EXPERIMENTAL AND NUMERICAL INVESTIGATION OF PIPING IN UNIFORM EMBANKMENT DAM WITH WEAK LAYER AT THE UPPER REGION

A Thesis Submitted to
the Graduate School of Engineering and Sciences of
İzmir Institute of Technology
in Partial Fulfillment of the Requirements for the Degree of

MASTER OF SCIENCE

in Civil Engineering

by
Merve OKAN

July 2022
İzmir

ACKNOWLEDGMENTS

I would like to thank my supervisor Prof. Gökmen TAYFUR and co-advisor Asst. Prof. Aslı BOR TÜRKBEN for their contributions, advice, and guidance for my work and research in the scope of my thesis. I also would like to thank specially Prof. Mehmet Şükrü GÜNEY for all his suggestions, allowing time, and his patience throughout the study who takes place in the thesis committee and who is the project manager of the project with the number 119M609 supported by The Scientific and Technical Research Council of Turkey (TUBİTAK) which makes the researches and studies available. I would like to give thanks to Prof. Alper BABA who is the member of the thesis committee.

I would like to thank Emre DUMLU who is the scholarship graduate student in the project for his help, encouragement, and good friendship during the study. Thanks to İsmail KESKİN, a laboratory technician at İzmir University of Economics, for his continuous help and support throughout the project and especially for helping me to prepare the soil material of the dams for the experiments. Thanks also to Emre Çağlar ÇELİK who is the final year civil engineering student at İzmir University of Economics for his help.

Special thanks to my family members, especially to my mother Faika OKAN, for their endless love, continuous support, and encouragement during the project period.

ABSTRACT

EXPERIMENTAL AND NUMERICAL INVESTIGATION OF PIPING IN UNIFORM EMBANKMENT DAM WITH WEAK LAYER AT THE UPPER REGION

From the past to nowadays, earth-fill dams have been built thanks to their advantages, however, piping is a problem that earth-fill dams can experience and then fail. While there are many studies about the overtopping failures of the dams, there are not too many surveys about dam failures due to piping.

Dams having a height of 0.6 m, a bottom width of 2 m, and a crest width of 0.20 m were built in a channel of 1 m wide, 0.81 m high and 6.14 m long. 3 different scenarios have been created and the evolution of dam failure resulting from seepage at the dam was recorded by six cameras located at different locations. In the closed system, water was pumped from the lower reservoir to the upper channel. The dam was constructed by using a mixture consisting of 85 % sand and 15 % clay. A circular tunnel with a diameter of 2 cm was created at the middle or corner of the dam according to the scenario and at 6 cm below the dam crest. The breach areas at different time instants at upstream and downstream sides are determined by using the Gauss Area calculation method and by image processing, and then it has been found that methods give close values to each other. Breach discharge and time-varied velocity values were determined by using the continuity equation.

Empirical relations were intended to be derived for the breach flow rate and empirical relations represented in the literature were trialed by using experimental findings.

ÖZET

ZAYIF BÖLGENİN ÜST BÖLGEDE OLDUĞU ÜNİFORM DOLGU BARAJDAKİ BORULANMANIN DENEYSEL VE SAYISAL ARAŞTIRILMASI

Toprak dolgu barajlar geçmişten günümüze avantajları sebebi ile inşa edilmektedir ancak borulanma toprak dolgu barajların yıkılmasına neden olan en temel problemlerden biridir, ayrıca geçmişte borulanma nedeniyle yıkılan toprak dolgu barajlar da vardır. Literatürde kret seviyesinden su aşması nedeniyle baraj yıkılmaları ile alakalı birçok çalışma bulunurken borulanma ile alakalı yeterli çalışma bulunmamaktadır.

1 m genişliğinde, 0.81 m yüksekliğinde ve 6.14 m uzunluğunda kanalın içinde 60 cm yüksekliğe, 2 m taban genişliğine ve 0.20 m kret genişliğine sahip toprak dolgu baraj inşa edilmiştir. 3 farklı senaryo oluşturulmuş, sızmadan kaynaklı baraj yıkılmasının gerçekleşmesi farklı yerlere konumlandırılmış 6 kamera ile kayıt altına alınmıştır. Kanal 2 kattan oluşup kapalı sistemde aşağıda bulunan su deposundan yukarıdaki kanala pompa ile su pompalanmıştır. Toprak dolgu baraj % 85 kum ve % 15 kil içeren zemin ile inşa edilmiştir. Senaryoya göre barajın ortasında veya köşesinde ve kretin 6 cm aşağısında 2 cm çapında yuvarlak bir tünel oluşturulmuştur. Farklı zamanlara ait gedik yüzey alanları memba ve mansap tarafları için ayrı olarak Gauss alan hesabı ve görüntü işleme yöntemi ile hesaplanmış, sonuçlar karşılaştırıldığında 2 metodun birbirine çok yakın sonuç verdiği görülmüştür. Gedikten geçen debi ve zamanla değişen hız değerleri memba ve mansap tarafları için ayrı olarak süreklilik denklemi kullanılarak hesaplanmıştır. Ayrıca, farklı zamanlara ait ıslak alanlar da belirlenmiştir.

Gedikten geçen debi için ampirik denklemlerin üretilmesi denenmiştir. Ayrıca, elde edilen deneysel bulgular kullanılarak literatürde sunulan farklı parametreler için ampirik denklemler denenmiştir.

TABLE OF CONTENTS

LIST OF FIGURES

Figure **Page**

Figure **Page**

Figure **Page**

Figure **Page**

Figure **Page**

Figure **Page**

LIST OF TABLES

Table **Page**

CHAPTER 1

INTRODUCTION

1.1. Background

A dam is a set that prevents or limits the flow of surface water or underground streams. Dams are constructed to provide drinking water, irrigation, energy, fishery, and flood prevention. Earth-fill dam is a type of embankment dam. It can be created by compacting soil which can consist of sand, clay, and silt. From the past to nowadays, earth-fill dams have been projected and built thanks to their advantages and still, they are built. Firstly, the advantages have been ordered.

- They are suitable for every valley type.
- Thanks to natural materials, the need for importing or transporting great amounts of processed materials or cement to the construction site decreases.
- The unit costs of earth-fill increase much more slowly than those for mass concrete.
- For the areas with high seismic activities, the earth-fill dams can be created more economically and show a higher performance by behaving more flexible during an earthquake when constructed with an optimum water content.
- A significant part of the construction process is carried out by machines and the machines have been developed day by day.

Also, there are some disadvantages.

- If the water level exceeds the crest level, earth-fill dams can be collapsed.
- The risk of seepage and piping through the earth-fill dam body and foundation is higher than in other types of dams.

Dams can fail because of stability problems such as excessive deformations, excessive stresses, or excessive loss of materials due to erosion, earthquakes, floods, overtopping flow, or piping. However, dams should not fail; all living things need water for survival. Thus, water should be saved and stored. Besides, dams are indeed

expensive structures to build. When they collapse, there will be considerable economic damage. Apart from these, the failure of dams can cause property damage and loss of life. For instance, Dai et al. (2005) explained that over 100,000 deaths by flood occurred at a large landslide dam in Dadu River that failed due to an earthquake. That's why, before starting construction, a required project should be designed and required precautions should be taken. Unfortunately, still, today embankment dam failures occur frequently. Zhong, Chen, and Deng (2017) emphasized that the most common dam type in the world is the earthfill dam, thus, 85% of total failures have been experienced by earthfill dams. Teton dam is a very well-known example of an earthen dam that experienced piping failure which caused flooding in 1976. Overtopping and piping can be accepted as the two most widespread failure modes of the earth- dams, levees, and dykes (Stéphane Bonelli and Benahmed 2010).

There have been many studies about dam failures especially because of overtopping in the literature, however since it is really difficult to observe the erosion process and conduct controlled experiments, there are not too many surveys about dam failure due to piping (Sharif et al. 2015; Chen, Zhong, and Shen 2019; Elkholy et al. 2015).

Costa (1985) informed that 28% of dam failure arises from piping and 34% from overtopping. Also, Chen, Zhong, and Shen (2019) indicated that between 1954 and 2018, 3541 dam breach accident occurred and more than 30% of them was due to piping in accordance with Dam Safety Management Center of the Ministry of Water Resources, P. R. China (2019). Besides, Zhong, Chen, and Deng (2017) notified that more than 50% of 3530 dam breach accidents from 1954 to 2014 were happened due to overtopping and 85% of total failures were including the homogeneous cohesive dams in accordance with Dam Safety Management Center of the Ministry of Water Resources, P. R. China (MWR 2015).

The estimation of breach initiation and evolution is of great importance for the evaluation of flood risk in terms of design, planning, and management, also flood magnitude, timing, and breach dimensions can be inferred (M. W. Morris 2013). There are many studies on the prediction of the breaching process that come up with numerical solutions or empirical equations in the literature. Piping and overtopping are some of the reasons allowing breach evolution. According to Morris (2013), structure type, design of embankment, hydraulic loading, the material used for embankment, construction, and condition of material can affect the breaching process. Zhenzhen

(2015) also stated that soil erosion and headcut migration lead to the process of breach widening.

Most of the researchers executing numerical analysis make some simplified assumptions concerning the shape of a breach and the discharge of water flowing through the breach. Morris et al. (2008) reveal that instead of simplified approaches, more realistic approaches are required about the breach mechanism as well as the breach geometry and flow through the breach.

1.2. Problem Statement

Breach shape is assumed generally in trapezoidal shape in different researches, however in reality, breach shape changes according to soil properties and hydraulic conditions. The change in geometry of this shape depended on the time is aimed to examine elaborately because, in the literature, many photographs display breaches in the last stage, however before reaching this last stage, the change in the geometry of the breach should be determined and considered. Thus, working with more realistic data is extremely important instead of simplifying assumptions.

1.3. Aim of the Research

The aim of this study is the experimental investigation of piping that is considerable in terms of safety of earth-fill dams which have significant functions and when collapsed cause property damage and loss of life. Empirical relations are intended to be derived for the breach flow rate and empirical relations represented in the literature are trialed by using experimental findings.

Creating different piping scenarios in the laboratory environment, investigating the development of the geometry of the breaches depended on the time that will occur due to piping and the flow rate along the breach are including this objective. Experiments are conducted in the civil engineering laboratory of İzmir University of Economics.

1.4. Outline

Advantages and disadvantages of earthen embankments, the importance of dam structures, effects of dam failures, statistical information of some piping and overtopping failures obtained through the literature, and the significance of the estimation of breach initiation and evolution were mentioned in the first chapter. Besides the statement of the problem, the aims of the research and study outline were stated.

In the second chapter, the literature review was presented. Experimental, numerical investigations and studies for developing and trailing empirical relations executed by researchers were explained.

In the third chapter, piping and overtopping mechanisms were explained. Fundamental mechanisms to initiate the internal erosion and piping of embankment dams were mentioned. Factors affecting initiation of piping and breach evolution were reviewed.

In the fourth chapter, the experimental setup and conducted soil mechanics experiments were represented.

In the fifth chapter, how the soil material of the dam was prepared, the construction process and scenarios with their differences between each other, and how scenario experiments were conducted were explained.

The sixth chapter displays Gauss area calculation and image processing methods, respectively.

In the seventh chapter, experimental findings of the scenarios were presented. The change in the reservoir water level with time, the discharge of water through the breach, surface breach areas, wetted areas, and accordingly velocities for upstream and downstream were calculated and represented. Breach evolution process with certain time instants was shown. The peak discharge through the breach, maximum reached surface breach areas, maximum wetted areas, and maximum velocities at both upstream and downstream for a certain time were indicated.

The eighth chapter indicates how the image processing technique was applied, the comparison of area values obtained by image processing and Gauss area calculation methods, and trialing of some empirical equations represented in the literature.

The ninth chapter shows the nonlinear regression analysis for the breach discharge equation given for the weirs.

In the last chapter, the conclusion, discussion, and recommendations of the study were represented under the title of the conclusion.

CHAPTER 2

LITERATURE REVIEW

In this chapter, experimental and numerical investigations carried out by researchers were explained. Also, studies for developing and trialling empirical relations were mentioned.

Fell et al. (2003) worked on a study to predict the time for piping to evolve and create a breach depending on the properties of the dam and its foundation. They tested their method with the experiences of failed dams and piping. The adequacy of monitoring and surveillance methods to notice internal erosion and piping according to the different beginning conditions of erosion is also investigated. They analyzed examples of piping failures and accidents from the literature, from sponsors, and other sources to examine the mechanisms of initiation, continuation, progression, and for failures, breach; in a practical way, also tested their method by utilizing failures and accidents for piping in the foundation, for piping in the embankment, and piping from the embankment to the foundation. They stated that the method is most reliable for piping in the embankment by indicating that if anything tends to predict a slower time than actual.

Greco et al. (2008) simulated the evolution of a breach in an earth-fill dam by using a two-dimensional depth-averaged (2DH) numerical model.

The diphasic flow volume and the jump equations containing the erosion processes are used in the development of a basic one- dimensional model for two-phase piping flow erosion by Lachouette, Golay, and Bonelli (2008). They stated that the particle concentration can affect the very early process considerably which can cause the expansion of the hole at the exit according to the model depending on constant input and output pressures. Dilute flow assumption was found as convenient for piping erosion flow modeling.

Zhu et al. (2011) constructed one embankment with pure sand and four embankments consisting of different sand-silt-clay mixtures, then investigated how erosion proceeds. They stated that cohesive soil embankments were affected considerably by headcut erosion in terms of breach evolution and experienced erosion

more slowly. Besides, shear erosion was at the forefront during the evolution of the breach at the embankment including only pure sand.

A one-dimensional numerical model was developed and improved by Alamdari, Banihashemi, and Mirghasemi (2012) by utilizing the mass-conserving finite volume method. The piping event was simulated and the model was verified with Teton dam. They emphasized that the radius in a certain place in 2 hours after the beginning of piping is almost equal to the radius obtained by the model which shows the variation of radius according to the time along the tunnel until the radius value attains the critical value and the piping event changes as the overtopping.

Zhang et al. (2012) investigated dam failure by overtopping in terms of erosion rate and sediment transport rate, then explained that peak sediment transport rate can be decreased by a longer dam crest and flatter inner slope which causes also extends the arrival time of peak sediment transport rate.

Fleshman and Rice (2014) managed a laboratory modeling program to evaluate the initiation of the piping evolution in several sandy soils with different specific gravity, gradation, grain size, and the grain shape. They conducted the models by using a laboratory tool produced and created especially for their study which helps to evaluate the hydraulic regime within the sampler during the test by imposing a uniform hydraulic gradient. That's why the beginning of the initiation piping process can be investigated according to required critical hydraulic conditions. Their results indicated that when the specific gravity of soils increases, piping resistance increases, also angular soils and graded soils resist piping events more. They also used finite-element seepage analyses to model the hydraulic conductivity of the loosened soil, the hydraulic conductivity of the undisturbed soil was arranged theoretically to account for the examined rise in void ratio and the analysis results showed a good agreement with examined behavior.

Elkholy et al. (2015) built earthen levees and examined internal erosion processes due to piping. While building levees, they used different mixtures containing sand, silt, and clay. The erosion process was recorded and by applying the image processing technique, they monitored erosion processes. For different soil compositions, the change in the depth of erosion during the piping was investigated. They concluded that even small changes in clay content can affect erosion rate considerably and when the soil composition changes considerably, the time will be influenced by causing a noticeable decrease in the reservoir level. A plastic pipe possessing a diameter value of 13.7 mm was used to create an initial hole, later it was removed to initiate piping. The

levee had dimensions of 0.46 m wide, 0.55 m long, and 0.15 m high, also 1:1 and 1:2 upstream and downstream slopes, respectively. During the experiment, they kept water constant with a maximum change of 10%. An edge detection algorithm and an automatic thresholding algorithm were implemented in turn to the images. They came up with an exponential equation to predict the erosion depth as a function of time and the coefficient of soil erodibility.

Sharif et al. (2015) prepared their earthen embankment by using the same procedure and monitored the erosion process by using the same method which was the image processing technique with Elkholy et al. (2015), however, the difference was this time, they had only one soil composition but they applied different numbers of blows during compaction to soil with determined normalized dry densities. The soil composition was the same for all the experiments consisting of 64% sand, 29% silt, and 7% clay, and can be taken into account as a sandy loam soil. Sharif et al. (2015) developed exponential equations to represent average erosion depth, area of vertical erosion, and volume of erosion with time. Also, they concluded that when the dry density of the soil mixture increases with an increase in the number of compaction blows, the run time is affected considerably which indicates the erosion rate, whereas it has not too much impact on the final average erosion depth. They discussed the changes in erosion depth, eroded side area, and eroded volume during the piping development by utilizing from image processing method.

Froehlich (2016) used outflow data of 41 dam failures to estimate the peak breach discharge of a dam by utilizing 2 nonlinear mathematical models and concluded that models showed a considerable performance in their estimation when compared with the other techniques.

Yang and Wang (2017) conducted some upward seepage experiments on sand specimens with two uniform soils which are stable and one gap-graded soil which is unstable. They compiled and analyzed a data set consisting of many different grain size distributions. Depending on the data set, they examined techniques for the prediction of critical hydraulic gradients and evaluated their performance. Three different soils were evaluated to observe the effect of gradation of soil on piping failure and critical hydraulic gradients. The specimens were exposed to upward seepage until a piping failure happens after they had been arranged. They concluded that gradation of soil affects critical hydraulic gradient and piping failure mode. A zero effective stress for internally stabled soil experiencing piping failure was logical, and failure was observed

with a volume expansion or a horizontal crack that progresses upward by breaking the top surface. Internally unstable soil was exposed to piping failure with strongly eroded fine particles by an upward seepage flow and they emphasized that coarse particles displayed a stable behavior.

Ashraf et al. (2018) used a nonlinear regression technique to produce new equations so that estimated breach parameters by benefiting from the data of 126 embankment failures, then tested their equations with the data of the 5 experiments executed on overtopping failures of non-cohesive and cohesive soil embankments. They emphasized that the values obtained by the equations were consistent with non-cohesive material while were not with cohesive materials, so that except for dam dimensions also soil properties can be taken into consideration for breach parameters of dams constructed with cohesive soils.

Wang et al. (2018) created nine nonlinear models by using regression analysis for the first eight models and a semi-analytical approach for the last model. The peak outflow of embankment dams experiencing breaching was predicted by investigating the data of 40 dam failures and then pointed out that the best model can be considered the model obtained with a semi-analytical approach. The parameters of water depth above breach invert and volume of water stored above breach invert contributed more to predicting targets when creating the models with regression analysis rather than parameters of average embankment width and embankment length.

Andreini et al. (2019) introduced probabilistic models for concentrated leak mechanisms to estimate the parameters such as the coefficient of erosion, the geometrical dimensions of the embankment, the critical shear stress, and the pipe radius enlargement for both cohesive and non-cohesive soils, then stated that effect on vulnerability to erosion of some soil characteristics can be estimated by the model for water retaining structures.

Chen, Zhong, and Shen (2019) assumed that before the failure of the pipe roof, the piping shape was an arch tunnel with a semicircle at the top and a square at the bottom under the condition when the dam will not consist of sand. They created a numerical model and took an arch tunnel as the initial cross-section. They selected a case with detailed measured data to verify the created numerical model, then, to investigate the model, they selected historical incidents of two artificially filled earthen dams. Lastly, the proposed model was tested by comparing it with the NWS BREACH model (Fread 1988). Also, when the proposed model was compared with the model,

they found that the model can give more reliable results of peak flow discharge in the breach and final breach widths.

Saliba et al. (2019) utilized Plaxis 2D and modeled an earth dam in Lebanon to indicate the evolution of piping by employing an iterative approach. Soil characteristics were specified according to ASTM standard methods. They reviewed that when the hydraulic gradient value was higher than the critical hydraulic gradient, the location of piping was determined.

CHAPTER 3

MECHANISIM OF PIPING AND OVERTOPPING

Because of the cracks, erosion within the earthen material occurs and this situation allows seepage of water through the earth-fill dam. Since more water can penetrate and flow through the dam, piping can be created. As the seepage force exceeds the weight of the materials occurring in the dam, the water washes away the soil and creates a hole within the earth-fill dam. If these holes enlarge and extend longitudinally due to washing much more material away, it can be called piping. Sellmeijer (1988) stated that piping can be defined as a channel starting the downstream of the structure by converging as flowlines and accordingly there will be high seepage pressures.

Fell et al. (2003) explain that there are 4 steps for breaching which are the initiation and continuation of erosion, the evolution of the pipe, the breach formation, and the widening of a breach. There are 4 fundamental mechanisms to initiate the internal erosion and piping of embankment dams and these can be ordered as concentrated leak erosion, backward erosion, contact erosion, and suffusion (Bonelli 2013; Zhenzhen 2015). Zhenzhen (2015) gives a table and explains the mechanisms one by one; the erosion that arises from a crack, cavity, or void was defined as concentrated leak erosion where a pipe is created, and the erosion process from downstream to upstream by removing soil particles as backward erosion, contact erosion happens where fine and coarse particles are in contact and fine soils are eroded by flow which is parallel to the coarse particles (ICOLD 2017), seepage flow causes movement of fine particles through the coarse particle pores and this happening can be called as suffusion (ICOLD 2017).

According to the Training Document No.39 report of U.S. Army Corps of Engineers (Brunner 2014), Figure 3.1 represents the piping process; firstly the material is internally eroded by seeping water through the dam and since material is eroded, a hole will be created which enables more water seepage and more erosion as shown in Figure 3.1 (A), secondly, downstream side starts to experience erosion and headcutting due to flow leaving the hole as shown in Figure 3.1 (B), then since hole becomes larger

and larger with time, the part existing on the hole will be weaker and start to pour into flowing water as shown in Figure 3.1 (C), Figure 3.1 (D) shows that how the headcutting continues while it is developing toward upstream, with time since the part on the extending hole will not be able to withstand its weight , it will completely pour into water so that breach outflow will increase by causing also an increase in breaching process and orifice type flow of pipe will be converted into open-air weir flow. Both toward upstream and downstream, erosion and headcutting proceed by widening the breach (Figure 3.1 (E)). The breaching process can continue until reaching the bed of the dam based on the remaining reservoir capacity.

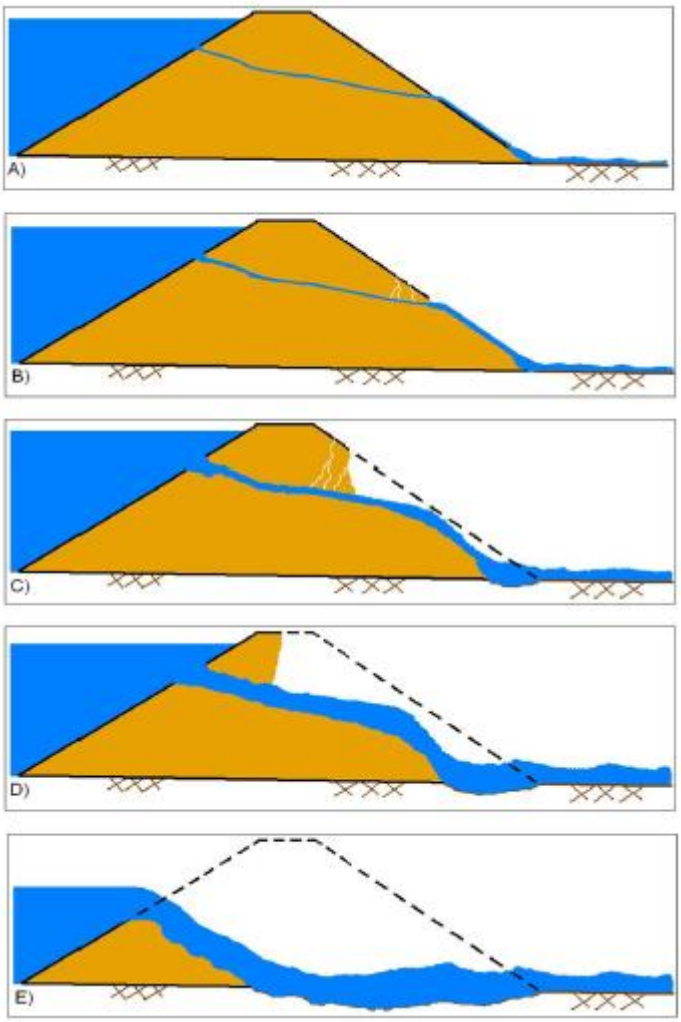

Figure 3.1. Breach process of piping failure (Source: Training Document No.39 report of U.S. Army Corps of Engineers (Brunner 2014))

There are some factors affecting the initiation of piping and breach evolution stated in the literature. The soil erodibility is a basic parameter indicating the time for the embankment failure (Sharif et al. 2015), and play an important role while estimating the performance of embankment in terms of internal erosion and breach failure (Temple et al. 2005; Elkholy et al. 2015; Sharif et al. 2015). According to Sharif et al. (2015), the hydraulic and mechanical properties of the soil change with internal erosion. Moreover, they stated that soil properties affect the failure of embankments considerably and proper compaction during construction is a key process that reduces porosity. Chen, Zhong, and Shen (2019) stated that breach evolution can be affected by the soil erodibility and initial pipe position according to their sensitivity analysis. According to Hanson et al. (2010), the openings initiating piping can arise from inadequate compaction during construction, differential settlement, desiccation, earthquakes, burrowing animals, and/or decay of woody vegetation roots.

For the flow of fluid through porous media, the Equation 3.1 called as Darcy law is generally used, where V is the Darcy (seepage) velocity, k is the hydraulic conductivity, i is the hydraulic gradient.

$$V = ki \tag{3.1}$$

Solid particles carried by water depend on the flow rate, which varies with the hydraulic gradient. The water that moves in the soil in a way that loses its energy as quickly as possible exerts a force on the particles. This force, the magnitude of which depends on the hydraulic slope, acts in the direction of seepage. For this reason, although the water leaking in the direction of gravity has a compacting effect on the particles, it tries to move the particles when it occurs in the opposite direction. When the imbalance between upward and downward forces occurs, piping phenomenon happens in non-cohesive soils. The stability of the soil where the piping occurs is deteriorated and at the same time it becomes unable to carry the load. The soil in the seepage area is under the effect of a resultant force that depends on its own weight and the seepage force. The hydraulic gradient of the seepage force that drags the particles in the soil is important which is specified as the critical hydraulic gradient in soil mechanics. The critical hydraulic gradient is given in the Equation 3.2.

$$i_c = \frac{h}{L} = \frac{G_s - 1}{1 + e} \tag{3.2}$$

where i_c is the critical hydraulic gradient, G_s is the specific gravity of soil and e is the void ratio.

The critical hydraulic slope does not depend on the size of the particles, thus, coarse and fine sand particles will behave in separate hydraulic gradients. However, since coarse particles have a high permeability, a large amount of flow is required according to Darcy's law to maintain the critical hydraulic gradient. Since the seepage force is proportional to the hydraulic gradient, piping occurs where the hydraulic gradient is high. The stability of dams against piping is determined by comparing the hydraulic gradient where piping is expected with the critical hydraulic gradient.

The hydraulic gradient where piping is expected is specified from the flow net and is also defined the existing hydraulic gradient. It can be said that there is safety when the existing hydraulic gradient of the piping zone is less than the critical hydraulic gradient. The safety of the dams against piping is determined by the safety factor obtained from the Equation 3.3 given below.

$$FS = \frac{i_c}{i_e} \tag{3.3}$$

where i_e is the existing hydraulic gradient.

When the water level exceeds the crest level, a continuous flow over the dam causes a decrease in the crest level by the erosion process, and overtopping failure can occur with time. A continuous flow exceeding the crest level cause overtopping by eroding the crest and downstream surface. In a weak part, erosion starts due to tractive shear force which exceeds the critical resistance (Qiming Zhong et al. 2021). Overtopping failure can arise from heavy floods, thus, the design of the dam plays an important role where surface elevation should not reach the crest level. Besides, waves can cause overwash and with wind, there will be overtopping.

According to the TD-39 report of the U.S. Army Corps of Engineers (Brunner 2014), Figure 3.2 represents the overtopping process; the downstream side will be exposed to headcut erosion during overtopping failure as shown in Figure 3.2 (A). A broad-crested weir behaviour is observed during the water flowing over the crest level and the headcut will expand by eroding backward and to the dam center where displayed in Figure 3.2 (B), Figure 3.2 (C) shows when the headcut arrives crest level, Figure 3.2 (D) demonstrates loss of upstream crest where a sharp-crested weir behaviour can be observed, then, erosion will proceed throughout the dam (Figure 3.2 (E)).

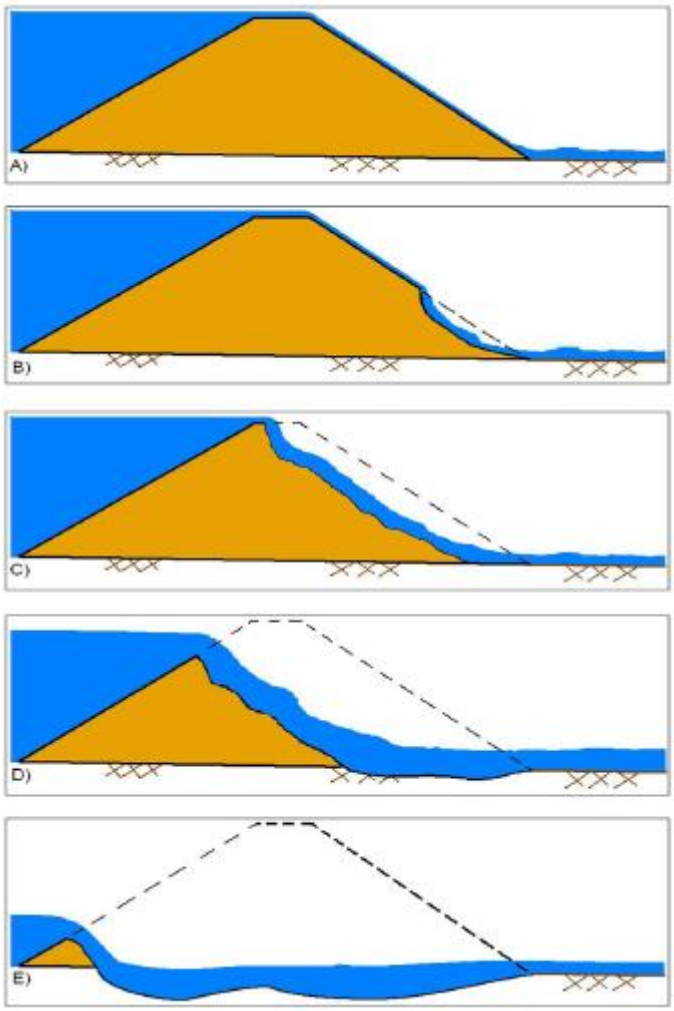

Figure 3.2. Breach process of overtopping failure (Source: Training Document No.39 report of U.S. Army Corps of Engineers (Brunner 2014))

CHAPTER 4

EXPERIMENTAL SETUP AND LABORATORY EXPERIMENTS

The experimental setup and conducted soil mechanics experiments have been presented in this chapter. The soil mechanics experiments were conducted according to ASTM standards. Standard proctor test, consolidation test, direct shear test, wet sieve analysis, hydrometer analysis, permeability test, and specific weight test have been conducted, and then significant soil parameters were indicated.

4.1. Experimental Setup

The dams for different experiment scenarios were conducted in a rectangular flume with a width of 1 m, a height of 0.81 m, and a length of 6.1 m in the İzmir University of Economics (Figure 4.1 and Figure 4.2). The flume consists of two parts; an upper channel and a bottom part. At the bottom part, there are a water tank and a sedimentation pool. A pump is utilized to maintain continuous flow to the upper channel of the flume from the water tank.

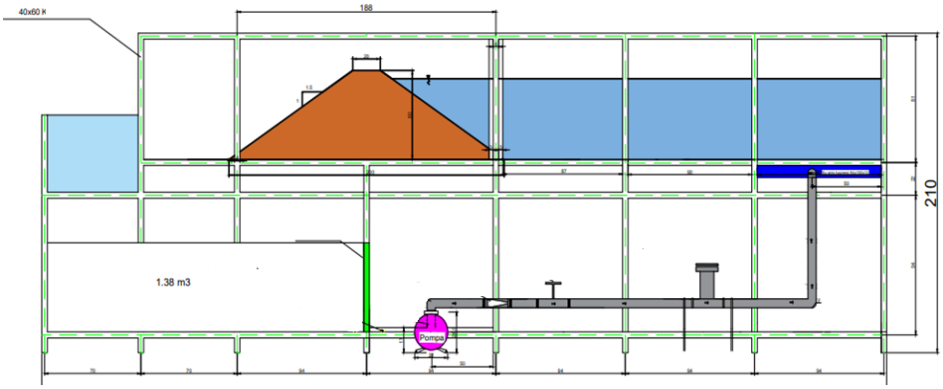

Figure 4.1. Experimental Flume Illustration

To adjust the flow from the pump to the flume, a control valve is used. A flow straightener was assembled during the production of the flume on the upstream side to make a smooth flow and decrease turbulence. The flowrate was measured by a magnetic flowmeter. To adjust the water level, an electromagnetic sensor was attached which starts and stops the pump when water depths in the channel were 0.540 m and 0.555 m, respectively. Grid lines were arranged on the side glasses with 1-cm grid interval.

Figure 4.2. Experimental Flume

4.2. Soil Mechanics Experiments

Some soil mechanics experiments were carried out before building the dam. The soil mixture utilized in the construction of the dam was prepared by using 85 % coarse sand and 15 % clay. The grain-size distribution of the mixture obtained from the wet sieve and hydrometer analyses is shown in Figure 4.3.

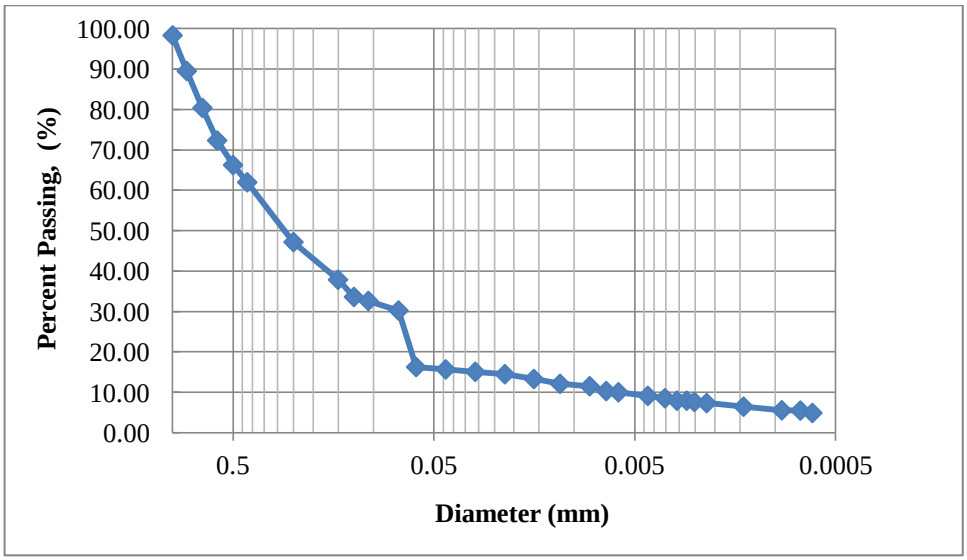

Figure 4.3. Grain size distribution of the dam material

From Figure 4.3, some characteristic diameters were obtained as D_{10}= 0.006 mm, D_{30}= 0.075 mm, D_{50}= 0.3 mm, and D_{60}= 0.4 mm. The uniformity coefficient C_u equals 66.7 and the curvature coefficient C_c is equal to 2.34.

The specific weight of the mixture was found to be G_s = 2.63 (Table 4.1) , from the test ASTM D854 – 14. Besides, the permeability of the mixture was obtained as k= $4.66 \cdot 10^{-4}$ cm/s from the falling head permeability test.

In order to increase the probability of the piping occurrence, the standard proctor test (ASTM-698) was conducted by reducing the applied energy by 50% (13 blows instead of 25) and so obtained the relationship between the maximum dry density and optimum water content was determined as Υ_{drymax}= 1.794 g/cm^3 and w_{opt} = 12.5 % (Figure 4.4). The void ratio (e) was calculated as 0.469.

Table 4. 1 Specific weight of soil mixture

Soil Mixture (85% Coarse Quartz + 15% Clay)	
First Experiment	
Sample Weight (g)	60.000
Pycnometer Weight (g)	144.680
Pycnometer + Water (g)	641.270
Pycnometer + Water + Sample (g)	678.420
G_1	2.626
Second Experiment	
Sample Weight (g)	60.000
Pycnometer Weight (g)	144.680
Pycnometer + Water (g)	641.370
Pycnometer + Water + Sample (g)	678.520
G_1	2.626

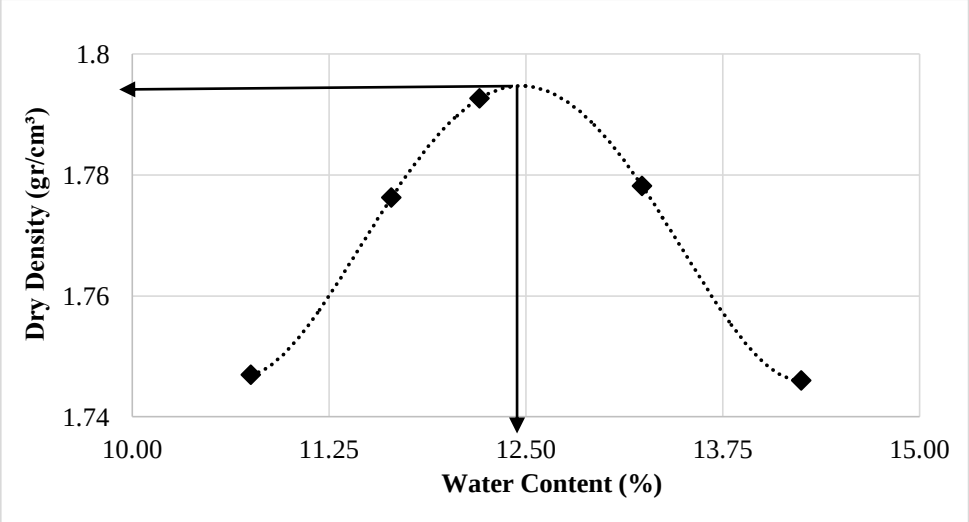

Figure 4.4. Dry density - water content relationship for proctor test with 13 blows.

Also, when the standard proctor test (ASTM-698) was conducted with 25 blows, the relationship between the maximum dry density and optimum water content was determined as Υ_{drymax}= 1.886 g/cm^3 and w_{opt} = 9.8 % (Figure 4.5).

From the direct shear test, it was found that the soil has a cohesion value of 15.33 kPa and an internal friction angle of 33.93^0 (Figure 4.6 and Figure 4.7).

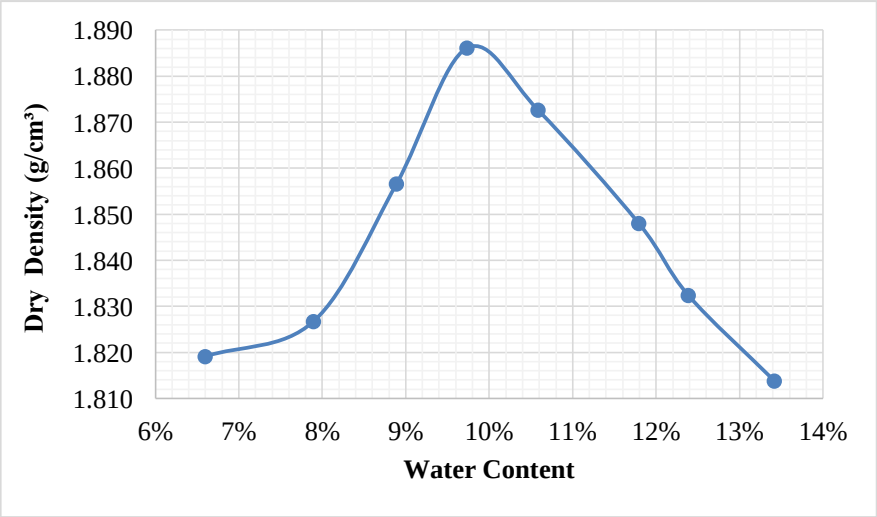

Figure 4.5. Dry density - water content relationship for proctor test with 25 blows.

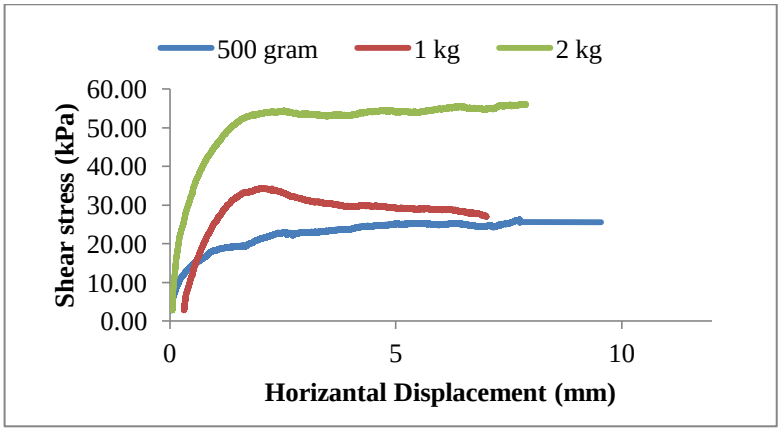

Figure 4.6. Shear stress vs. horizontal displacement

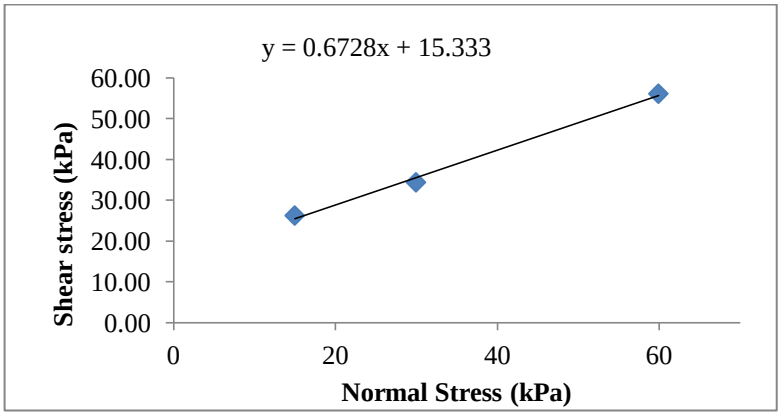

Figure 4.7. Max. shear stress vs. normal stress

According to the consolidation test results (Figure 4.8), the compression index (Cc), recompression index (Cr) and, swelling index (Cs) were found to be 0.100, 0.009, and 0.007, respectively. The oedometric modulus of deformation (E_{oed}) was obtained as 35714 kN/m² (Figure 4.9).

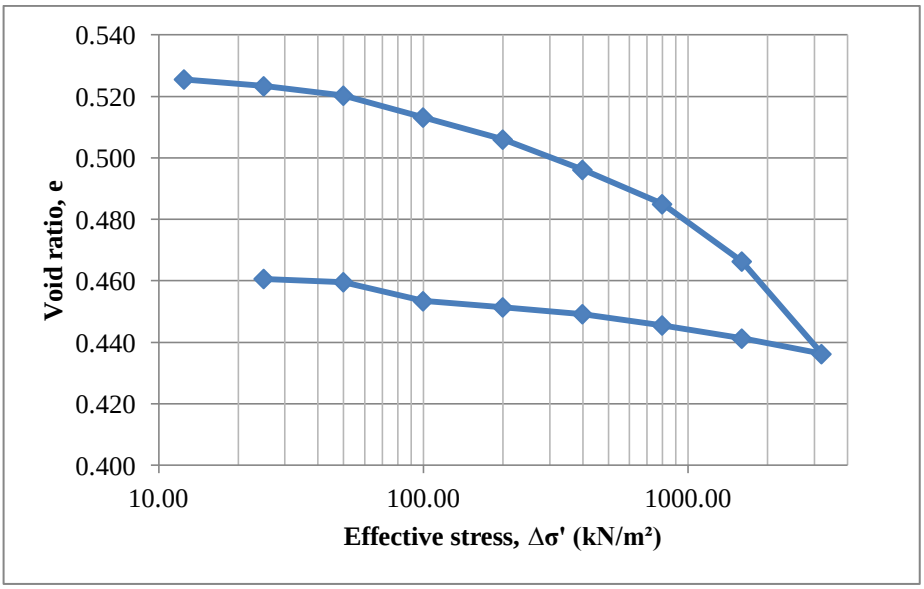

Figure 4.8. Compressibility curve

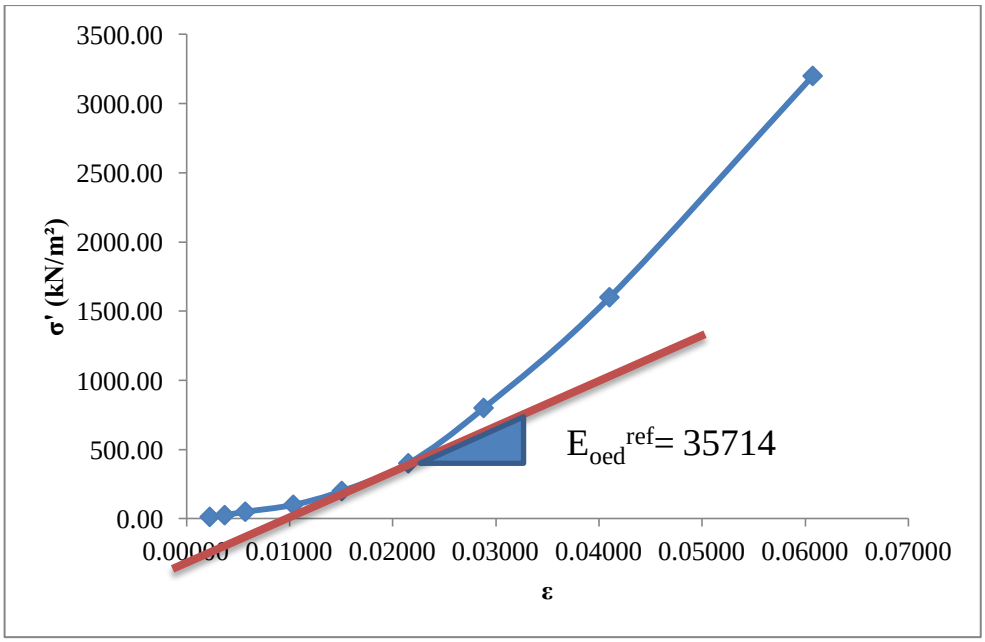

Figure 4.9. The oedometric modulus of deformation (E_{oed})

CHAPTER 5

CONSTRUCTION PROCEDURE AND SCENARIOS

5.1. Construction Procedure

The dams were homogenous types and constructed in 6 layers (Figure 5.1). Each layer had a height of 10 cm. The bottom layer had 200 cm in length. During the construction, L-shaped molds which possess 15 cm edge dimensions were utilized to create a rectangular volume. L-shaped molds with 15 cm sides cause a 30 cm reduction in each layer, 15 cm from the right and 15 cm from the left. Therefore, before trimming, the lengths of the layers in the dam were 200 cm for the 1st layer, 170 cm for the 2nd layer, 140 cm for the 3rd layer, 110 cm for the 4th layer, 80 cm for the 5th layer, and 50 cm for the 6th and final layer. The inner width of the dam is 96 cm. The rectangular volumes which are created to pour the wet material were calculated by multiplying 96 cm width, calculated lengths, and the 2.5 cm height. The volumes of each layer are given in order as 192000 cm^3 for the first, 163200 cm^3 for the second, 134400 cm^3 for the third, 105600 cm^3 for the fourth, 76800 cm^3 for the fifth, and 48000 cm^3 for the last layer, respectively.

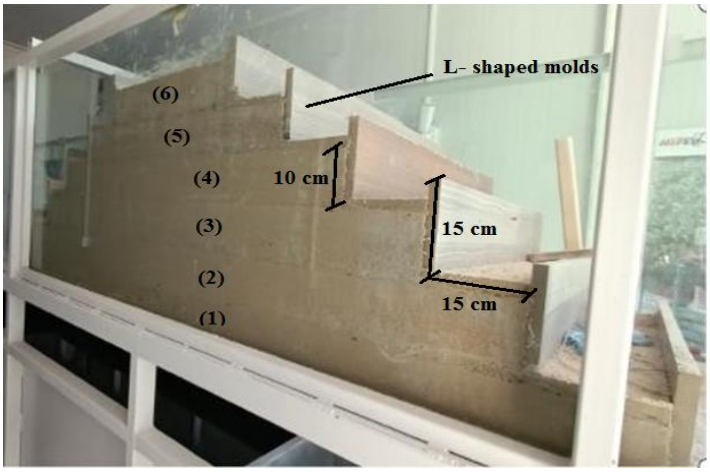

Figure 5.1. Layers and place of L-shaped molds

The soil mixture utilized in the construction of the dam was prepared by using 85 % coarse sand and 15 % clay. In order to specify the water content, the standard proctor test (ASTM-698) was executed by applying 13 blows. The reason for applying reduced energy (13 drops instead of 25) was to increase the probability of the piping occurrence. The bulk density and optimum water content were obtained as Υ_{bulk}= 1.997 g/cm^3 and w_{opt} = 12.5 % from the proctor test with 13 blows, and then the soil was prepared by using these values. According to this bulk density, the weight of material that needs to be compacted for each layer is calculated using known volumes in each layer. The wet material weights that needed to be compacted for each layer to be built with this soil are calculated as 383424.0 grams for the first, 325910.4 grams for the second, 268396.8 grams for the third, 210883.2 grams for the fourth, 153369.6 grams for the fifth and 95856.0 grams for the last layer, respectively.

In the construction stage, the compaction process has been conducted for 2.5 cm height and a minimum 50 cm length in order to satisfy the required homogeneity. The layers of 10 cm were compacted for every 2.5 cm, that is, first to 2.5 cm, then to 5 cm, 7.5 cm and finally reaching 10 cm. By supplying 1.997 g/cm³ bulk density, the weights for the relative volume were calculated and compacted. During the soil compaction, the bulk density of 1.997 g/cm^3 was satisfied for each layer according to the proctor test results. Each layer has the same weight in the same volume. The dam consisted of 6 layers and each 10 cm layer was created in four parts by reducing 3.5 cm height to 2.5 cm with 22 hammer blows on 46x92 cm^2 plate.

While preparing the soil material, first the dry material (sand and clay) was mixed in the concrete mixer for at least 10 minutes (Figure 5.2 (a)). Then, the dry material was poured into a wheelbarrow (Figure 5.2 (b)). The water was added to dry material and mixed by 2 people using shovels in the wheelbarrow until there is no dry material left.

Because of the clay in the soil mixture, clotted materials arise which affect the compaction and homogeneity of the material negatively. To prevent this negative effect; while pouring the materials into layers, the clotted materials are opened by hand (Figure 5.3 (a)). Before starting a new layer, the dam surface is slightly wetted and roughened with a small brush (Figure 5.3 (b)). The purpose of this is to prevent segmentation that is likely to occur. After roughening, the new layer is started. The wet material is compacted to the determined reference level by the hammer of the proctor experiment set on a wide wooden plate (Figure 5.3 (c)). Figure 5.3 (d) shows after compaction of

the first layer. Since the dams have large dimensions, the construction process was completed in a specified period. If the construction process would continue in the upcoming times, the dam surface was covered with a damp cloth and cover to prevent water loss.

When the construction has been completed, the molds which shown in Figure 5.3 (e) were removed; and then, the dam surface was trimmed with a trowel for the determined slope (Figure 5.3 (f)).

At the upper channel of the flume, some homogeneous dams possessing 0.6 m height, 2 m bottom width, and 0.20 m crest width were constructed with the slope at the upstream and downstream sides of 1:1.5. The evolution of the dam failure was recorded by six cameras placed at different locations. The water depths in the channel were attained from the camera recordings. In order to evaluate the shape of the breach and survey the changes in its geometry, the upstream and downstream camera images were investigated. In order not to work with fisheye images, the videos taken from lateral camera recording were edited and straightened with Hit-film-Express version 2021.1. Moreover, extra sensitive solutions were implemented to ensure that the images are completely flat.

(a) (b)

Figure 5.2. (a) Concrete mixer used to mix clay and sand (b) Wheelbarrow used to the mix water and dry materials

(a)

(b)

(c)

(d)

(e)

(f)

Figure 5.3. Some construction stages: (a) Roughening the surface with a small brush, (b) Opening clotted material by hand (c) Compacting by proctor hammer, (d) The first layer after compaction, (e) The last layer after compaction, (f) Final shape.

5.2. Scenarios

In this study, some different scenarios of experiments have been carried out. A circular hole of 2 cm diameter lying from upstream to downstream was created to initiate piping and to form a breach in all the scenarios. The experiments were started when the water in the flume reached this level and passed through the hole. The differences between the scenarios were represented in the following.

- In the first scenario, a 2-cm circular hole at 54 cm level and the right side of the dam was created (Figure 5.4). The pump was adjusted to maintain 3.82 m^3/h continuous flow.

Figure 5.4. Initial hole place for the first scenario

- After conducting the experiment for the first scenario, the breach occurred at the glass side of the dam. The second scenario was executed by trimming only the breach part of the dam coming from the first scenario by using a trowel (Figure 5.5) and then building that part again by satisfying the bulk density of 1.997 g/cm^3 as shown in Figure 5.6. A 2-cm circular hole was created at the middle and 54 cm level of the dam body (Figure 5.7). The pump was adjusted to maintain 3.82 m^3/h continuous flow.

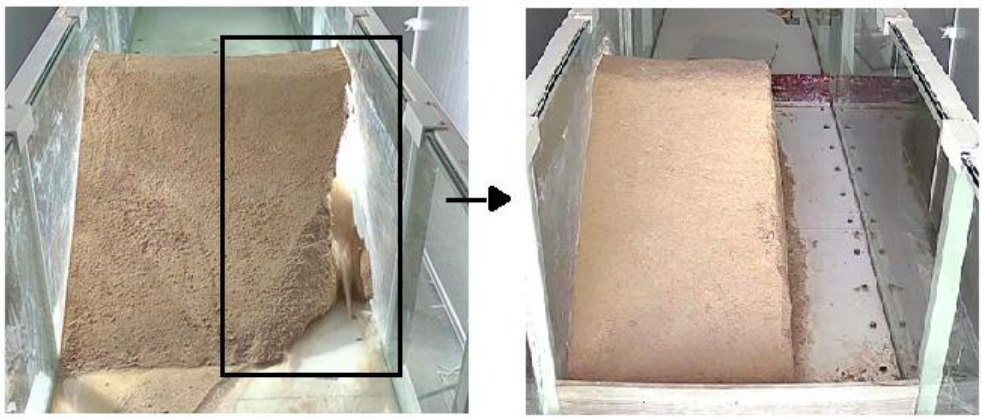

Figure 5.5. Trimming of the breach part of the dam coming from the first scenario

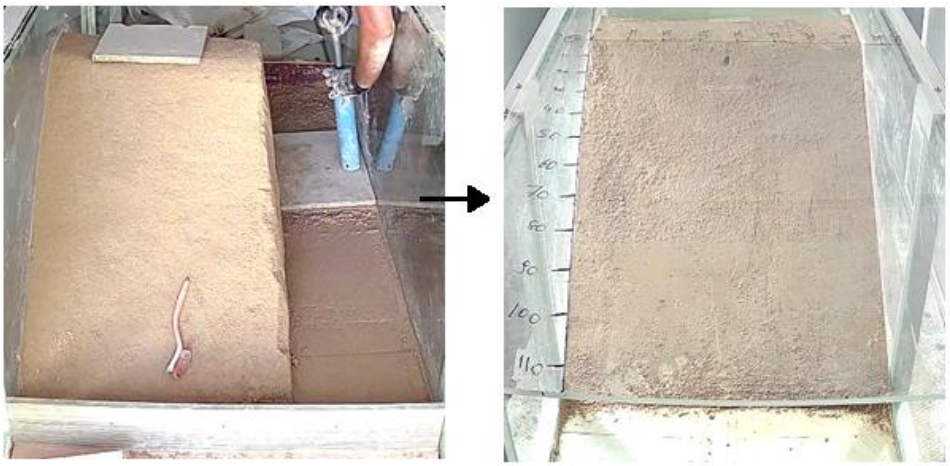

Figure 5.6 Construction of the trimmed part to create the dam for the second scenario

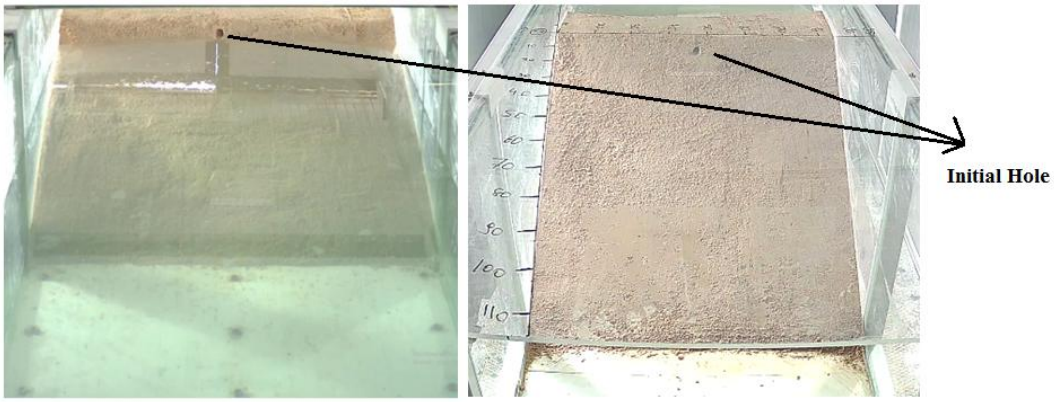

Figure 5.7 Initial hole place for the second scenario

- In the third scenario, a new dam was constructed with a 2-cm circular hole at the 54-cm level and the middle of the dam (Figure 5.8). Also, only for the 3rd scenario, the dam surface has been painted with green spray in order to work image processing more readily as shown in Figure 5.9. The pump was adjusted to maintain 6.96 m^3/h continuous flow.

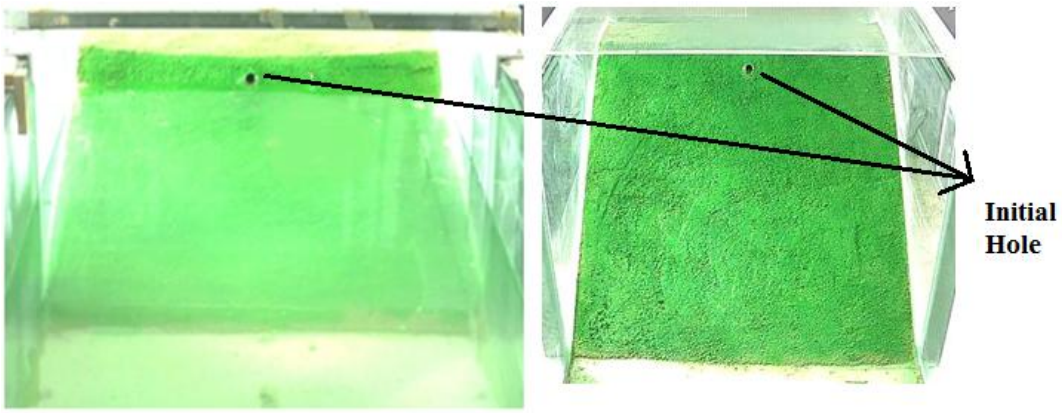

Figure 5.8 Initial hole place for the third scenario

Figure 5.9 Painting the dam surface with green spray for the third scenario

CHAPTER 6

METHODS

The images taken from the records corresponding to a certain time were scaled and the boundary coordinates of the breaches at downstream and upstream sides were specified at Get-data Graph Digitizer 2.26 software. The surface areas of the breach developed at different instants were computed by the Gauss Area calculation and Image Processing color thresholding technique. The temporal variations of the breach areas and the time-dependent wetted area values were investigated in the Get-data Graph Digitizer 2.26 software. The image processing color thresholding technique has been applied to determine erosion lines and breach areas in the MATLAB environment.

6.1. Gauss Area Calculation

Gauss area calculation formula, which can be called also as Shoelace formula, is used to calculate the area of a polygon. To be able to use the formula, the point coordinates are required as shown in Figure 6.1 and Figure 6.2. Since there is a cross multiplication of coordinates in the calculation which behaves like a shoelace, it has called shoelace formula (Dahlke 2017).

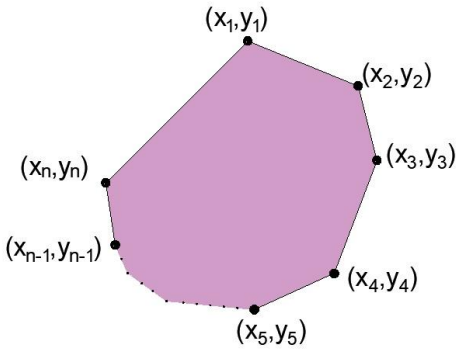

Figure 6.1. n-sided polygon with point coordinates

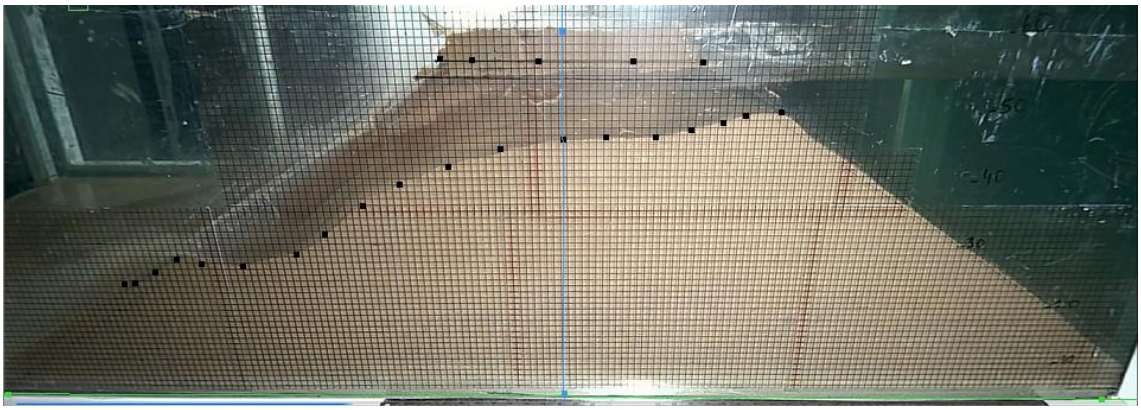

Figure 6.2. Assigning coordinates on Get-data Graph Digitizer 2.26 software environment

For the area of a n-sided polygon (A_1, A_2,…, A_n), shoelace formula is given in the Equation;

$$Area = \frac{1}{2} |(x_1y_2 + x_2y_3 + \cdots + x_ny_1) - (x_2y_1 + x_3y_2 + \cdots + x_1y_n)| \quad (6.1)$$

Besides, the formula can be written briefly as,

$$Area = \frac{1}{2} \sum_{i=1}^{n} x_i(y_{i+1} - y_{i-1}) \quad (6.2)$$

or,

$$Area = \frac{1}{2} \sum_{i=1}^{n} y_i(x_{i-1} - x_{i+1}) \quad (6.3)$$

where n is the number of sides, x_i and y_i represent the abscissa and ordinate in the i coordinate, respectively.

6.2. Image Processing Technique

Red, green, and blue colors can be indicated numerically and briefly cited as RGB. Color information is investigated by using some color spaces which makes it easy to carry out some calculations by specifying colors ("Understanding Color Spaces and Color Space Conversion," n.d.). RGB and HSV can be given as some color space examples where RGB color space expresses colors according to red, green, and blue amounts and HSV color space utilizes hue, saturation, and value. According to Mustikasari and Madenda (2014), when it is compared with RBG color space, HSV undergoes the way of human experience more substantially. While RGB values can be arranged from 0 to 255, HSV color space from 0 to 1.

Image segmentation is a technique that is used to separate an image into different spaces according to some image properties by considering their homogeneity or similarity where color, edges, and texture were utilized (Kulkarni 2012). Different properties can also arise from different color spaces so that suitable color space can be selected according to the problem (J. Yang, Liu, and Zhang 2010).

Thresholding can be regarded as the most straightforward technique while segmenting images for image processing and binary images can be created from a grayscale image by using thresholding (Shapiro and Stockman 2002). This method evaluates the color spaces according to similarity property. The color channels are segmented by applying the threshold technique on different color spaces such as RGB or HSV.

While applying gray thresholding, a threshold value is determined. Then, the original pixel value of a gray level image is compared with the threshold value. When the original pixel value is less than the determined threshold value, actual pixel values will be assigned as 0; if not, they will be assigned as 1. That's why the newly obtained image will be a binary image whose pixel values are segmented by a single thresholding technique. Besides, more than one thresholding value can be selected. When there are 2 thresholding values, if the original pixel value is between thresholding values, original pixel values will be assigned as 1, if not, they will be assigned as 0.

Also, there is a color thresholding technique (Figure 6.3). Kulkarni (2012) explains that the color information of the object in an image is required to separate it from the background and other objects. By determining a thresholding range, the pixels

outside the range will be disapproved and intended objects will be achieved. Madani et al. (2011) stated that when the color thresholding method is compared with other methods in terms of simple usage, it is the most popular technique.

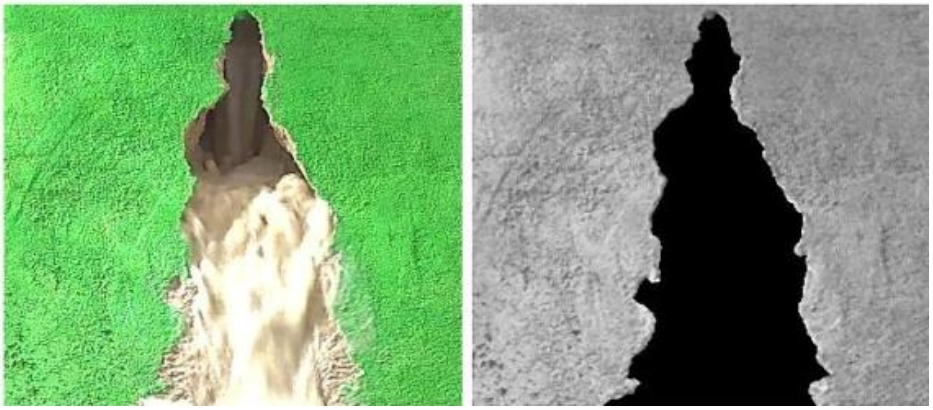

(a) (b)

Figure 6.3. a) Before and b) After applying the color thresholding technique to the image

CHAPTER 7

EXPERIMENTAL FINDINGS AND RESULTS

In this chapter, experimental findings of the scenarios have been presented. How the reservoir water level changed with time was shown, and the discharge of water through the breach, surface breach areas, wetted areas, and accordingly velocities for upstream and downstream were calculated. The process of breach evolution was also displayed for different time instants. The peak discharge through the breach, maximum reached surface breach areas, maximum wetted areas, and maximum velocities at both upstream and downstream for a certain time were indicated. The discharge of water through the breach was determined by using the continuity equation:

$$\Delta S = \left(Q_{pump} - Q_{breach}\right) \cdot \Delta t \tag{7.1}$$

where Q_{pump} is the flow rate delivered by the pump, Q_{breach} is the discharge through the breach, ΔS is the storage in the channel during the time interval Δt.

The average velocity V of the flow through the breach was approximately calculated by using the Equation 7.2 where A represents wetted area.

$$V = \frac{Q_{breach}}{A} \tag{7.2}$$

7.1. First Scenario

For the first dam, in order to initiate the breach formation, a circular hole of 2 cm diameter extending from upstream to downstream was created at 54 cm from the upper right side of the dam body. The experiment was started when the water in the

flume reached this level and passed through the hole. The temporal developments of the breach recorded by the cameras located on the downstream, upstream, and lateral side of the dam are shown in Figure 7.1, Figure 7.2, and Figure 7.3, respectively. The time t=0 indicates the beginning of the seepage.

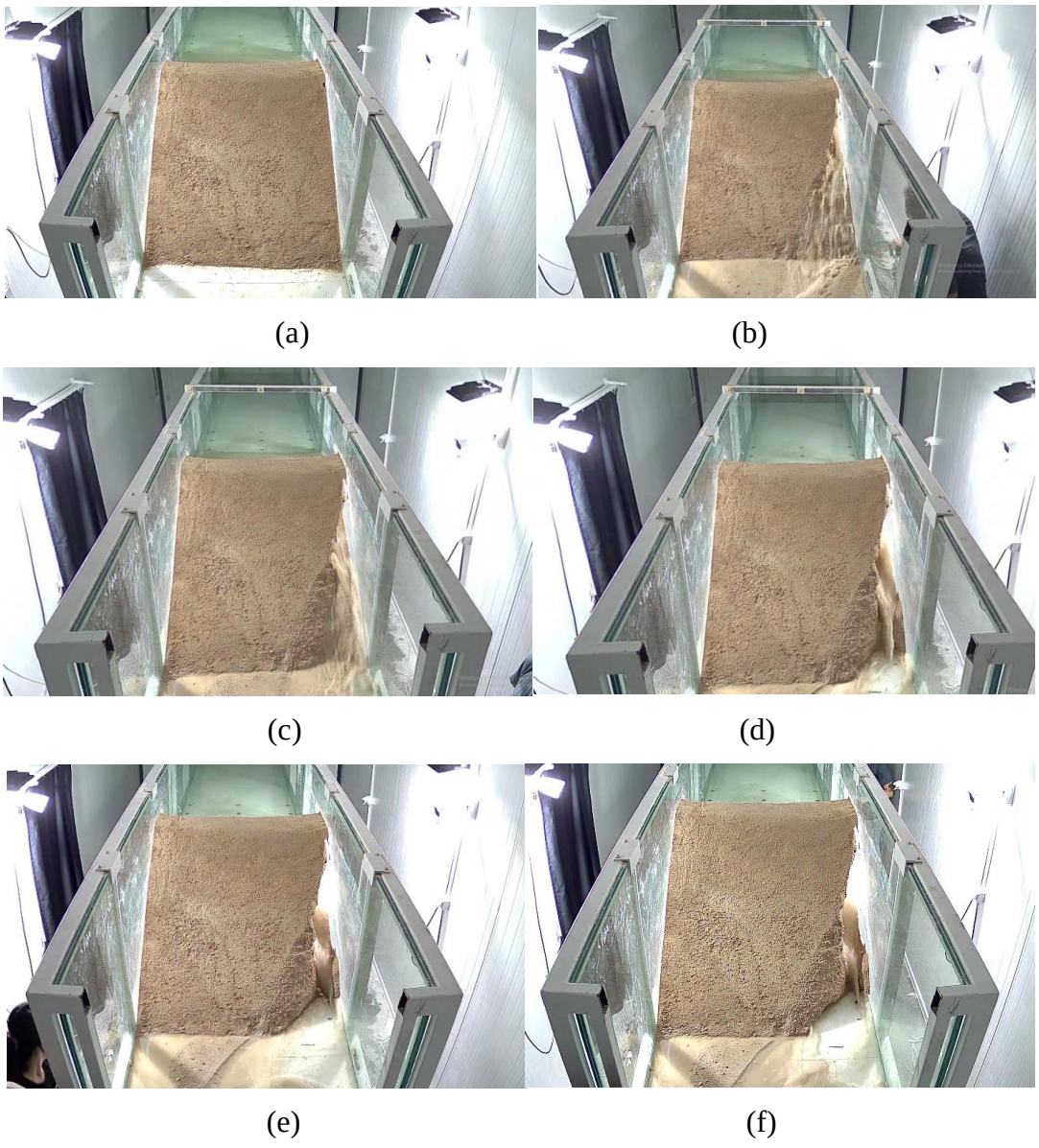

(a) (b)

(c) (d)

(e) (f)

Figure 7.1. The temporal development of the breach at downstream a) t=0 s, b) t=220 s, c) t=340s d) t=680 s, e) t=1020 s f) t=1360 s.

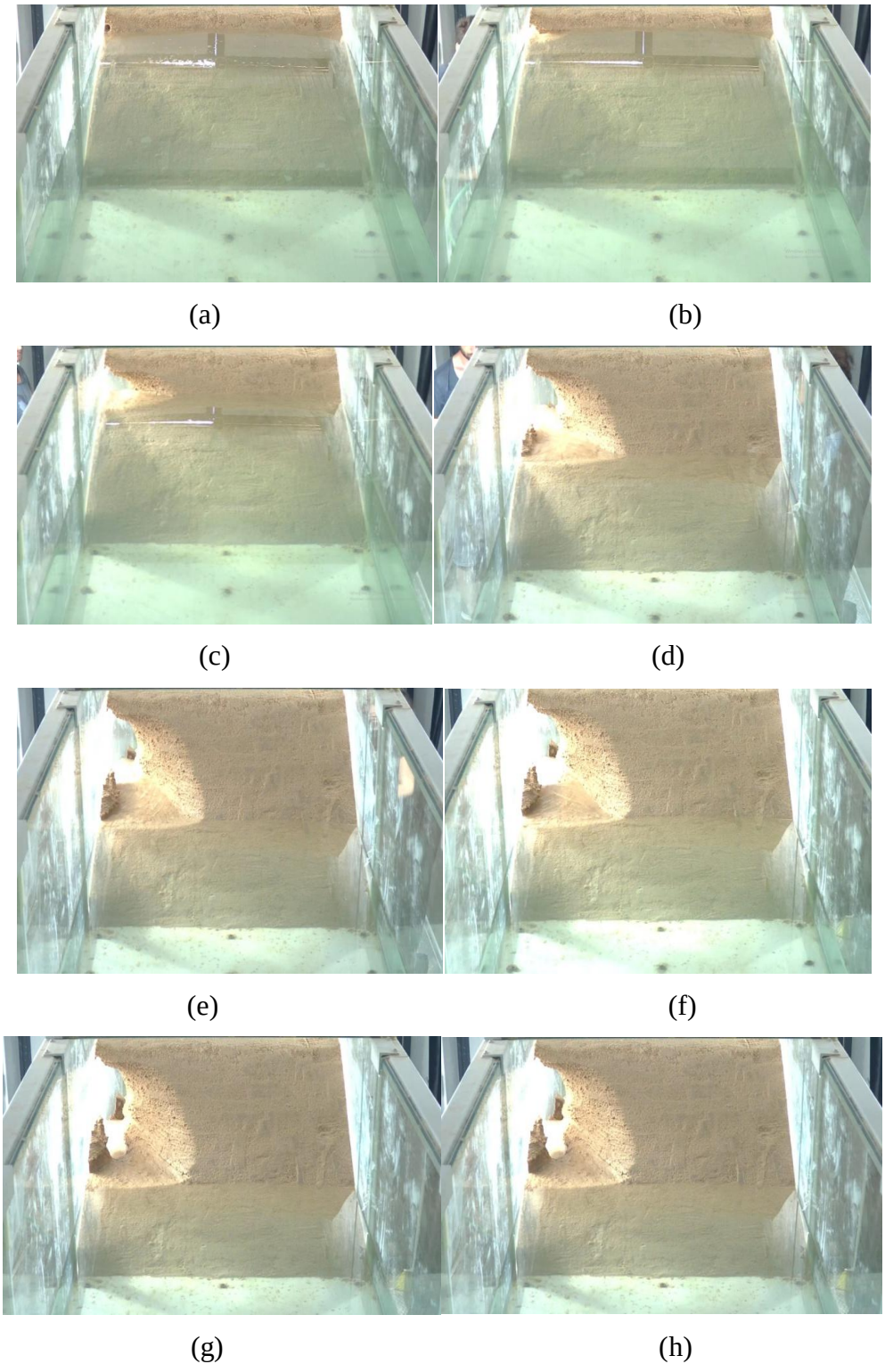

Figure 7.2. The temporal development of the breach at upstream a) t=0 s, b) t=220 s, c) t=340s d) t=680 s, e) t=1020 s f) t=1360 s, g) t=1700s, h) t=2040 s

(a)

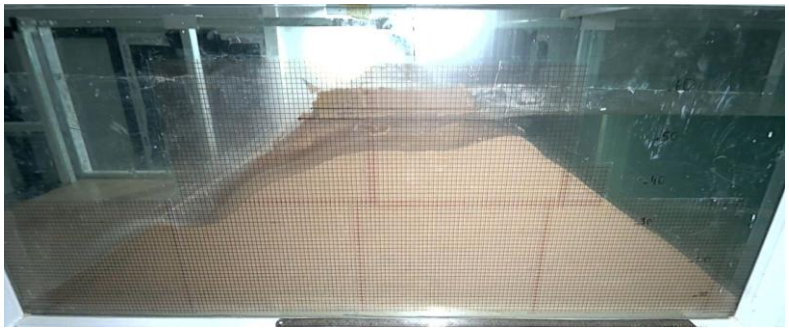

(b)

(c)

(d)

Figure 7.3. The temporal development of the breach at lateral side a) t=0 s, b) t=220 s, c) t=340s d) t=680 s, e) t=1020 s f) t=1360 s, g) t=1700s

(cont. on next page)

(e)

(f)

(g)

Figure 7.3. (cont.)

The temporal water depths in the channel and discharge through the breach calculated by the Equation 7.1 are shown in Figure 7.4 and Figure 7.5, respectively.

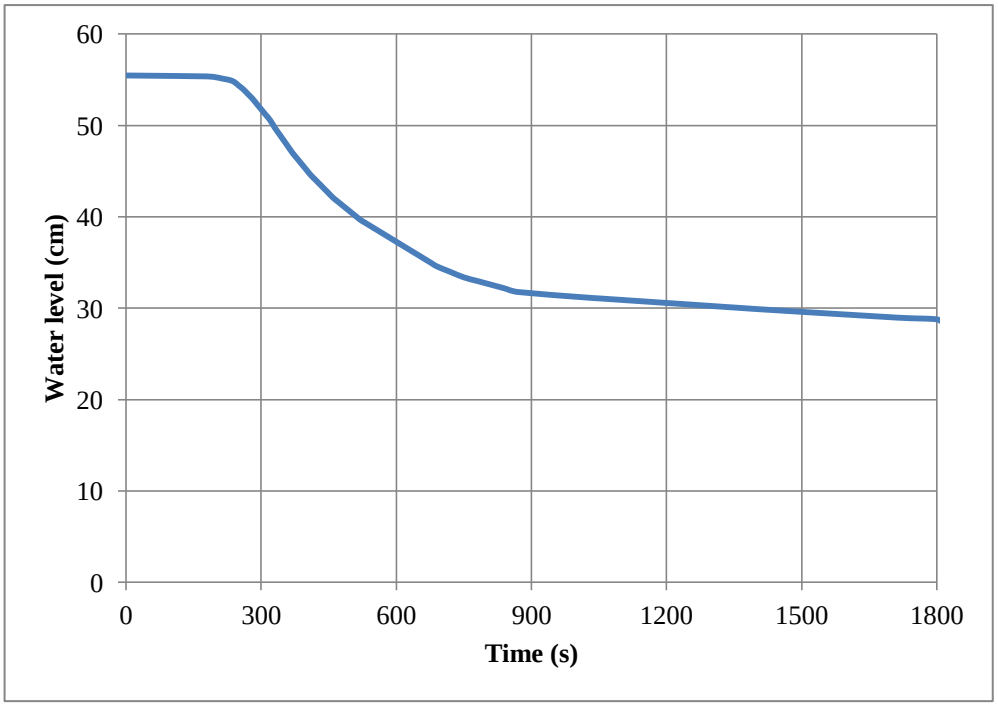

Figure 7.4. Time-varied water depths in channel

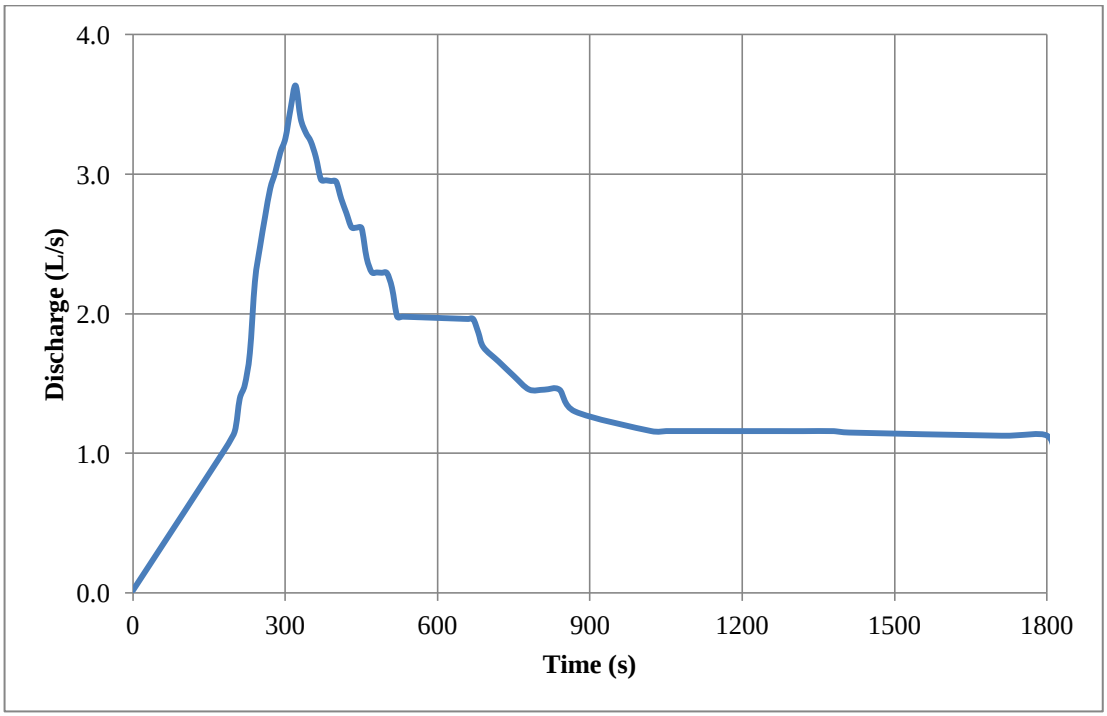

Figure 7.5. Time-varied average discharge through the breach

The temporal variations of the breach area at downstream, upstream and right side are given in the Figure 7.6.

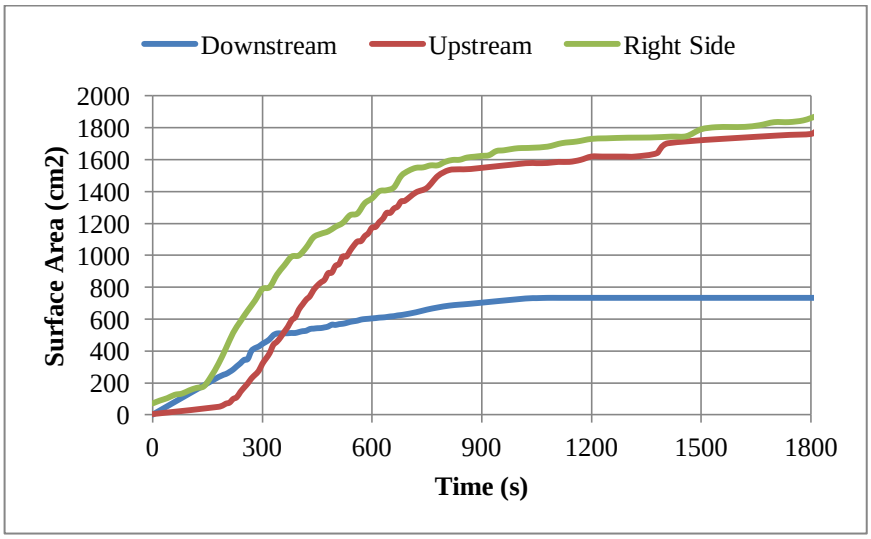

Figure 7.6. Temporal variations of the breach area at downstream, upstream and right side

Besides, the time dependent wetted area and velocity values obtained by using the Equation 7.2 at upstream and downstream are presented in Figure 7.7 and Figure 7.8, respectively.

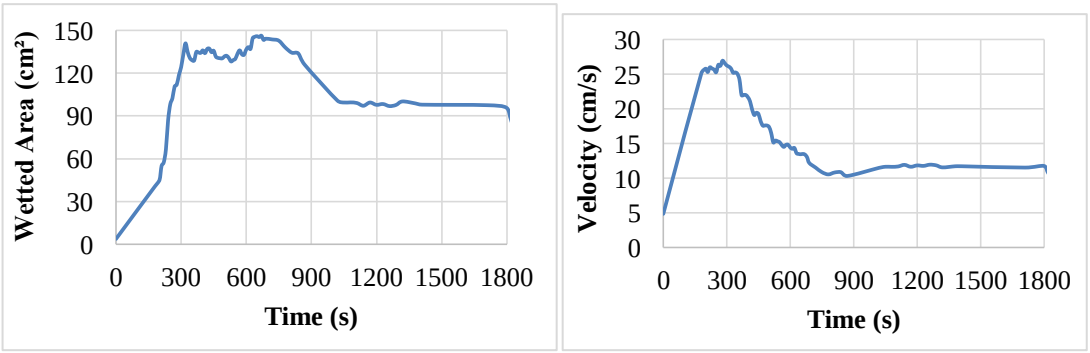

(a) (b)

Figure 7.7. (a) Wetted area and (b) velocity values at upstream

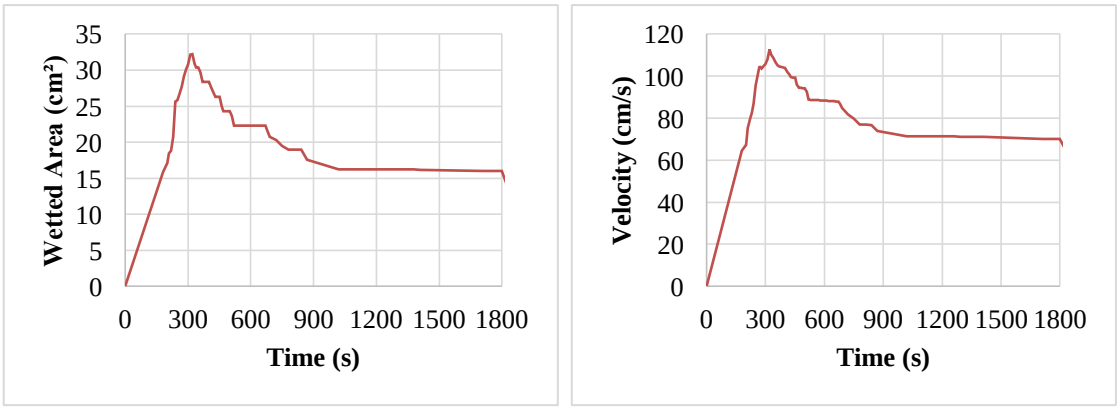

(a) (b)

Figure 7.8. (a) Wetted area and (b) velocity values at downstream

The discharges through the breach corresponding to different instants were calculated using the continuity equation. The boundary coordinates of the breach surface areas and wet areas of the breach were obtained by using the Get-Data Graph Digitizer, and the areas at each time were calculated by applying the Gauss-area function of these obtained coordinates. The time-dependent velocity values through the breach areas were also calculated. During the experiment, it was observed that the breach started on the downstream side and then developed towards to upstream side. The maximum discharge through the breach was calculated as Q_{breach}=3.64 L/s at t=320 s. The breach surface area of the upstream was recorded at a maximum level of A_{ups}=1760 cm^2 at t =1800 s, while downstream A_{down}= 732 cm^2 at t=1080 s and remained unchanged, also $A_{lateral}$= 1875 cm^2 at t=1800 s. Reached maximum wetted area was found to be $A_{wetted\text{-}ups}$=146 cm^2 at t=670 s, $A_{wetted\text{-}downs}$=32 cm^2 at t=320 s. The maximum velocity values through the breach were calculated as V_{ups}=27 cm/s at t=280 s and V_{down}=113 cm/s at t=320 s. The pump was turned off and the experiment was terminated at t=1800 s.

7.2. Second Scenario

The second scenario was applied by trimming and then building only the breach part of the dam constructed for the first scenario. In order to generate the formation of

the breach, a circular hole of 2 cm diameter lying from upstream to downstream was created at 54 cm from the bottom and at the middle of the dam body. The experiment was started when the water in the flume reached this level and passed through the hole. The temporal developments of the breach recorded by the cameras located at downstream and upstream of the dam are given in Figure 7.9 and Figure 7.10, respectively. The time t=0 corresponds to the starting of the seepage.

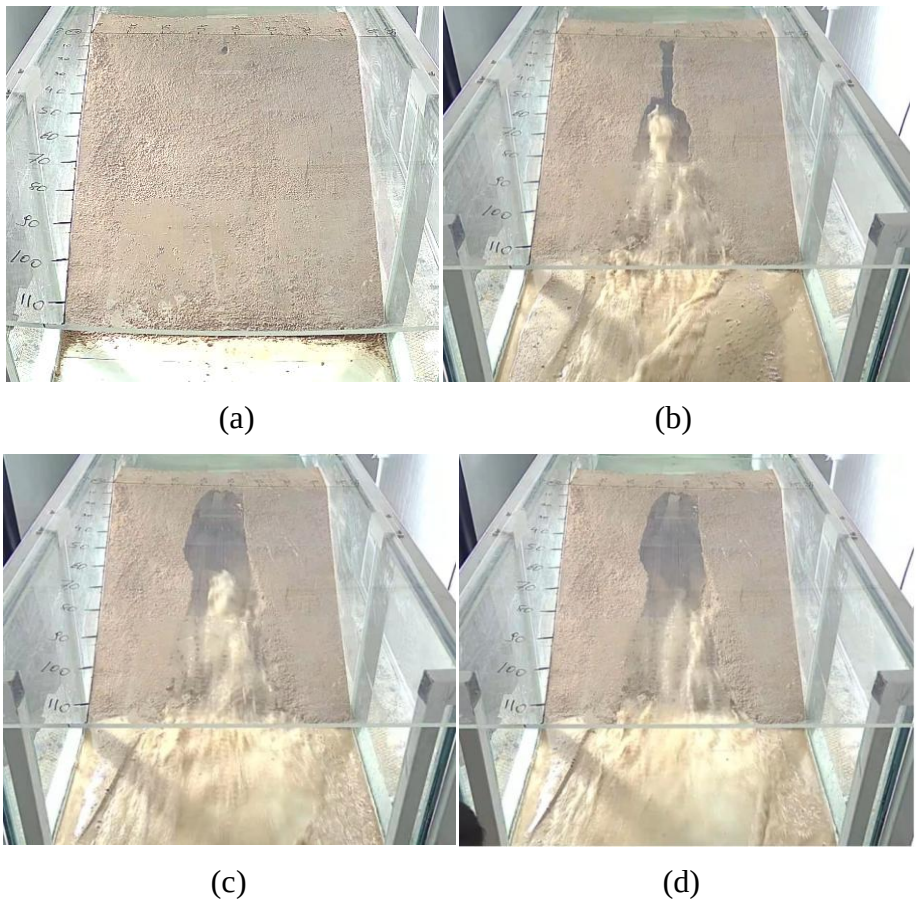

(a) (b)

(c) (d)

Figure 7.9. The temporal development of the breach at downstream a) t=0 s, b) t=140 s, c) t=180s d) t=220 s, e) t=280s, f) t=420s, g) t=560s, h) t=780s

(cont. on next page)

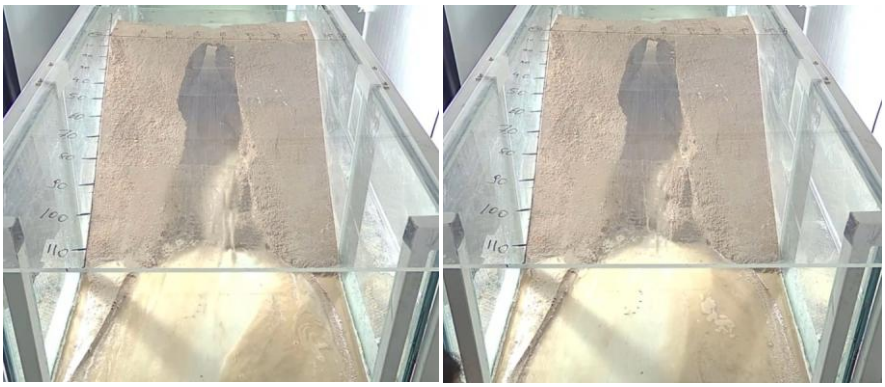

(e) (f)

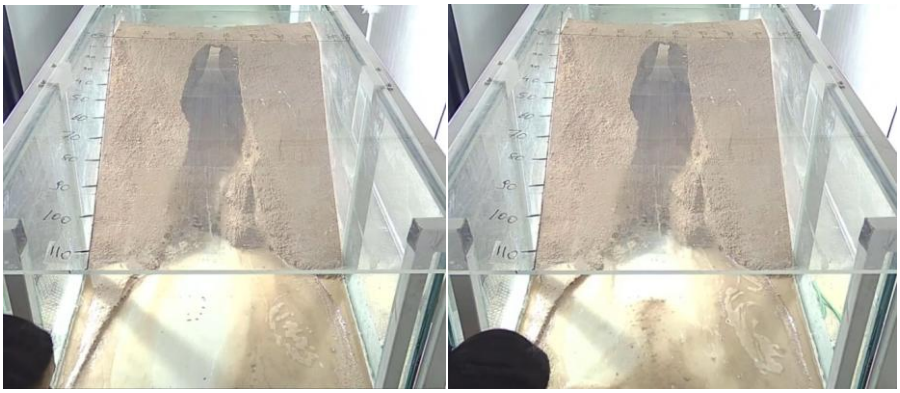

(g) (h)

Figure 7.9. (cont.)

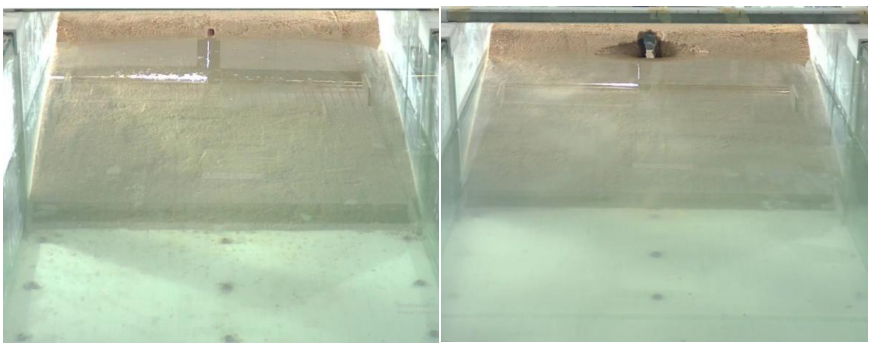

(a) (b)

Figure 7.10. The temporal development of the breach at upstream a) t=0 s, b) t=140 s, c) t=180s d) t=220 s, e) t=280s, f) t=420s, g) t=560s, h) t=780s

(cont. on next page)

(c) (d)

(e) (f)

(g) (h)

Figure 7.10. (cont.)

The temporal water depths in the channel and discharge through the breach calculated by the Equation 7.1 are given in Figure 7.11 and Figure 7.12, respectively.

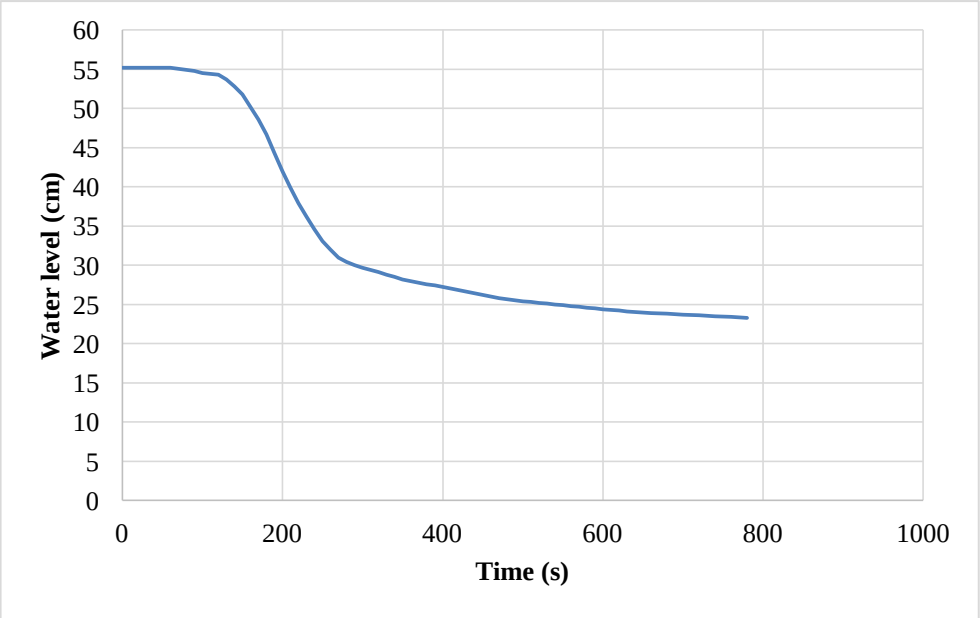

Figure 7.11. Time-varied water depths in channel

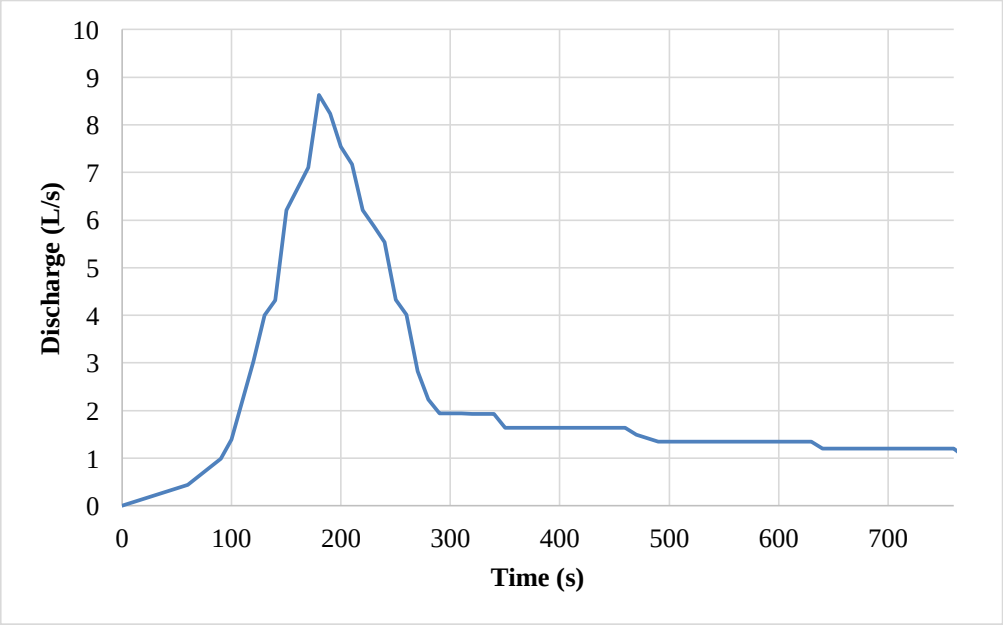

Figure 7.12. Time-varied discharge through the breach

The temporal variations of the breach area at downstream and upstream are shown in the Figure 7.13.

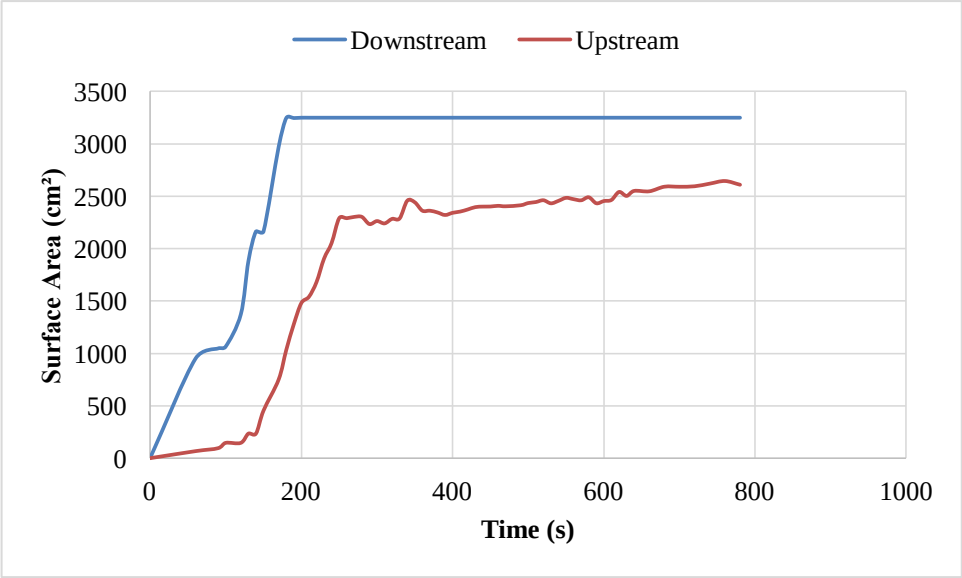

Figure 7.13. Temporal variations of the breach area at downstream and upstream

The time-dependent wetted area and velocity values obtained by using the Equation 7.2 at upstream and downstream are given in Figure 7.14 and Figure 7.15, respectively.

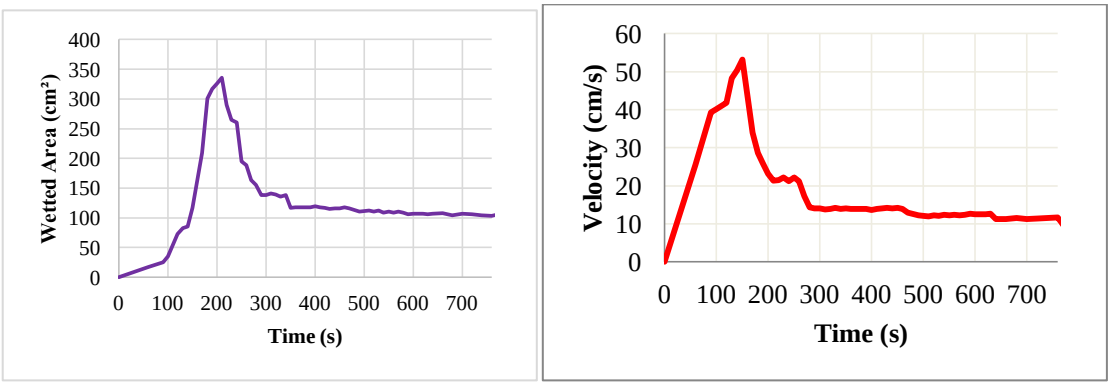

(a) (b)

Figure 7.14. (a) Wetted area and (b) velocity values at upstream

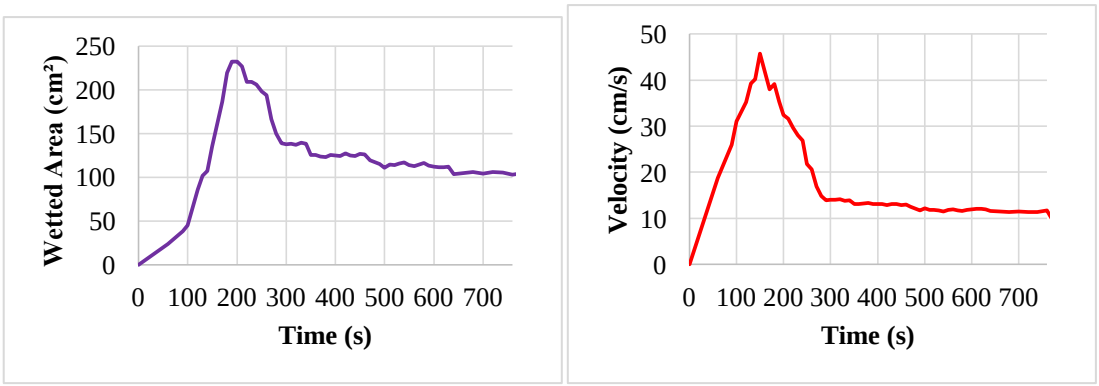

(a) (b)

Figure 7.15. (a) Wetted area and (b) velocity values at downstream

The discharges through the breach corresponding to different instants were calculated using the continuity equation. The boundary coordinates of the breach surface areas and wet areas of the breach were obtained by using the Get-Data Graph Digitizer, and the areas at each time were calculated by applying the Gauss-area function of these obtained coordinates. The time-dependent velocity values through the breach areas were also calculated. During the experiment, it was observed that the breach started on the downstream side and then developed towards to upstream side. The maximum discharge through the breach was calculated as Q_{breach}=8.62 L/s at t=180 s. The breach surface area of the upstream was recorded at a maximum level of A_{ups}=2643 cm^2 at t=780 s, while downstream A_{down}= 3247 cm^2 at t=200 s and remained unchanged. Reached maximum wetted area was found to be $A_{wetted\text{-}ups}$=336cm^2 at t=210 s, $A_{wetted\text{-}downs}$=233 cm^2 at t=190 s. The maximum velocity values through the breach were calculated as V_{ups}=53.2 cm/s at t=150 s and V_{down}=45.8 cm/s at t=150 s. The pump was turned off at t=1800 s, and the experiment was terminated at t=780 s, and then the experiment was terminated.

7.3. Third Scenario

In the third scenario, a new dam was constructed with a circular hole at the 54-cm level and the middle of the dam. To generate the formation of the breach, a circular

hole of 2 cm diameter lying from upstream to downstream was created at 54 cm from the bottom of the dam body. The experiment was started when the water in the flume reached this level and passed through the hole. The temporal developments of the breach recorded by the cameras located at downstream and upstream of the dam are given in Figure 7.16 and Figure 7.17, respectively. The time t=0 corresponds to the starting of the seepage.

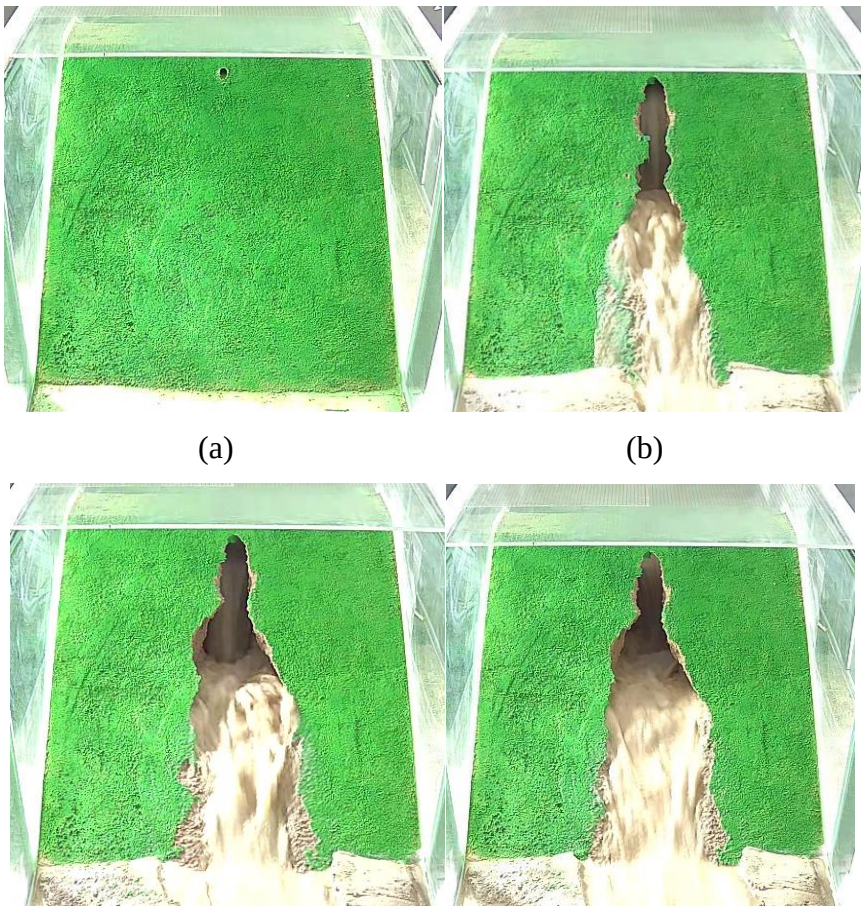

(a) (b)

(c) (d)

Figure 7.16. The temporal development of the breach at downstream a) t=0, b) t=180, c) t=230 s, d) t=280 s, e) t=340 s, f) t= 380 s, g) t=410 s, h) t= 570 s

(cont. on next page)

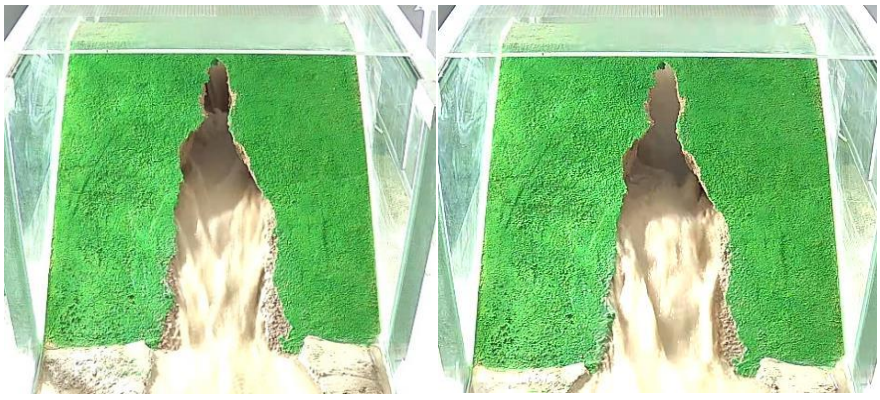

(e) (f)

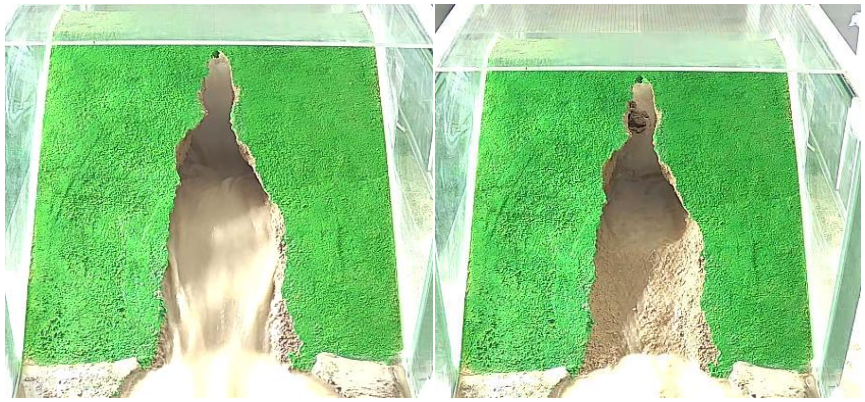

(g) (h)

Figure 7.16. (cont.)

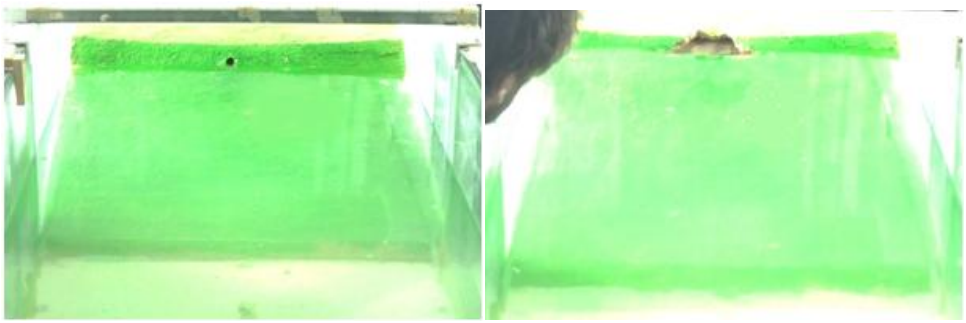

(a) (b)

Figure 7.17. The temporal development of the breach at upstream a) t=0, b) t=180, c) t=230 s, d) t=280 s, e) t=340 s, f) t= 380 s, g) t=410 s, h) t= 570 s

(cont. on next page)

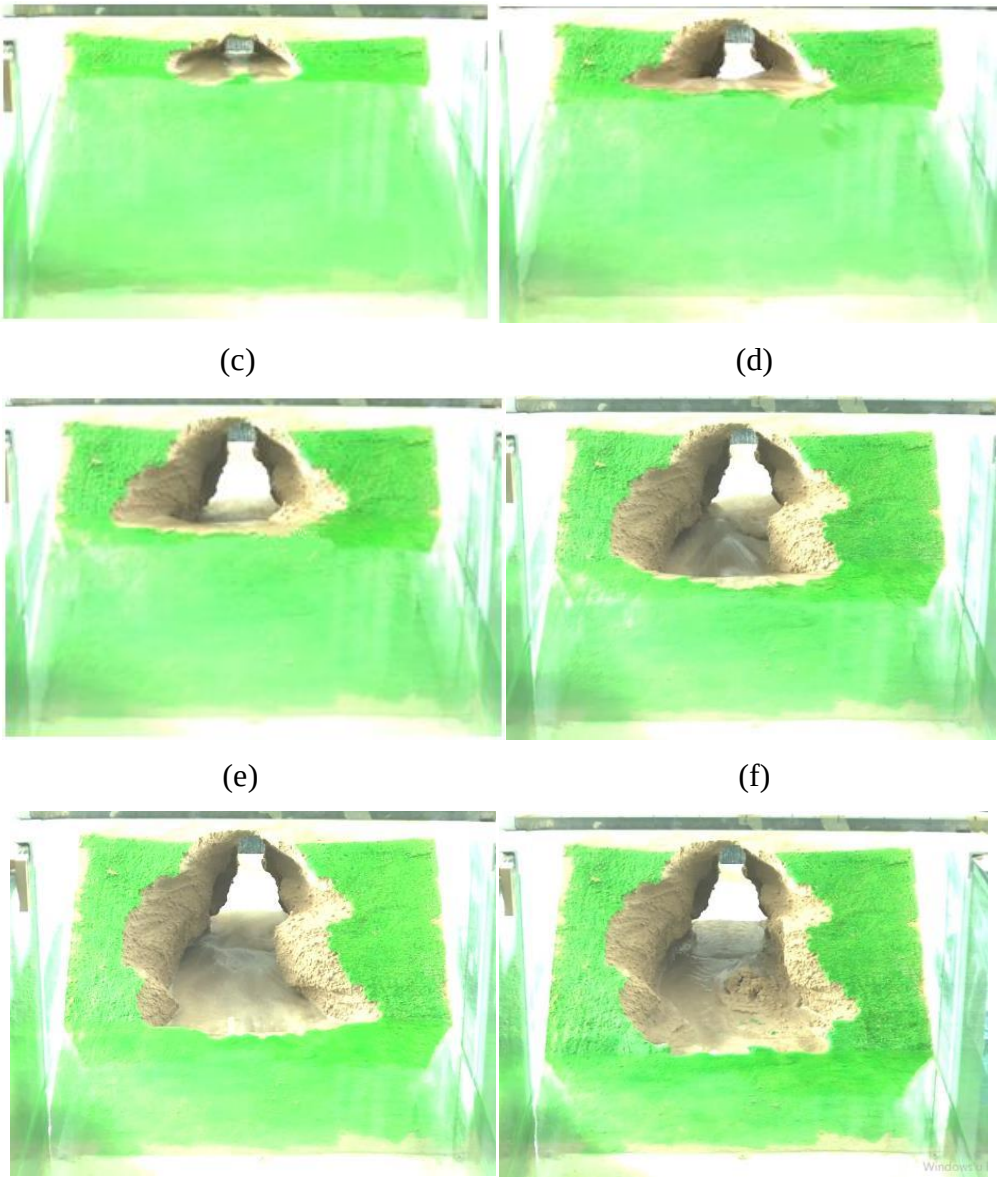

(c) (d)

(e) (f)

(g) (h)

Figure 7.17. (cont.)

The temporal water depths in the channel and discharge through the breach calculated by the Equation 7.1 are given in Figure 7.18 and Figure 7.19, respectively.

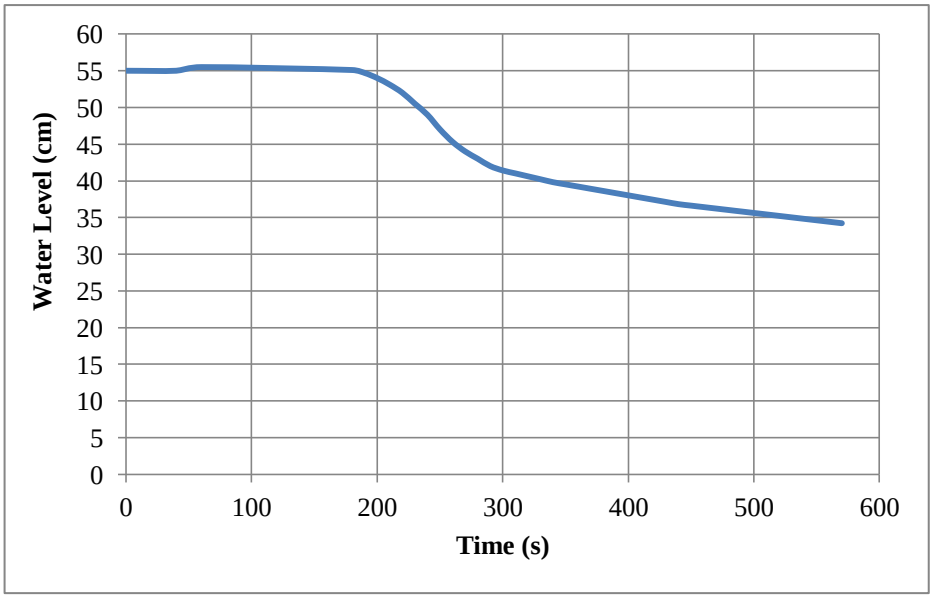

Figure 7.18. Time-varied water depths in channel

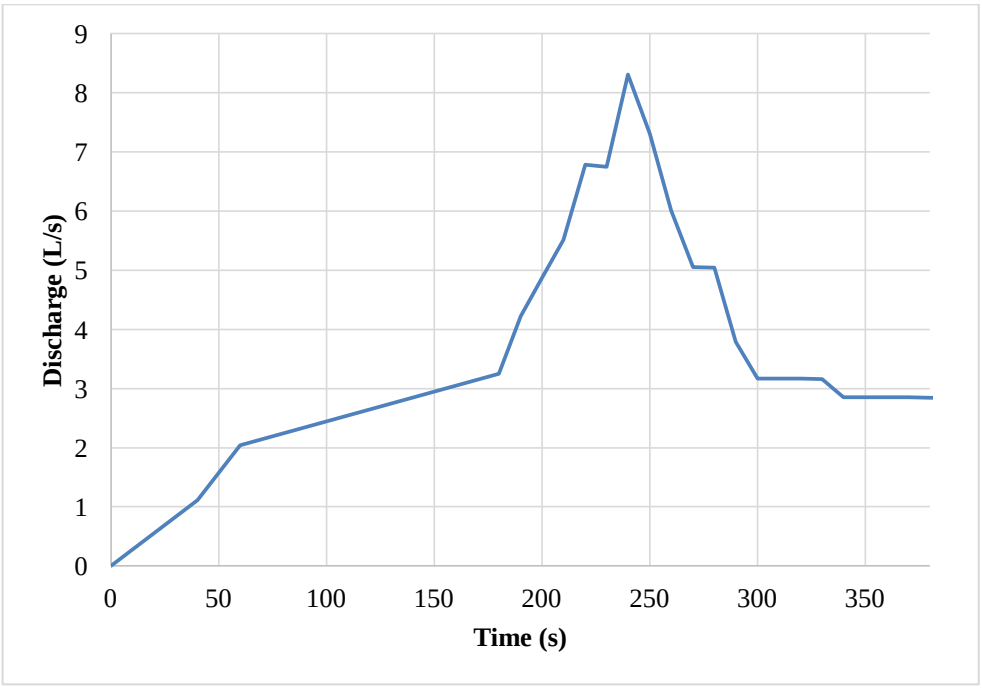

Figure 7.19. Time-varied discharge through the breach

The temporal variations of the breach area at downstream and upstream are shown in the Figure 7.20.

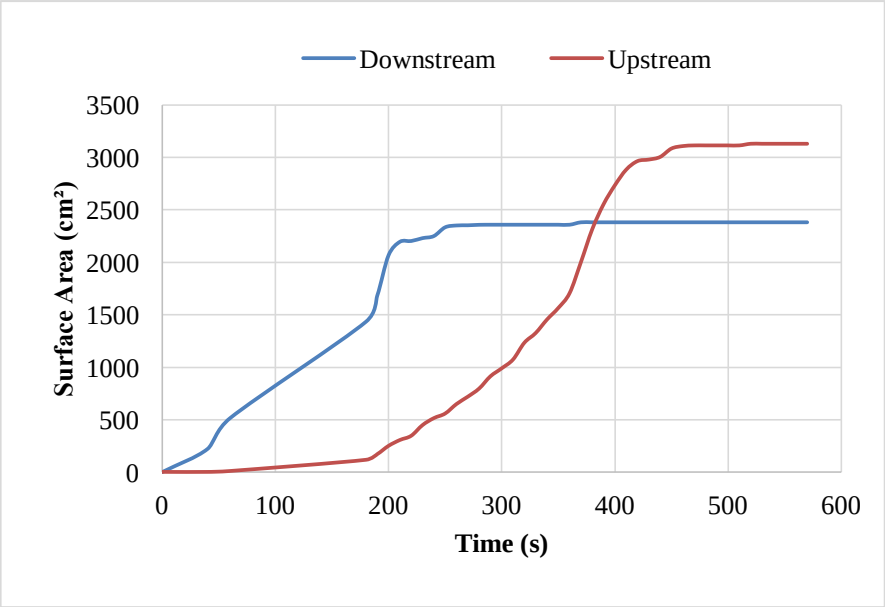

Figure 7.20. Temporal variations of the breach area at downstream and upstream

The time-dependent wetted area and velocity values obtained by using by the Equation 7.2 at upstream and downstream are given in Figure 7.21 and Figure 7.22, respectively.

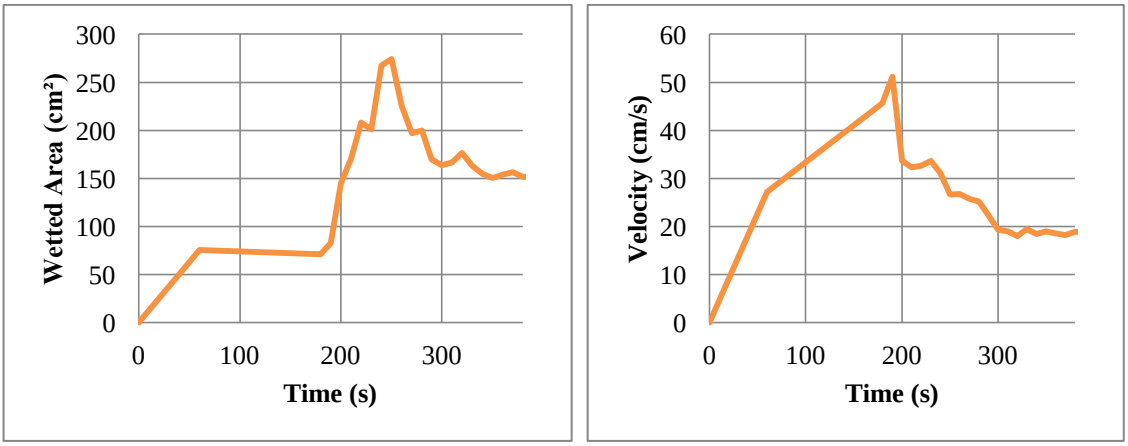

(a) (b)

Figure 7.21. (a) Wetted area and (b) velocity values at upstream

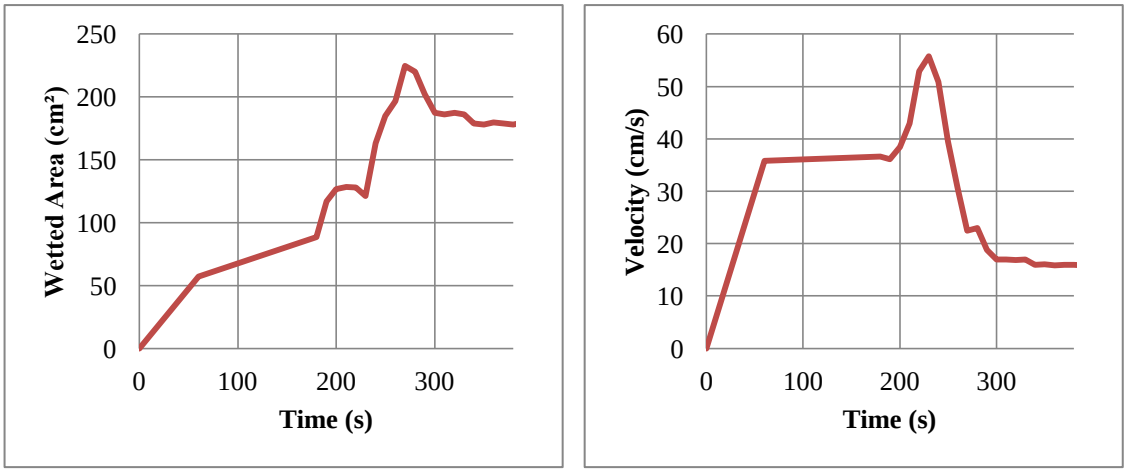

(a) (b)

Figure 7.22 (a) Wetted area and (b) velocity values at downstream

The discharges through the breach corresponding to different instants were calculated using the continuity equation. The boundary coordinates of the breach surface areas and wet areas of the breach were obtained by using the Get-Data Graph Digitizer, and the areas at each time were calculated by applying the Gauss-area function of these obtained coordinates. The time-dependent velocity values through the breach areas were also calculated. During the experiment, the breach initiated on the downstream side and then evolved towards to upstream side. The maximum discharge through the breach was calculated as Q_{breach}=8.31 L/s at t=240 s. The maximum breach surface area at the upstream was found to be A_{ups}= 3128.7 cm^2 at t=520 s, while at downstream A_{down}= 2379.3 cm^2 at t=370 s and remained unchanged afterwards. The maximum wetted areas were $A_{wetted\text{-}ups}$=274 cm^2 at t=250 s and $A_{wetted\text{-}downs}$=225 cm^2 at t=270 s. The maximum velocity values through the breach were calculated as V_{ups}=51.1 cm/s at t=190 s and V_{down}=55.8 cm/s at t=230 s for upstream and downstream, respectively. The pump was turned off at t=380 s, and then the experiment was terminated.

7.4. Comparison of the Experimental Findings

7.4.1. Comparison for the First and the Second Scenarios

While the dam of the second scenario was constructed by repairing the breach part of the dam exposed to an experiment and includes the initial hole at the middle of the dam, the dam of the first scenario was constructed from the beginning with an initial hole at the right side of the dam. Therefore, during the experiment, while a half breach occurs in the first scenario, a full breach evolves in the second scenario, so that the experimental findings are obtained accordingly.

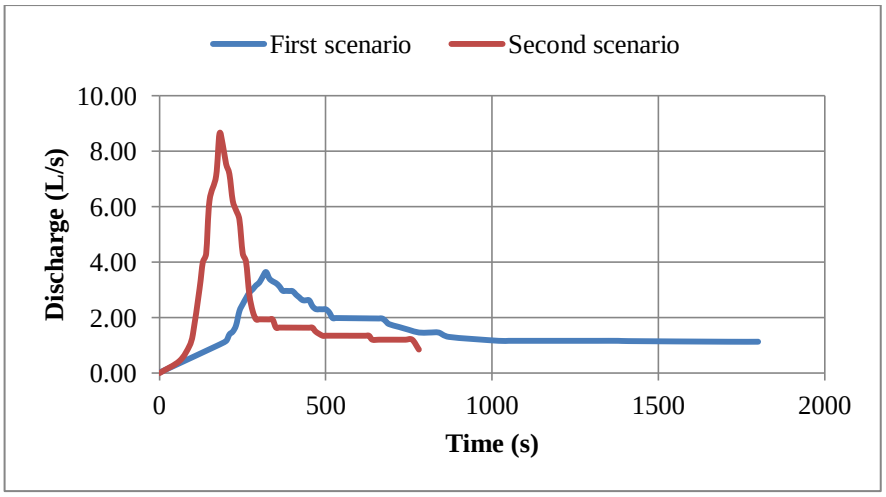

Figure 7.23. Comparison of the discharge through the breach for the first and the second scenarios

When the discharge through the breach for the scenarios are compared with each other, it can be said that the peak discharge value of the second scenario is almost twice of the first scenario, and the second scenario reaches the peak discharge in a shorter time as shown in Figure 7.23.

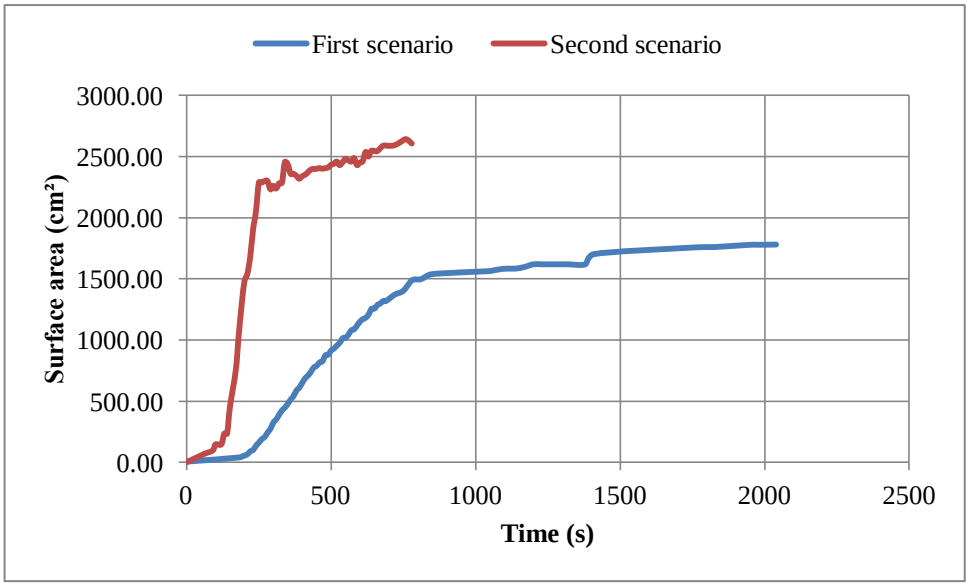

Figure 7.24. Comparison of the upstream surface areas for the first and the second scenarios

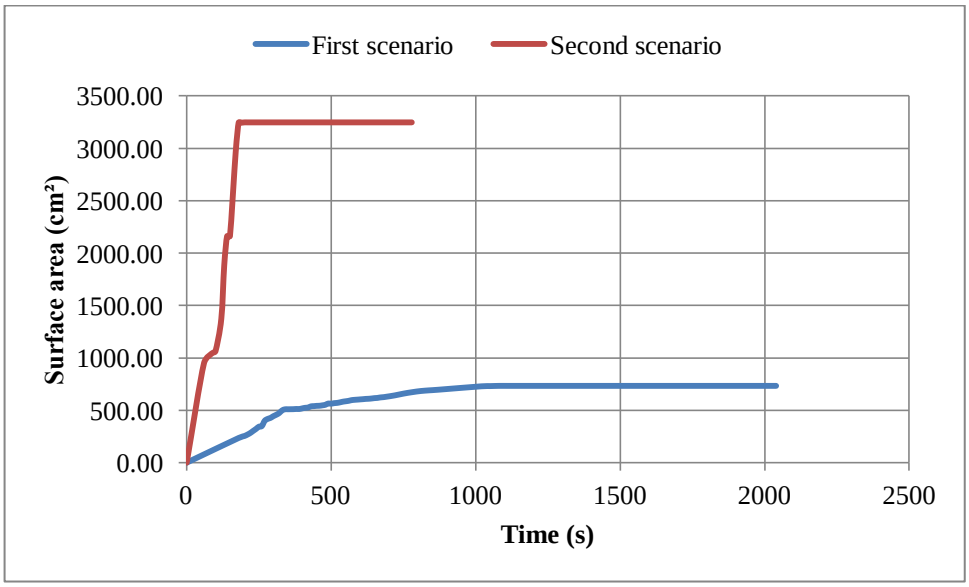

Figure 7.25. Comparison of the downstream surface areas for the first and the second scenarios

When the surface areas for the scenarios are compared with each other for upstream, it can be said that the maximum surface area value of the second scenario is one and half times that of the first scenario, and the second scenario reaches the maximum surface area in a shorter time as shown in Figure 7.24.

When the surface areas for the scenarios are compared with each other for downstream, it can be said that the maximum surface area value of the second scenario

is almost four and half times of the first scenario, and the second scenario reaches the maximum surface area in a shorter time as shown in Figure 7.25.

When the wetted areas for the scenarios are compared with each other for upstream, it can be said that the maximum wetted area value of the second scenario is almost twice of the first scenario, and the second scenario reaches the maximum wetted area in a shorter time as shown in Figure 7.26.

When the wetted areas for the scenarios are compared with each other for downstream, it can be said that the maximum wetted area value of the second scenario is almost seven times of the first scenario, and the second scenario reaches the maximum wetted area in a shorter time as shown in Figure 7.27.

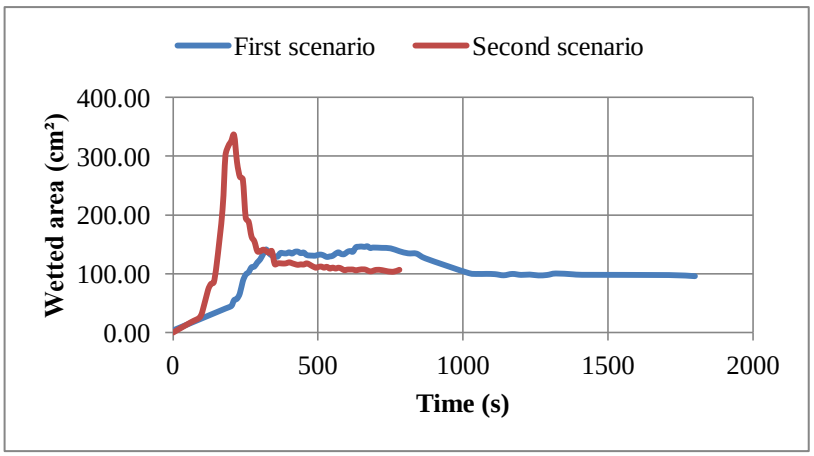

Figure 7.26. Comparison of the upstream wetted areas for the first and the second scenarios

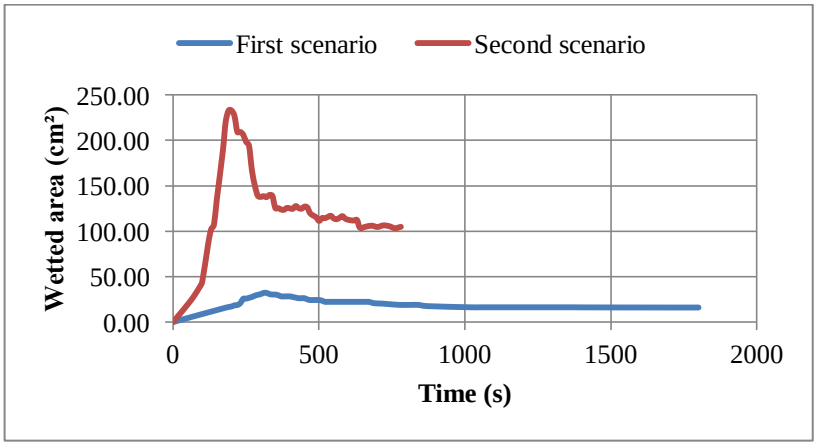

Figure 7.27. Comparison of the downstream wetted areas for the first and the second scenarios

When the velocity values for the scenarios are compared with each other for both upstream and downstream, it can be said that the second scenario reaches the maximum velocity in a shorter time as shown in Figure 7.28 and Figure 7.29. The maximum velocity value of the second scenario is twice of the first scenario for upstream, however, for downstream, the maximum velocity value of the first scenario is two and half times of the second scenario.

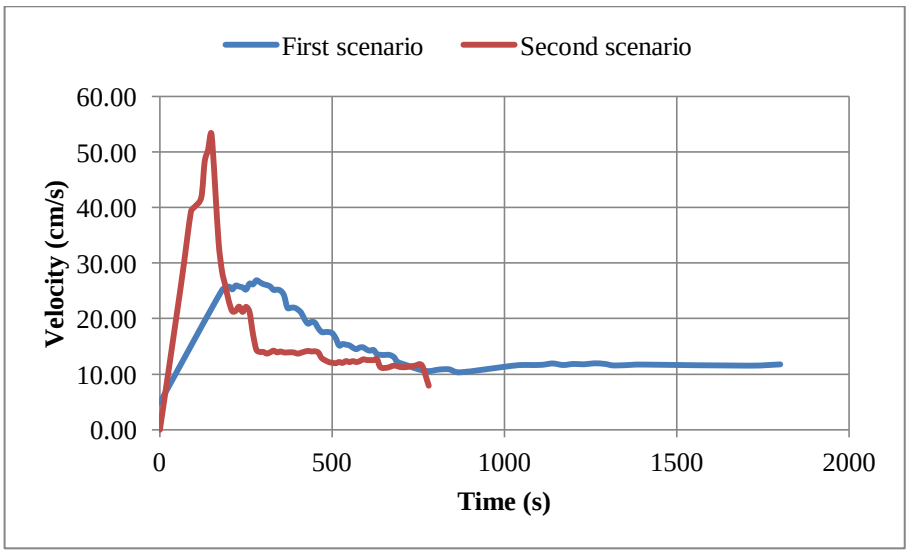

Figure 7.28. Comparison of the upstream velocities for the first and the second scenarios

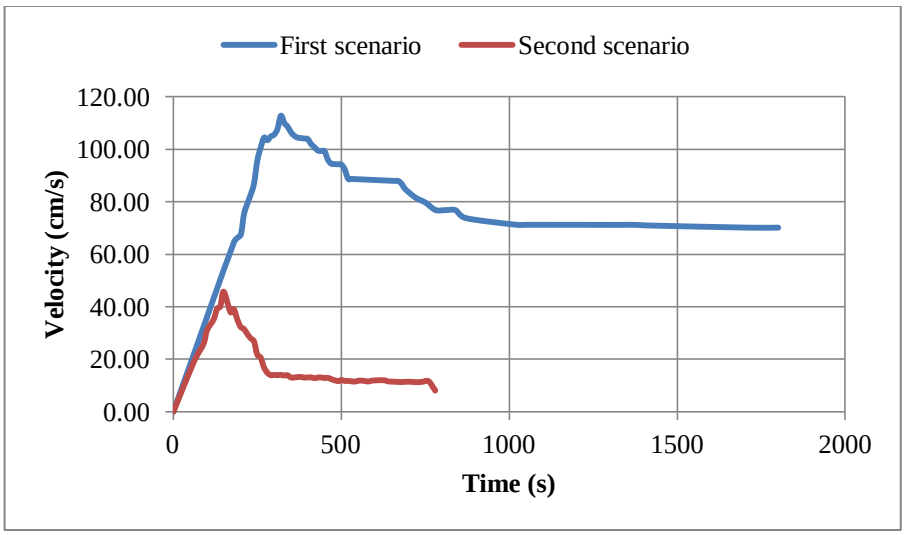

Figure 7.29. Comparison of the downstream velocities for the first and the second scenarios

7.4.2. Comparison for the First and the Third Scenarios

While the initial hole of the dam exists at the glass top side of the first scenario, the third scenario possesses its initial hole at the middle top of the dam and for both of the scenarios; dams were constructed from the beginning. Therefore, during the experiment, while a half breach occurs in the first scenario, a full breach evolves in the third scenario, so that the experimental findings are obtained accordingly.

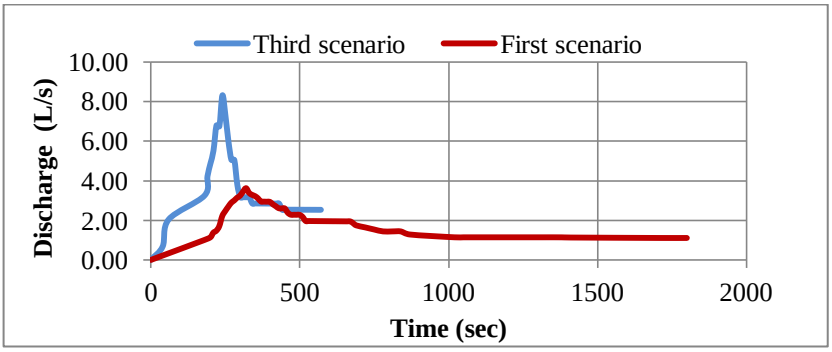

Figure 7.30. Comparison of the discharge through the breach for the first and the third scenarios

When the discharge through the breach for the scenarios are compared with each other, it can be said that the peak discharge value of the third scenario is almost twice of the first scenario, and the third scenario reaches the peak discharge in a shorter time as shown in Figure 7.30.

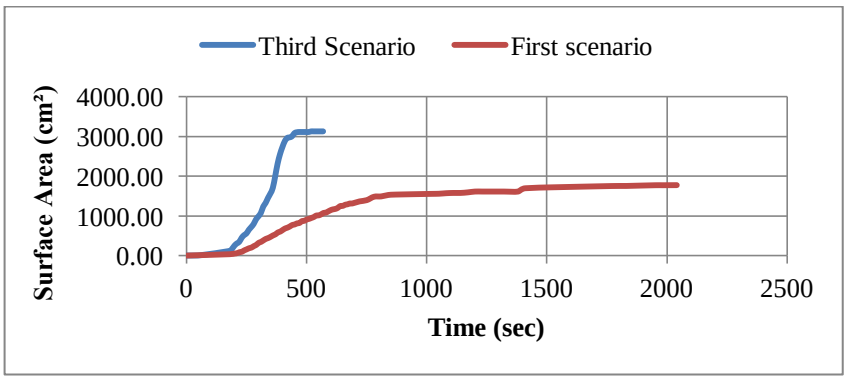

Figure 7.31. Comparison of the upstream surface areas for the first and the third scenarios

When the surface areas for the scenarios are compared with each other for upstream, it can be said that the maximum surface area value of the third scenario is almost twice of the first scenario, and the third scenario reaches the maximum surface area in a shorter time as shown in Figure 7.31.

When the surface areas for the scenarios are compared with each other for downstream, it can be said that the maximum surface area value of the third scenario is almost three times of the first scenario, and the third scenario reaches the maximum surface area in a shorter time as shown in Figure 7.32.

When the wetted areas for the scenarios are compared with each other for upstream, it can be said that the maximum wetted area value of the third scenario is almost twice of the first scenario, and the third scenario reaches the maximum wetted area in a shorter time as shown in Figure 7.33.

When the wetted areas for the scenarios are compared with each other for downstream, it can be said that the maximum wetted area value of the third scenario is almost seven times of the first scenario, and the third scenario reaches the maximum wetted area in a shorter time as shown in Figure 7.34.

When the velocity values for the scenarios are compared with each other for both upstream and downstream, it can be said that the third scenario reaches the maximum velocity in a shorter time as shown in Figure 7.35 and Figure 7.36. The maximum velocity value of the third scenario is almost twice of the first scenario for upstream, however, for downstream, the maximum velocity value of the first scenario is twice of the third scenario.

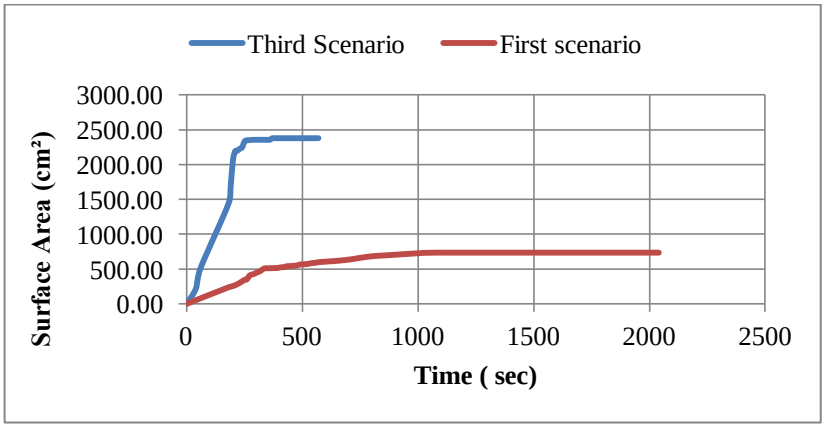

Figure 7.32. Comparison of the downstream surface areas for the first and the third scenarios

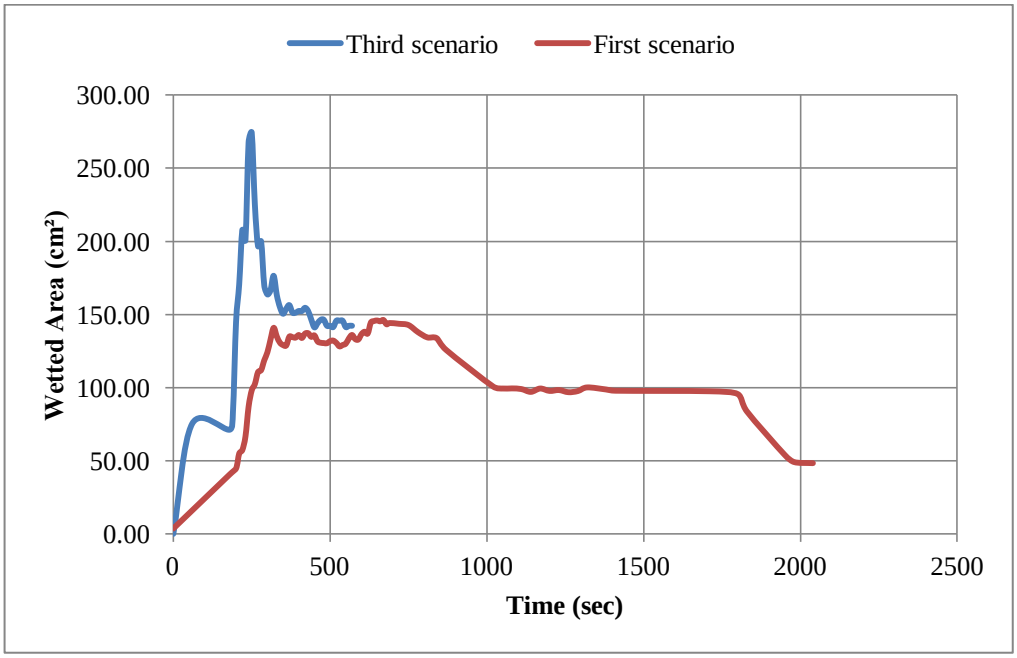

Figure 7.33. Comparison of the upstream wetted areas for the first and the third scenarios

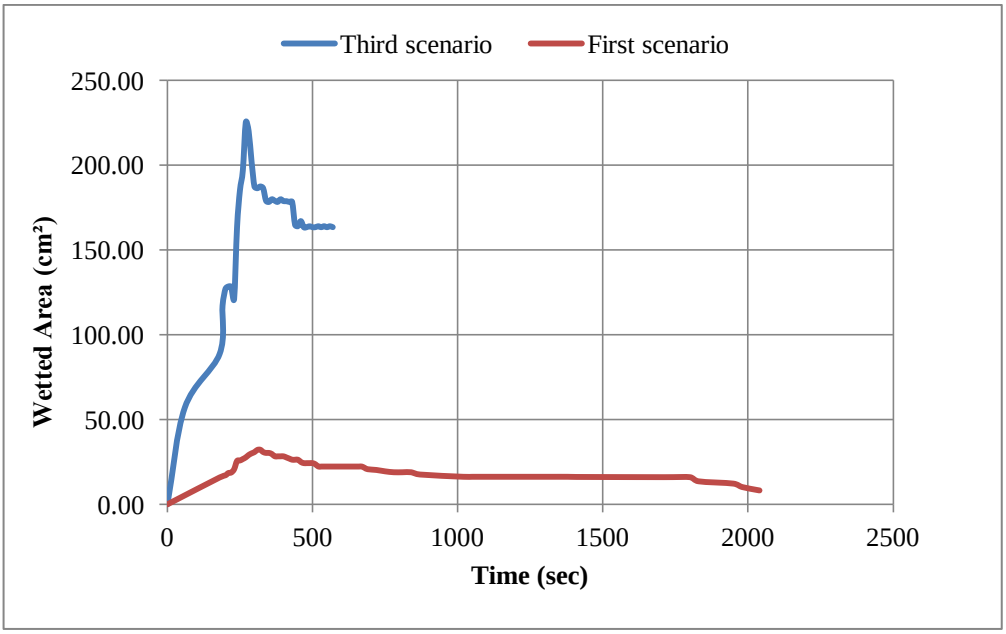

Figure 7.34. Comparison of the downstream wetted areas for the first and the third scenarios

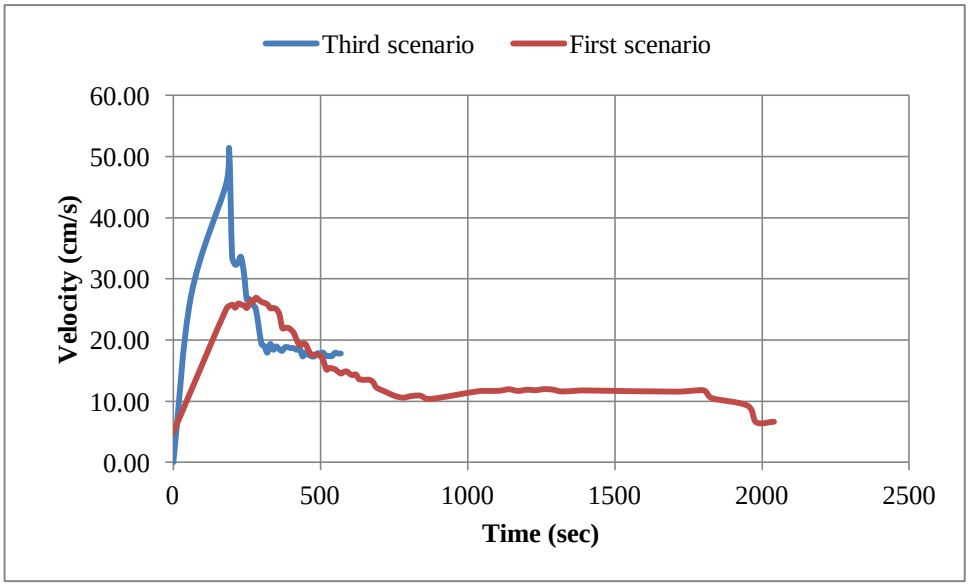

Figure 7.35. Comparison of the upstream velocities for the first and the third scenarios

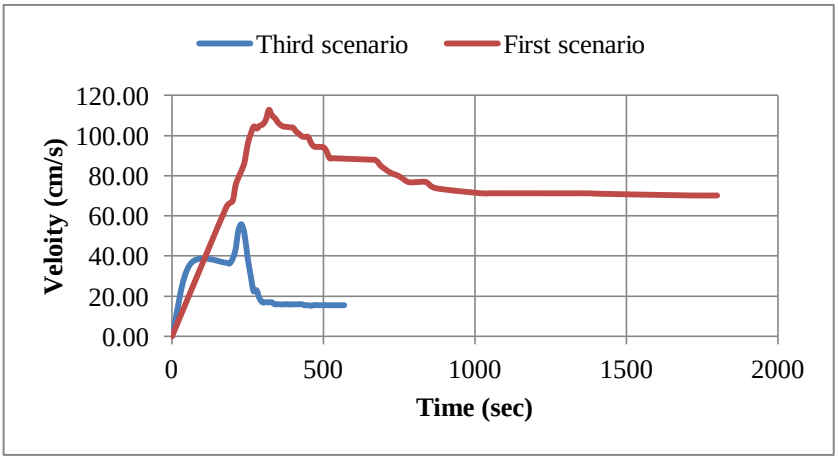

Figure 7.36. Comparison of the downstream velocities for the first and the third scenarios

7.4.3. Comparison for the Second and the Third Scenarios

While the dam of the second scenario was constructed by repairing the breach part of the dam exposed to an experiment, the dam of the third scenario was constructed from the beginning with an initial hole at the middle of the dam. When the discharge through the breach for the scenarios are compared with each other, it can be said that the

peak discharge values are close to each other, however, the second scenario has a little more and the dam of the second scenario reaches the peak discharge in a shorter time as shown in Figure 7.37.

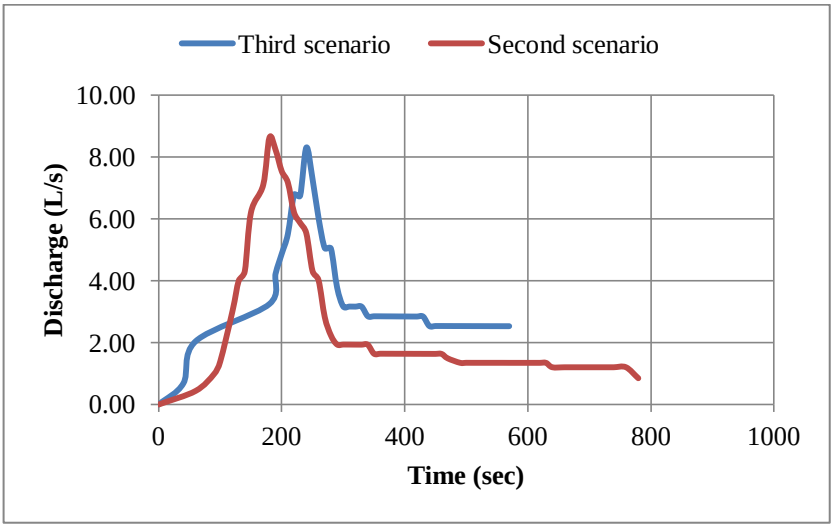

Figure 7.37. Comparison of the discharge through the breach for the second and the third scenarios

When the surface areas are compared, the maximum surface area at upstream has been observed for the third scenario (Figure 7.38) and the maximum surface area at downstream has been observed for the second scenario (Figure 7.39). This situation can be corresponding from material caving during the second scenario experiment (Figure 7.40). The repair process may have resulted in reduced resistance to erosion.

When the wetted areas for the scenarios for both upstream and downstream are compared with each other, it can be said that maximum wetted area values are close to each other, however, the second scenarios has a little more and the dam of the second scenario reaches the maximum wetted area in a shorter time for both upstream and downstream as shown in Figure 7.41 and Figure 7.42.

When the velocities for the scenarios for upstream are compared with each other, it can be said that maximum velocity values are close to each other, however, the second scenario has a little more and the dam of the second scenario reaches the maximum velocity in a shorter time for upstream as shown in Figure 7.43.

When the velocities for the scenarios for downstream are compared with each other, it can be said that maximum velocity values are close to each other; however, this time the third scenario has a higher value. Nevertheless, the dam of the second scenario again reaches the maximum velocity in a shorter time for downstream as shown in Figure 7.44.

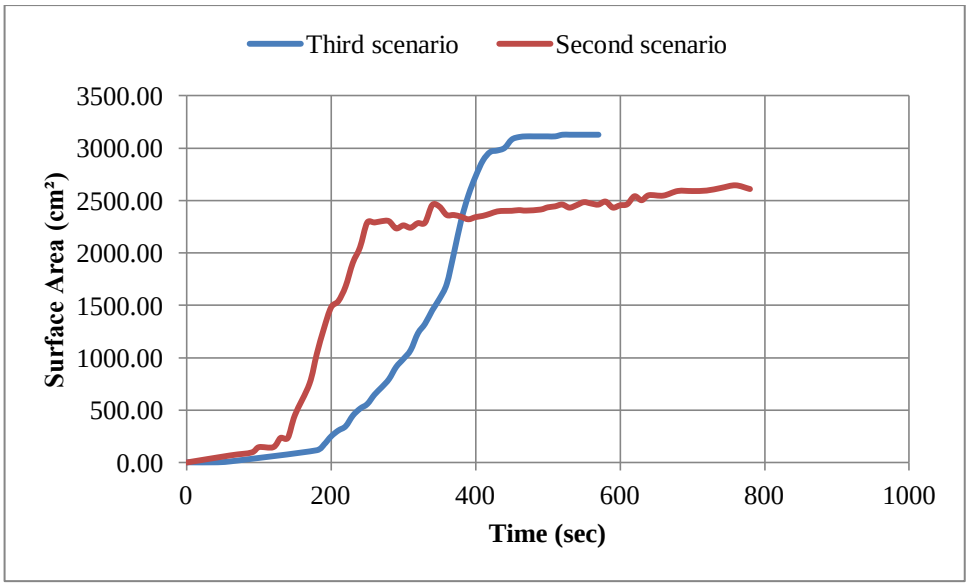

Figure 7.38. Comparison of the upstream surface areas for the second and the third scenarios

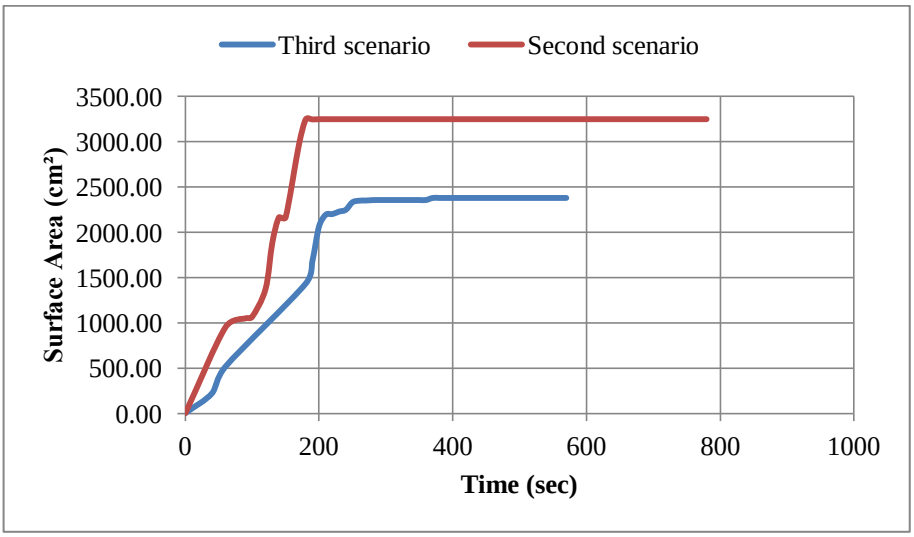

Figure 7.39. Comparison of the downstream surface areas for the second and the third scenarios

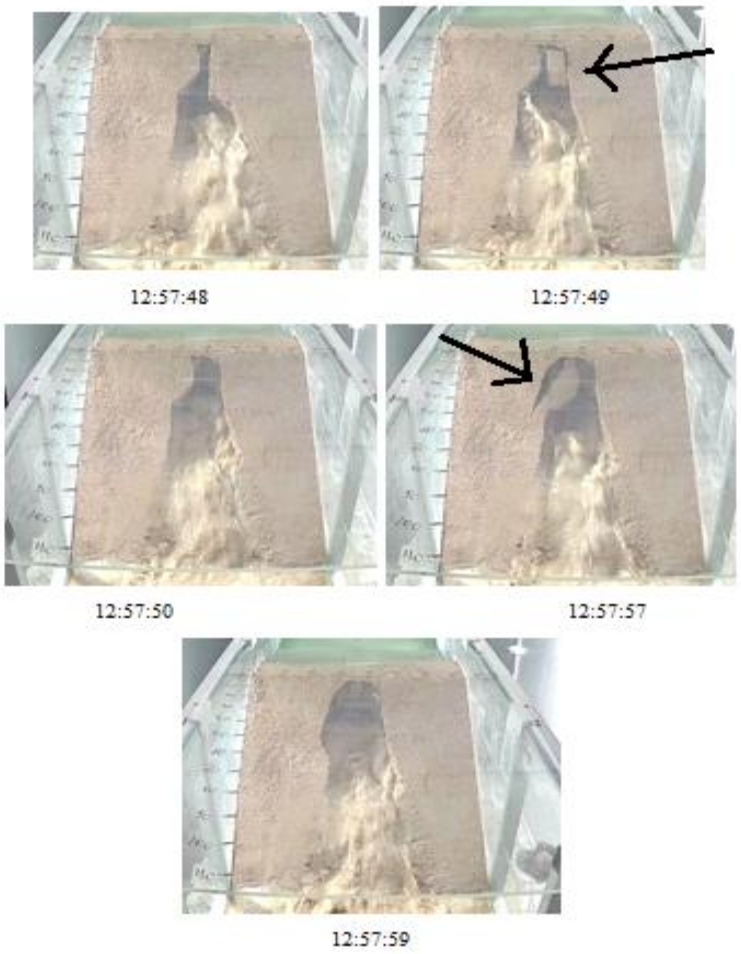

Figure 7.40. Material caving during the second scenario experiment

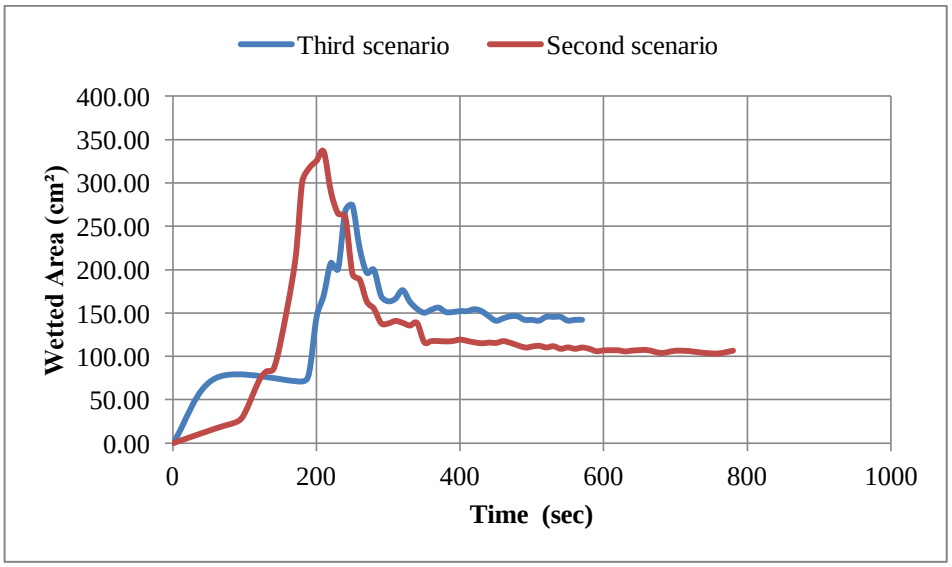

Figure 7.41. Comparison of the upstream wetted areas for the second and the third scenarios

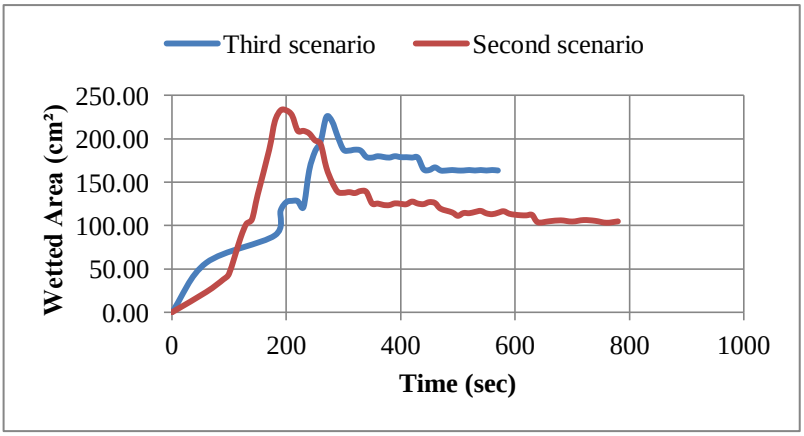

Figure 7.42. Comparison of the downstream wetted areas for the second and the third scenarios

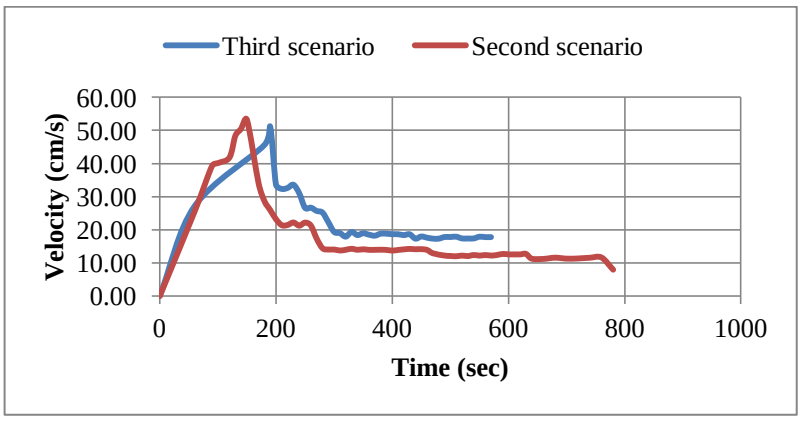

Figure 7.43. Comparison of the upstream velocities for the second and the third scenarios

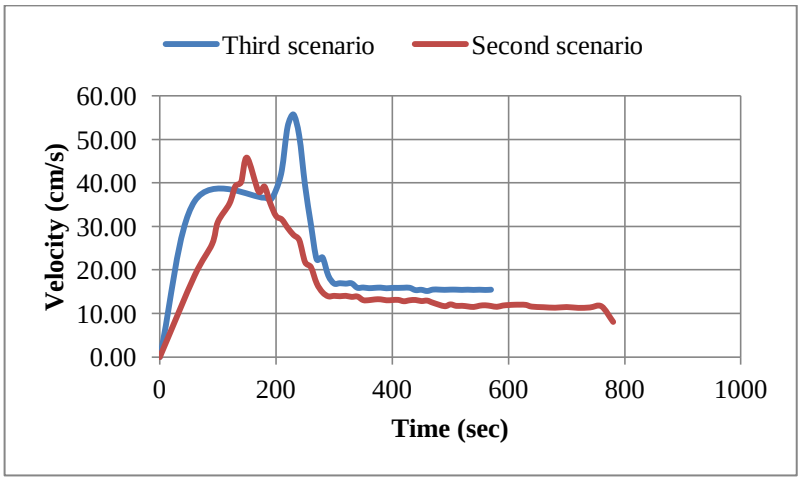

Figure 7.44. Comparison of the downstream velocities for the second and the third scenarios

CHAPTER 8

USE OF IMAGE PROCESSING

8.1. Application of the Image Processing Technique for the First Scenario

The image processing technique was used to monitor the erosion process in the earth-fill dam from the side looking. In this first scenario, a 2 cm-diameter hole was opened on the edge of the glass at the height of 54 cm from the bottom. When the water level reached 54 cm, the passage of water from the hole started and the breach developed over time to open from the bottom of the hole. During the experiment, there is a continuous inflow into the reservoir. The experiment is investigated for the time when the water level changes maximum 10%. (i.e., for the part the water level is almost constant during the experiment). During the experiment, the erosion process was investigated with the camera placed on the glass side. 180 cm × 60 cm side surface was used for the videos to be analyzed. In the pictures, the bottom erosion line edges of the opened breach and the outer surface of the dam were drawn with the Matlab (ROI-Based Processing) “drawpolyline” command using cyan color.

Later, these pictures were recorded and only the cyan color was determined by running the computer code using the function obtained from Matlab Color Thresholder – RGB to recognize the Color preferred by the user in the picture. The bottom erosion line and the outer surface of the dam at the beginning of the experiment were detected separately, and after each detection, the bottom erosion lines at each time were collected with the dam surface at the beginning of the experiment, and the change of the surface depending on the time was also examined. The tonal values of the colors are set as the threshold range [0,151] for channel 1, [202,255] for channel 2, and [204,255] for channel 3. All curves obtained over time were collected in a single graph. Figure 8.1 shows steps in image processing for detaching erosion lines and Figure 8.2 indicates the evaluation of erosion lines at different time instants after image processing.

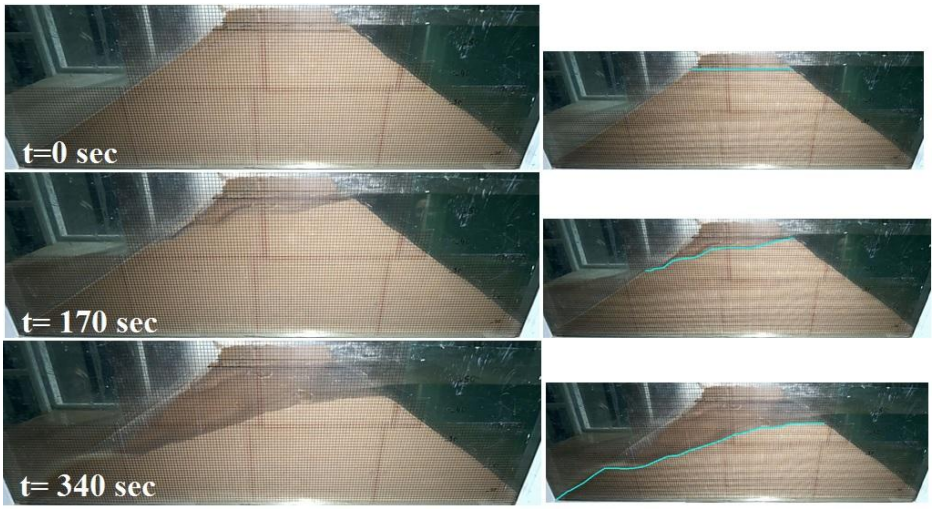

(a) (b)

Figure 8.1. (a) Original figure (b) Detaching of bottom erosion line at different time instants by drawing polylines

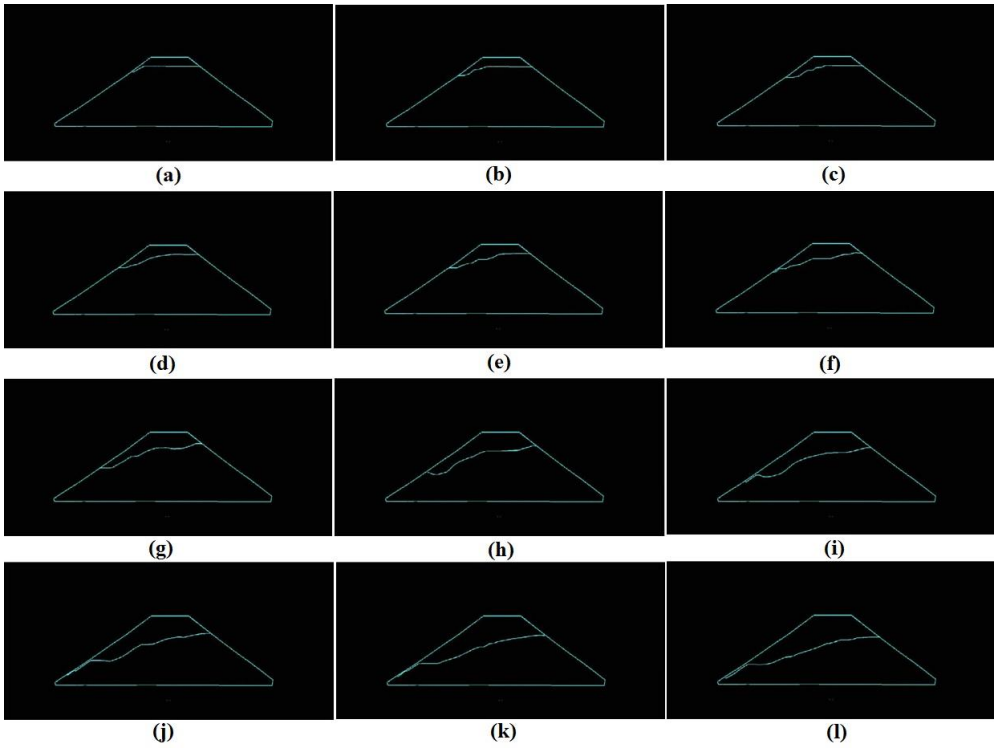

Figure 8.2. The evaluation of erosion lines at different time instants a) t=10 sec, b) t= 40 sec, c) t=70 s, d) t= 100 sec, e) t=130 sec, f) t= 160 sec, g) t=190 sec, h) t= 220 sec, i) t= 250 sec, j) t= 280 sec, k) t=310 sec, l) t= 340 sec

Figure 8.3 shows the evaluation of erosion lines depending on time in one image. Besides, how the average erosion depth changes with time was given in Figure 8.4.

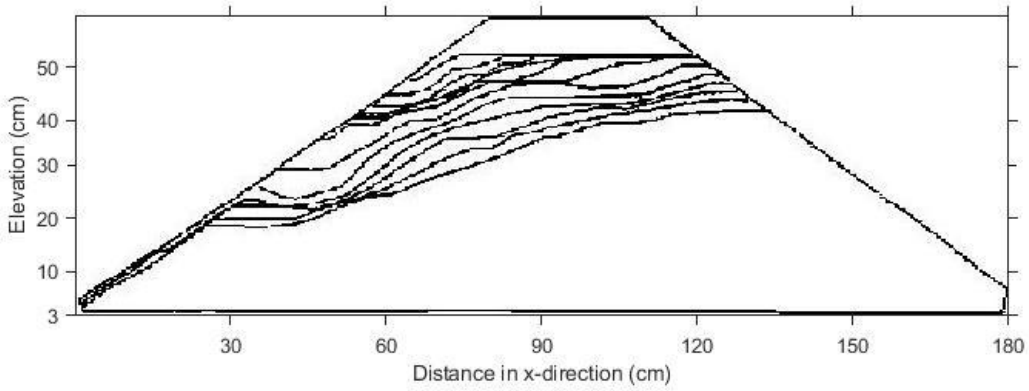

Figure 8.3. Bottom Erosion lines for every 30 seconds (starting from t=10 sec)

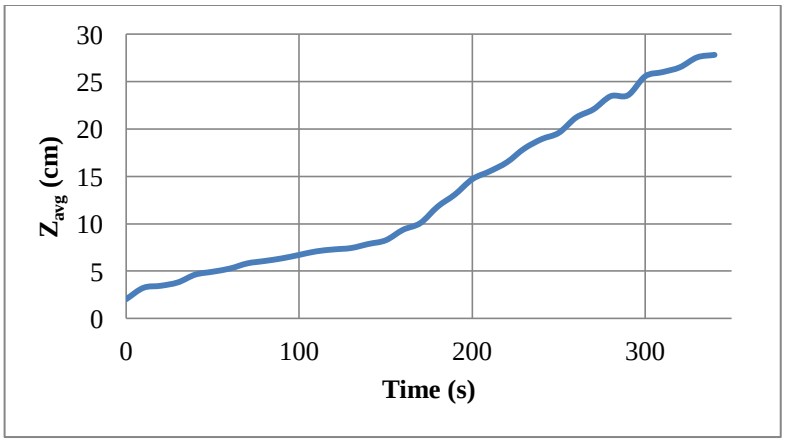

Figure 8.4. Average depth of erosion with time

It was observed that the average breach depth due to piping developed relatively slowly in the first half of the experiment period, while it developed twice as fast in the second half.

The surface where erosion occurs was painted with green color on Matlab environment by using “drawpolygon” command in order to display the eroded area for the side view to be used in image processing (Figure 8.5). Matlab code written using

the function obtained from Matlab Color Thresholder – HSV was used to solve the problem. The eroded and painted side areas were obtained by adjusting the HSV color space. H, S, and V values were adjusted to detect colors other than green. The tonal values of the colors are set as the threshold range [0.091, 0.538] for channel 1, [0.586, 1] for channel 2, and [0.742, 1] for channel 3. For the initial condition, the eroded side area of the breach at $t = 0$ is known as 72 cm². The eroded side area of the breach with green color was determined by image thresholding technique and by converting it binary image then taking its negative, the eroded area set to black color. For the moment t= 0, after the number of black pixels was found to be 2509 with the code, it was accepted that 2509 pixels were equal to 72 cm², and in the pictures belonging to other times, the breach was processed in black with the image thresholding method and the pixel numbers were taken into account, this first limit in cm² rated by value. The eroded side area values were found to correspond with the area values calculated with the Gauss area calculation method by assigning coordinates with the GetData Graph Digitizer program. A comparison of the results is presented in Figure 8.6.

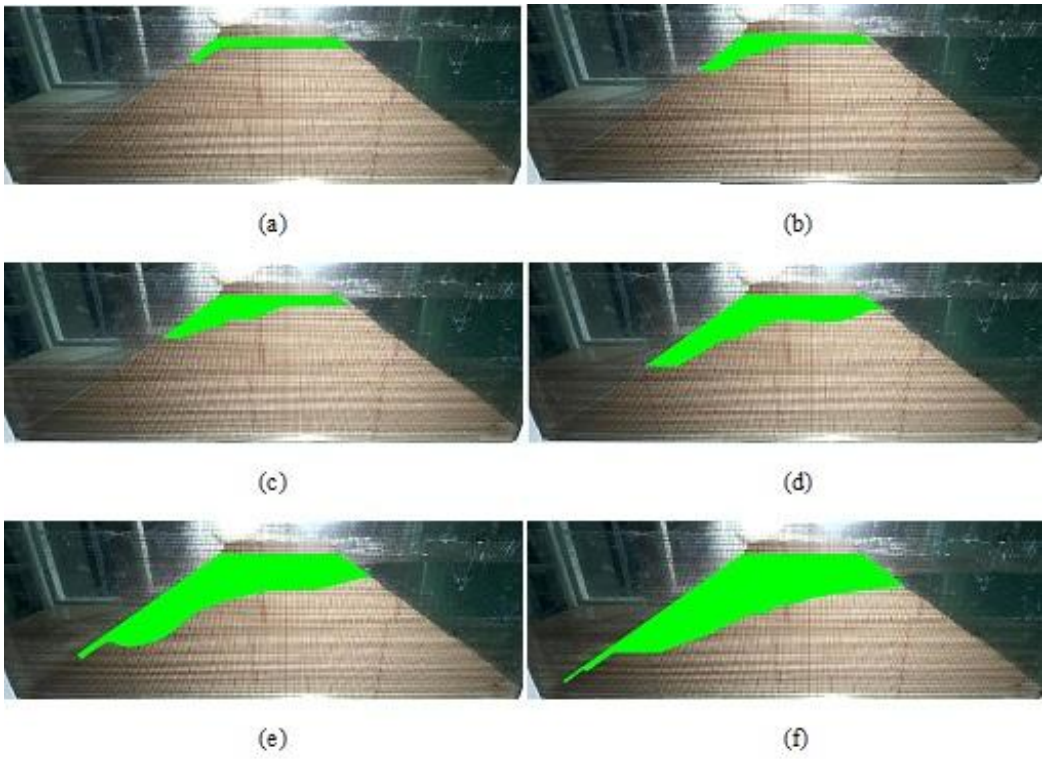

Figure 8.5. The evaluation of eroded side area at different time instants a) t=10 sec, b) t=70 s, c) t=130 sec, d) t=190 sec, e) t= 250 sec, f) t=310 sec

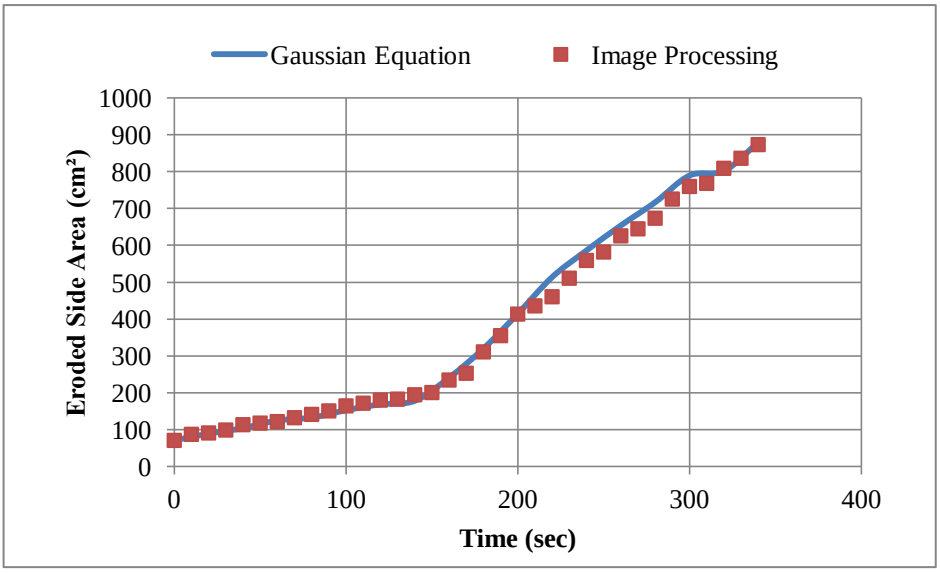

Figure 8.6. Comparison of Gaussian Equation and Image Processing

8.1.1. Comparison of the Experimental Results with the Empirical Equations Given by Sharif et al. (2015)

Sharif et al. (2015) investigated the changes of erosion during the piping event in a model set using the image processing technique in their study. For different λ and so that t_f values they conducted their experiments where λ cited as normalized dry density which is equal to $\Upsilon_{dry}/\Upsilon_{dry_{max}}$ where Υ_{dry} is the dry unit weight of the mixture and $\Upsilon_{dry_{max}}$ is the maximum dry unit weight. Besides, t_f is run time indicating the time when the water level changes as maximum 10%. In the experiments carried out by the researchers, an initial hole to initiate the piping was created at the bottom of the dam body. While Sharif et al. (2015) conducted the standard proctor test, in this study in order to increase the probability of the piping occurrence and decrease the applied energy, the standard proctor test (ASTM-698) was conducted by reducing the applied energy by 50% (13 blows instead of 25) and so obtained the relationship between the maximum dry density and optimum water content was determined as max dry density Υ'_{drymax}= 1.794 g/cm^3 and w_{opt} = 12.5 %. While calculating λ value, the optimum water content corresponding to max dry density obtained from the proctor test with 13 blows is different than the optimum water content corresponding to max dry density obtained from the proctor test with 25 blows. In order to take water content into consideration,

instead of taking the maximum dry density from the proctor test with 25 blows, the dry density corresponding to optimum water content according to the proctor test with 13 blows was taken from the curve of the proctor test with 25 blows (Figure 8.7)

$$\lambda = \frac{\Upsilon_{dry}}{\Upsilon_{dry_{opt}}} = \frac{1.794}{1.831} = 0.98 \qquad (8.1)$$

where $\Upsilon_{dry_{opt}}$ is the dry density taken from the curve of the proctor test with 25 blows corresponding to 12.5% optimum water content coming from the curve of the proctor test with 13 blows.

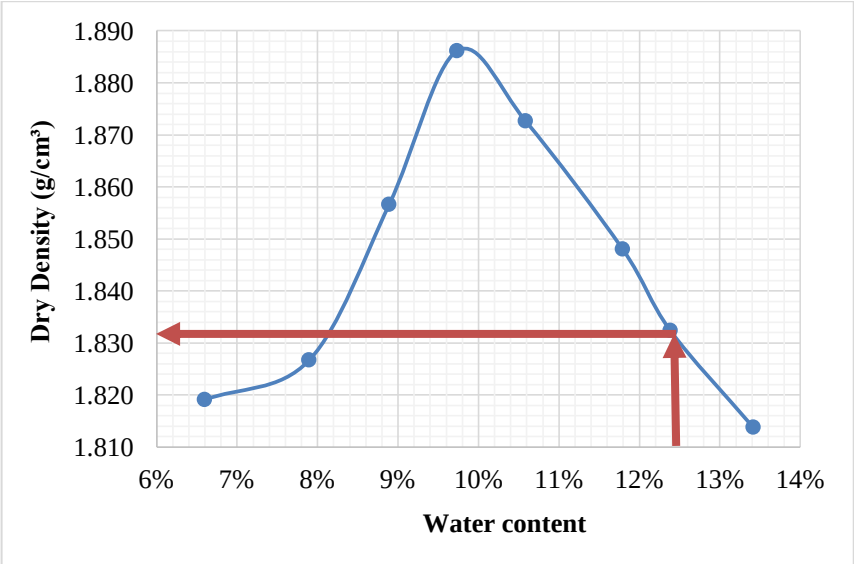

Figure 8.7. Obtaining the dry density corresponding to the optimum water content of 13-blow proctor test curve from the 25-blow standard proctor test curve

Within the scope of the first scenario, a hole with a diameter of 2 cm was created in the upper layer and at the glass side of the dam body. The ratio of the mean depth of erosion to the mean base width of the breaches was found as 1.4 ± 0.1 at different time instants for the first scenario.

Sharif et al. (2015) investigated the area of vertical erosion during the piping event in a model set using the image processing technique in their study. They used the best-fit curve technique and the areas of vertical erosion are obtained as an exponential function expressed as:

$$A_s = A_{in} + 7.59 \times 10^{-3} A_L \lambda^{-3.49} e^{2.39\left(t/t_f\right)} \tag{8.2}$$

where A_s = the area of vertical erosion recorded from the side camera, A_{in} = initial side area calculated approximately as $d_{in} \times L$, in which L is the length of the embankment at the bed level, taken to equal to 0.55 m in their study; and A_L = area of the longitudinal-section of the embankment up to the water surface elevation. The A_s/A_L values obtained by the equation are compared with the experimental findings of this study; the results are represented in Figure 8.8.

The change in the eroded volume of the piping zone with time was estimated from the recorded images. Information from images was taken by upstream, downstream, and right-side camera records. Since the eroded side areas and average widths are known, the area of side erosion is multiplied by the average width of erosion to calculate the approximate volume values which is a similar approach to Sharif et al. (2015)' second approach for volume calculation.

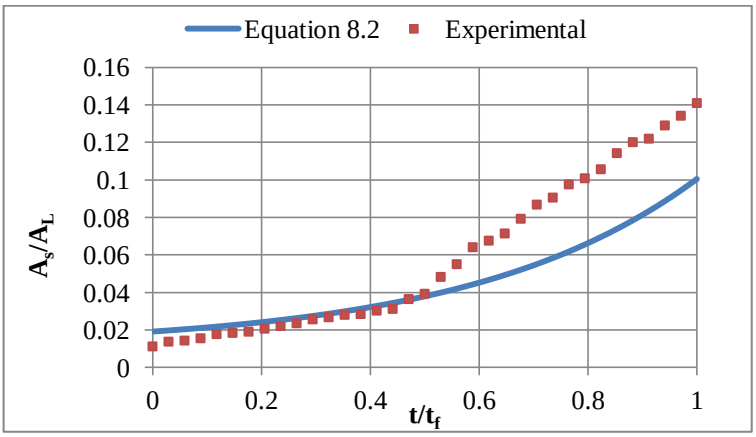

Figure 8.8. Comparison of experimental results with the investigated the area of vertical erosion equation of Sharif et al. (2015)

Sharif et al. (2015) investigated the change in the eroded volume of the piping zone with time during the piping event in a model set using the image processing technique in their study. They used the best-fit curve technique according to the second approach and the eroded volumes are obtained as an exponential function expressed as:

$$V_2 = V_{in} + 0.249 \times 10^{-3} V_e \lambda^{-4.85} e^{3.19\left(t/t_f\right)} \quad (8.3)$$

where V_2 = volume calculated by the second approach, V_{in} = initial volume of the piping zone, and V_e = volume of the embankment up to the water surface elevation. The V_2/V_e obtained by equation is compared with the experimental findings of this study; the results are represented in Figure 8.9. Both for the volume and the area equations, the experiments in this study were investigated only for the maximum 10% water change, the run time t_f was taken as 340 s.

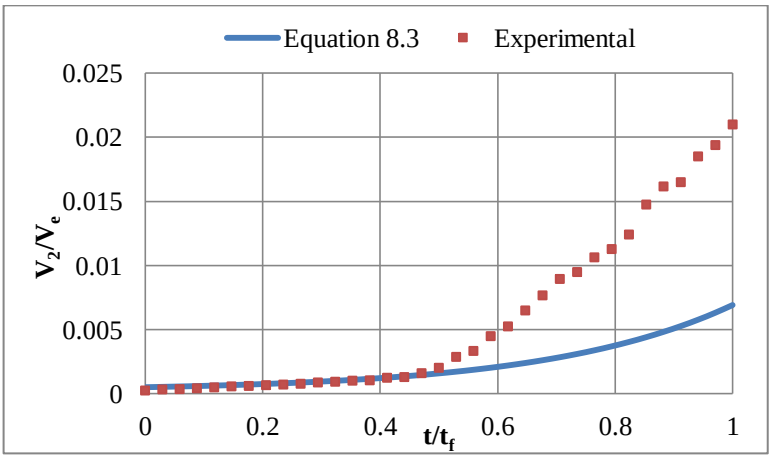

Figure 8.9. Comparison of experimental results with the investigated the eroded volume equation of Sharif et al. (2015)

When experimental findings were compared with the numerical results of the equations presented by Sharif et al. (2015), it was determined that while very consistent results were obtained in the first half of the experiment period, the non-dimensional area and non-dimensional volume values observed in the experiments in the second half

were on average 46% and 183% larger, respectively, than those obtained from the presented empirical equations. This difference is thought to be due to the weak layers being in different positions. In the case of the upper weak layer in question in this study, the breach developed much faster in the second part of the experiment.

8.2. Application of the Image Processing Technique for the Third Scenario

The image processing technique was used to monitor the erosion process in the earthfill dam from the downstream side and upstream side, respectively, also for the third scenario. Digital images obtained from the video camera during the experiment were stored as 24-bit color images with a resolution of 1366 × 768 pixels. These images have been cropped and made to size to be programmed to facilitate image processing. The most important problem encountered in image processing studies is image brightness. To solve this problem, first of all, the surface where the breach will occur was painted with green spray paint in order to increase the visible spectral index of the images to be used in image processing. On the other hand, Matlab code written using the function obtained from Matlab Color Thresholder – HSV was used to solve the problem. The breach areas were obtained by adjusting the HSV color space. In this study, H, S, and V values were adjusted to detect colors other than green, that is, the breach. The tonal values of the colors are set as the threshold range [0.196,1] for channel 1, [0.09.1] for channel 2, and [0.333,1] for channel 3. After the color determination, a median filter was applied to correct the rough parts of the dam surface that would be detected as black color shown in Figure 8.10. For the initial condition, the area of the breach at $t = 0$ is known. Since the diameter of the breach is 2 cm, the area is equal to 3.14 cm². The area of the breach was determined by image thresholding technique and set to black color. For the moment t= 0, after the number of black pixels was found to be 37 with the code, it was accepted that 37 pixels were equal to 3.14 cm², and in the pictures belonging to other times, the breach was processed in black with the image thresholding method and the pixel numbers were taken into account, this first limit in cm² rated by value.

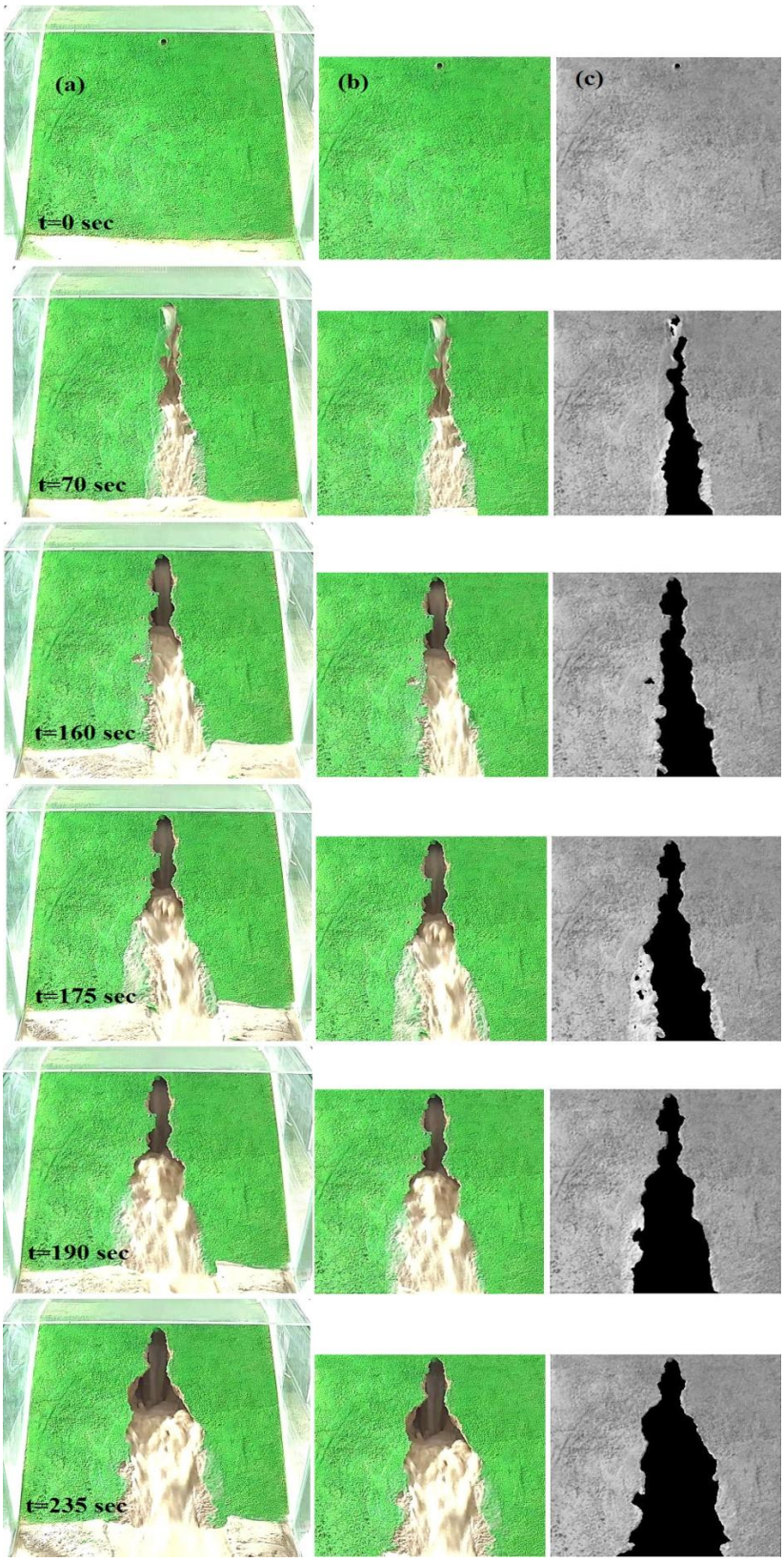

Figure 8.10. Time dependent image processing using Matlab Color Thresholder for downstream – HSV. a) Original picture from experiments. b) Cropped Image c) After Color Thresholding

The image processing technique was also used to monitor the erosion process in the earthfill dam from the upstream side. The same procedure has been applied, however, this time the tonal values of the colors are set as the threshold range [0.196, 1] for channel 1, [0.25, 1] for channel 2, and [0.333, 1] for channel 3; then for the moment t= 0, after the number of black pixels was found to be 88 with the code, it was accepted that 88 pixels were equal to 3.14 cm². Image processing study for upstream is given in Figure 8.11.

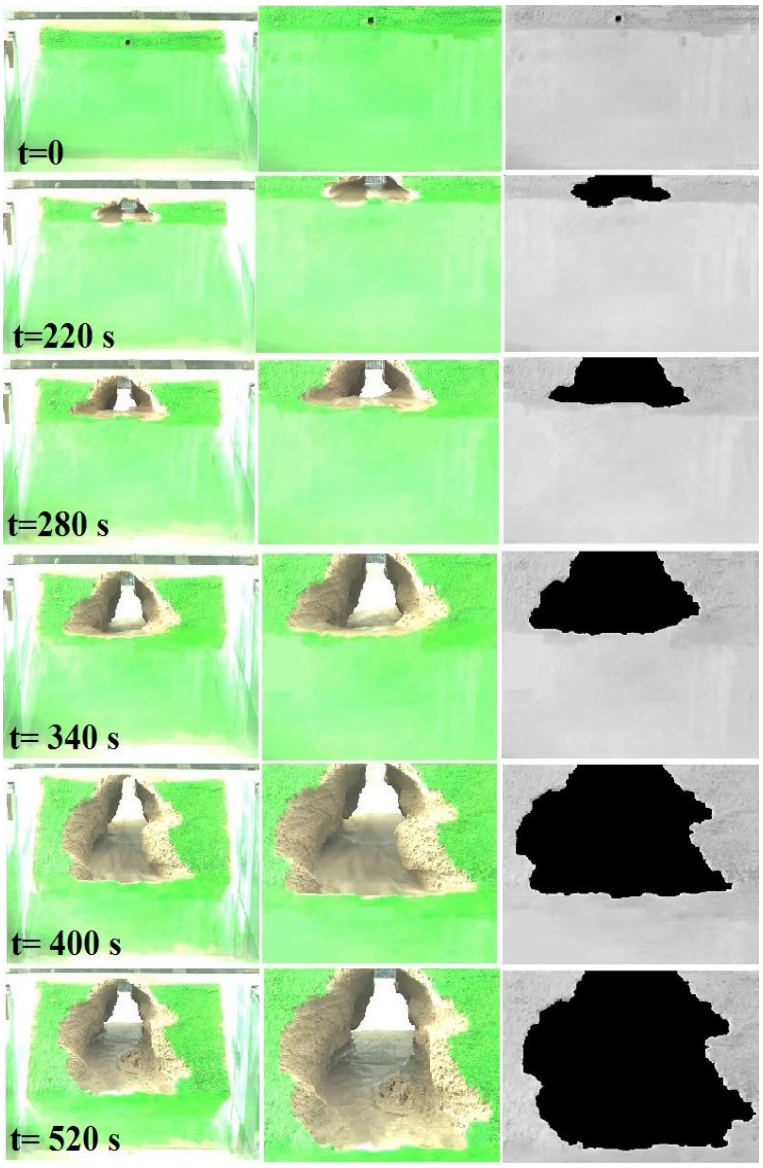

Figure 8.11. Time dependent image processing using Matlab Color Thresholder for upstream – HSV. a) Original picture from experiments. b) Cropped Image c) After Color Thresholding

For the third scenario, the breach area values for downstream and upstream were found to correspond with the area values calculated with the Gauss area calculation method by assigning coordinates with the GetData Graph Digitizer program. A comparison of the results is presented in Figure 8.12 and Figure 8.13 respectively.

The ratio of the mean depth of erosion to the mean base width of the pipes was found as 1.02 ± 0.1 at different time instants for the third scenario.

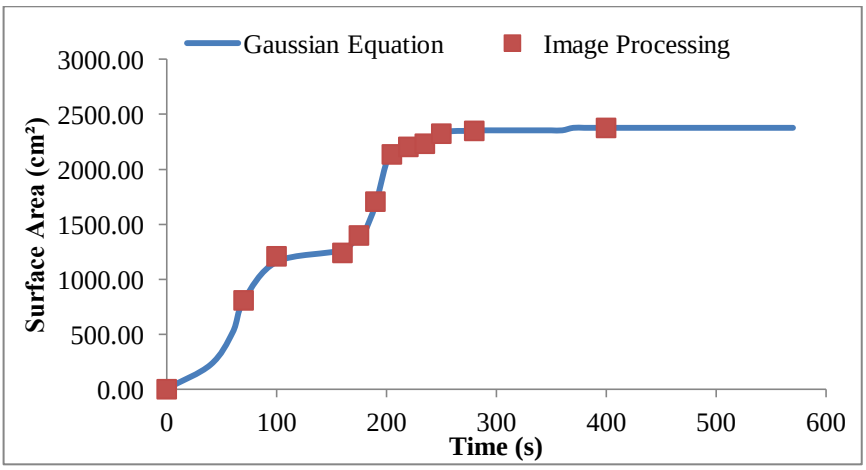

Figure 8.12. Comparison of Gaussian equation and image processing for the calculation of surface areas for downstream

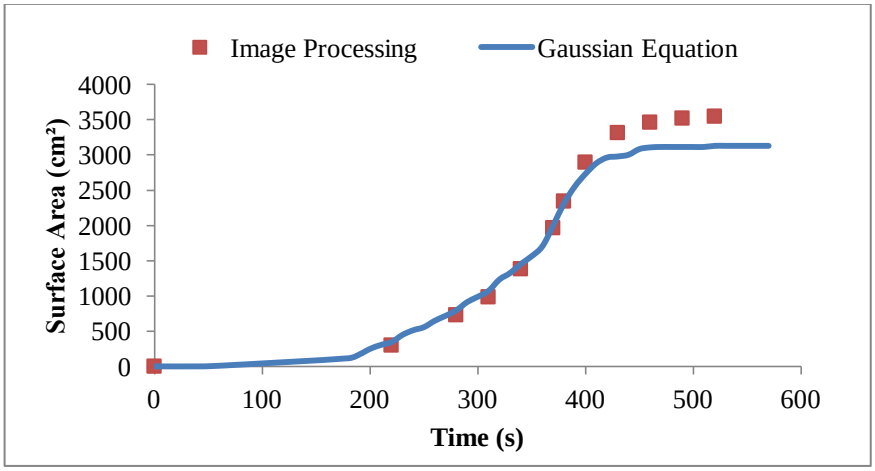

Figure 8.13. Comparison of Gaussian equation and image processing for the calculation of surface areas for upstream

CHAPTER 9

NONLINEAR REGRESSION ANALYSIS

In numerical solution analyzes in which the dam failure is modelled, the breach discharge is determined by using Equation 9.1 given for the weirs;

$$Q = CLH^{3/2} \tag{9.1}$$

where Q is the discharge, L is the weir crest width and H is the water load on the weir. The C coefficient takes values ranging from 1.5 to 2.2. Since the breach formed due to piping does not have certain geometry, this approach is not realistic and a coefficient that varies according to the shape of the breach should be investigated. In this study, average L and H values are obtained by determined wetted areas of upstream for each scenario, and then C coefficient was investigated for Equation 9.1 by using nonlinear regression analysis. C coefficient was found as 0.554 and discharge values were estimated with a determination coefficient (R^2) of 0.56 for the first scenario, 0.798 with R^2 of 0.79 for the second scenario, and 1.025 with R^2 of 0.81 for the third scenario. Scatter plots are represented in the following (Figure 9.1, Figure 9.2, and Figure 9.3).

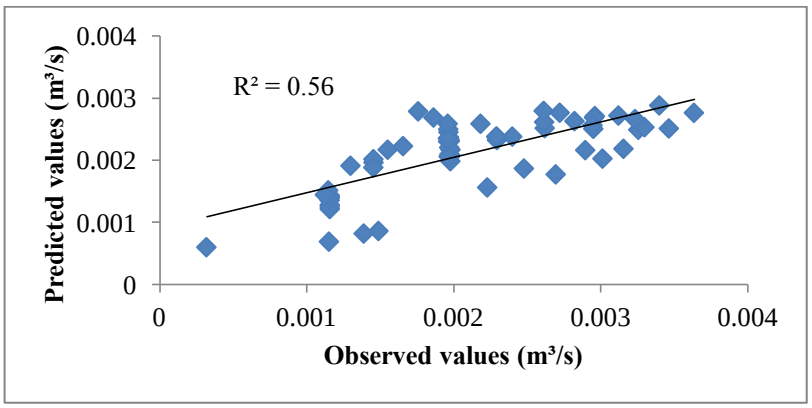

Figure 9.1. Scatter plot of observed and predicted breach discharge values by Equation 9.1 for the first scenario

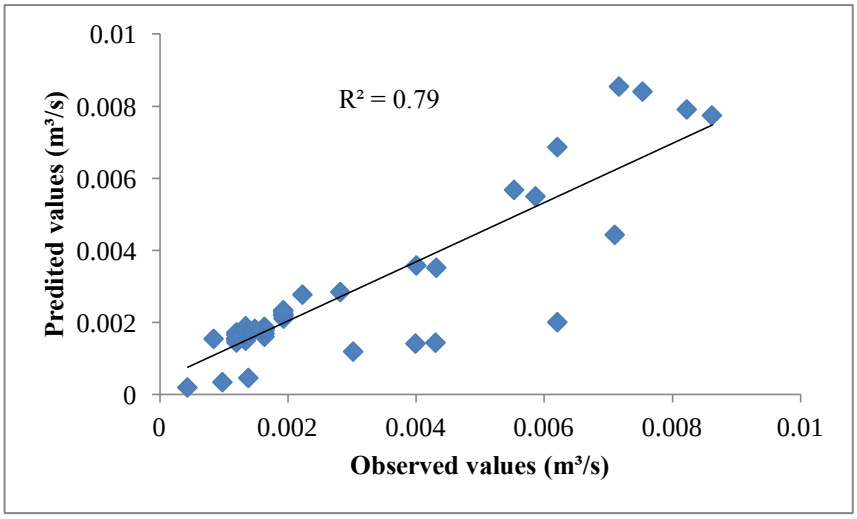

Figure 9.2. Scatter plot of observed and predicted breach discharge values by Equation 9.1 for the second scenario

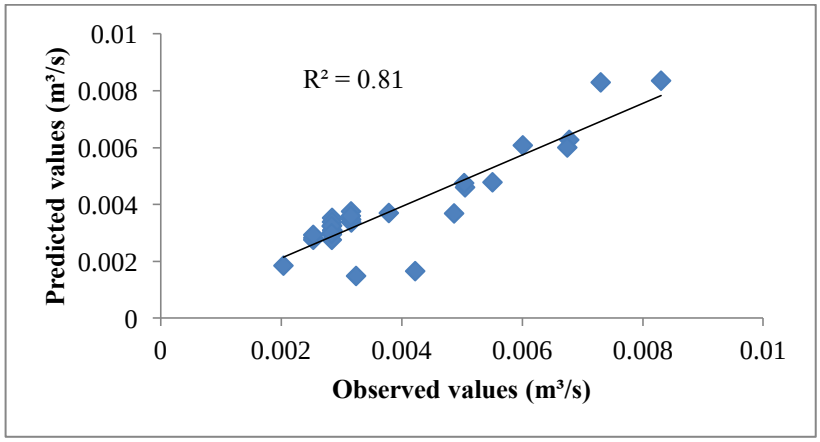

Figure 9.3. Scatter plot of observed and predicted breach discharge values by Equation 9.1 for the third scenario

Since the scenarios were fulfilled with the same soil composition and compaction, the average of the C coefficients is calculated as 0.792 and Equation 9.2 gives the breach discharge equation given for the weirs as follows:

$$Q = (0.792)LH^{3/2} \tag{9.2}$$

By using Equation 9.2, breach discharge values were calculated again for all the scenarios, and R^2 values were obtained the same for all the scenarios and their scatter plots are given in the following (Figure 9.4, Figure 9.5, and Figure 9.6).

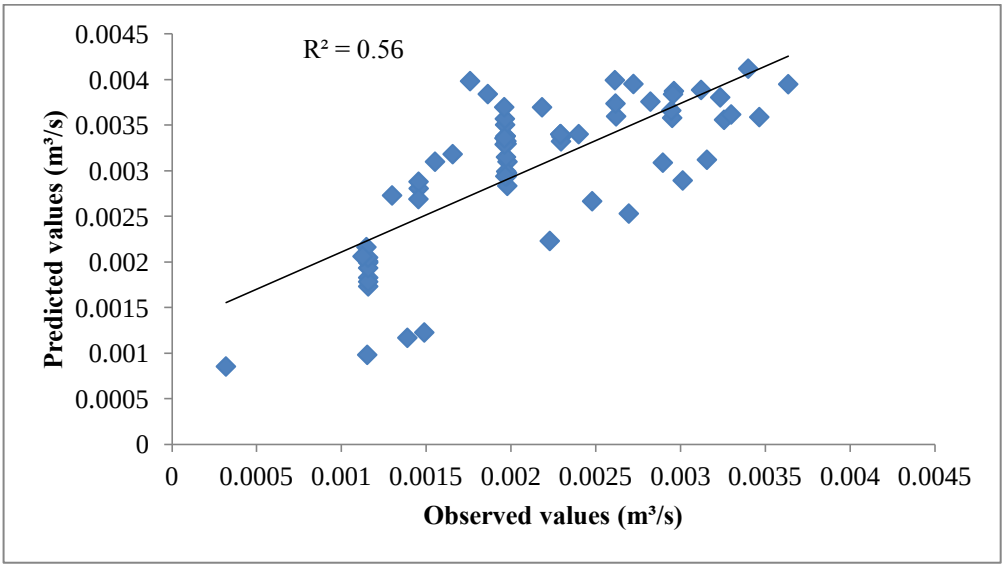

Figure 9.4. Scatter plot of observed and predicted breach discharge values for the first scenario with breach discharge equation obtained by average C coefficient (by Equation 9.2)

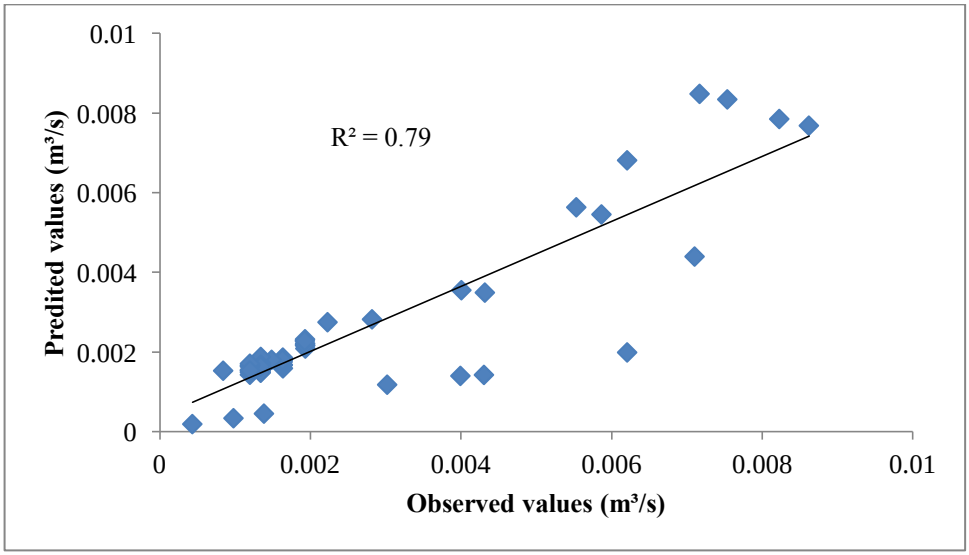

Figure 9.5. Scatter plot of observed and predicted breach discharge values for the second scenario with breach discharge equation obtained by average C coefficient (by Equation 9.2)

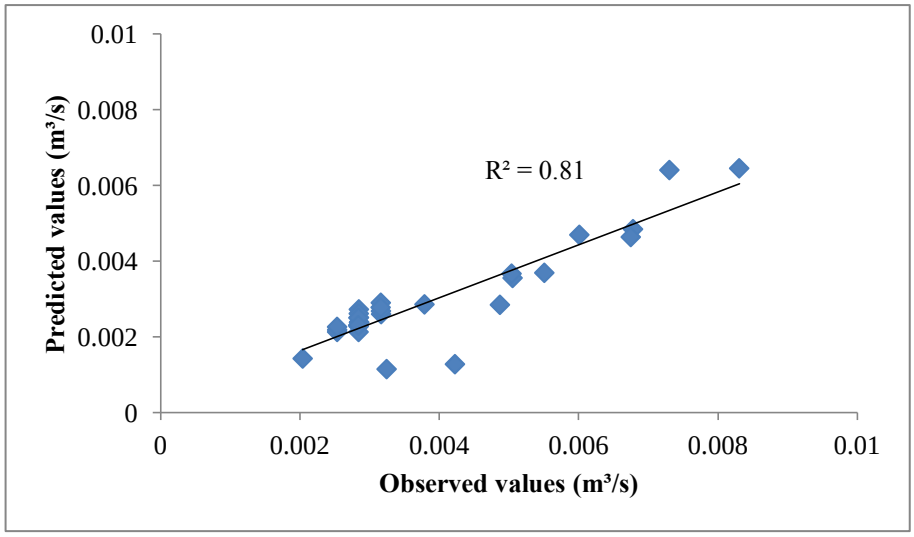

Figure 9.6. Scatter plot of observed and predicted breach discharge values for the third scenario with breach discharge equation obtained by average C coefficient (by Equation 9.2)

Besides, a nonlinear regression analysis was conducted for the power of the breach discharge equation given for the weirs, so the equation becomes as follows:

$$Q = CLH^{x} \tag{9.3}$$

C and x coefficients were investigated for Equation 9.3 by using nonlinear regression analysis. C coefficient was found as 9.813, x coefficient was found as 2.542 and discharge values were estimated with a determination coefficient (R^2) of 0.85 for the first scenario, C coefficient as 0.780, and x coefficient as 1.491 with R^2 of 0.79 for the second scenario, and C coefficient as 1.107 and x coefficient as 1.528 with R^2 of 0.82. Scatter plots are represented in the following (Figure 9.7, Figure 9.8, and Figure 9.9). When the coefficients are compared with each other, it can be said that the x coefficients obtained by the second and third scenarios which were conducted by creating the initial hole at the middle were too close to each other and close to the power of Equation 9.1 which is 1.5. However, both the C and x coefficients of the first scenario whose initial hole exists at the glass side were much far away from the coefficients obtained by other scenarios. Besides, the C coefficients of the second and

third scenarios obtained for Equation 9.3 were too close to the coefficients obtained for Equation 9.1, respectively for each scenario.

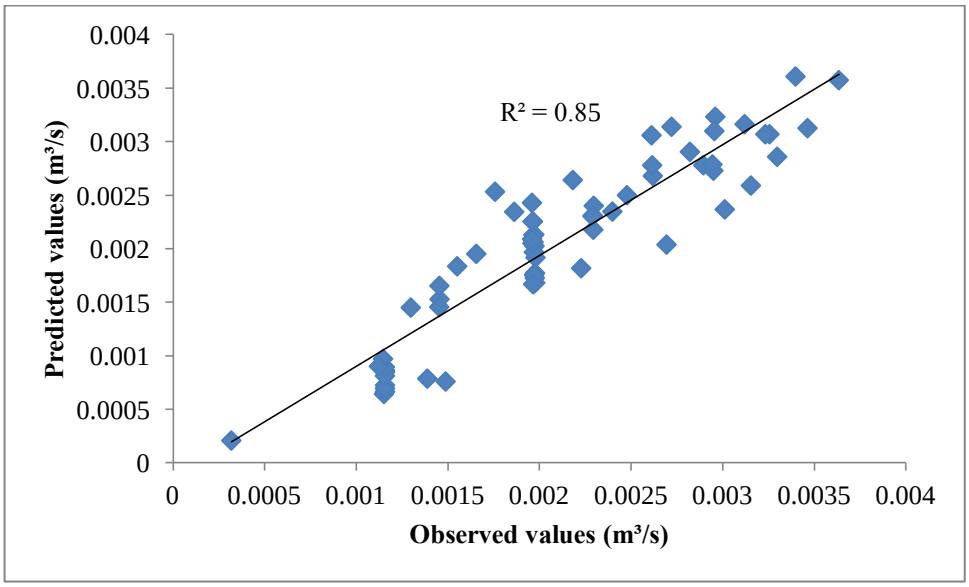

Figure 9.7. Scatter plot of observed and predicted breach discharge values by Equation 9.3 for the first scenario

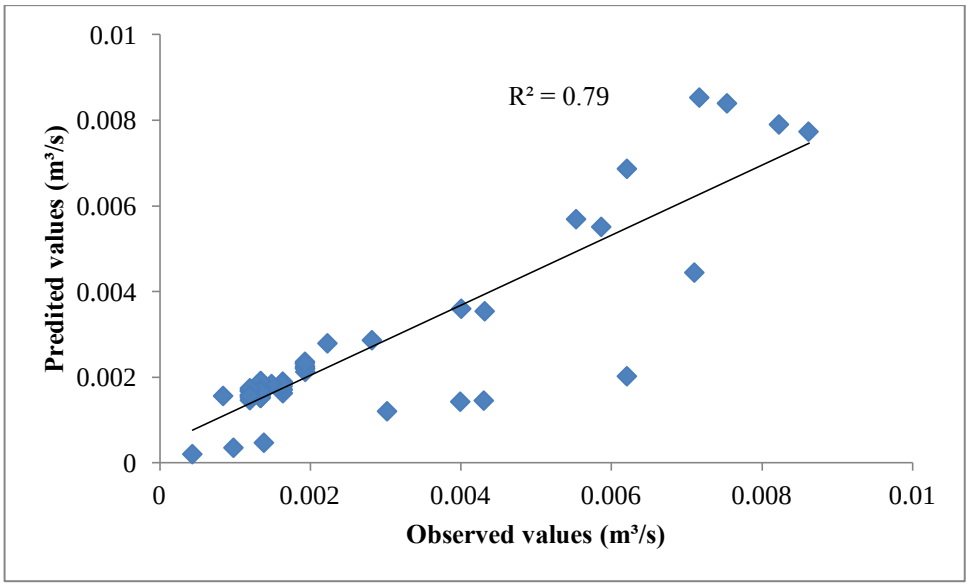

Figure 9.8. Scatter plot of observed and predicted breach discharge values by Equation 9.3 for the second scenario

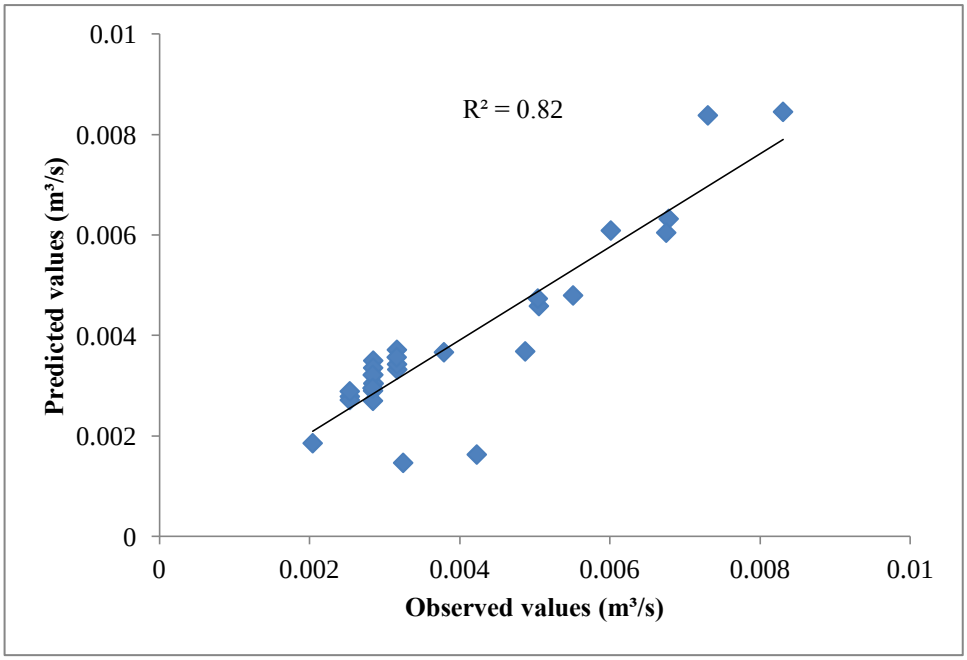

Figure 9.9. Scatter plot of observed and predicted breach discharge values by Equation 9.3 for the third scenario

Since the coefficients obtained by the first scenario were so different than other scenarios, only the average is taken for the coefficients of the second and third scenarios. The average of the C coefficients is calculated as 0.9435 and the average of the x coefficients is calculated as 1.5095. Equation 9.4 gives the breach discharge equation given for the weirs as follows:

$$Q = (0.9435)LH^{1.5095} \tag{9.4}$$

By using Equation 9.4, breach discharge values were calculated again for the second and third scenarios, and R^2 values were obtained the same for the scenarios, and their scatter plots are given in the following (Figure 9.10 and Figure 9.11).

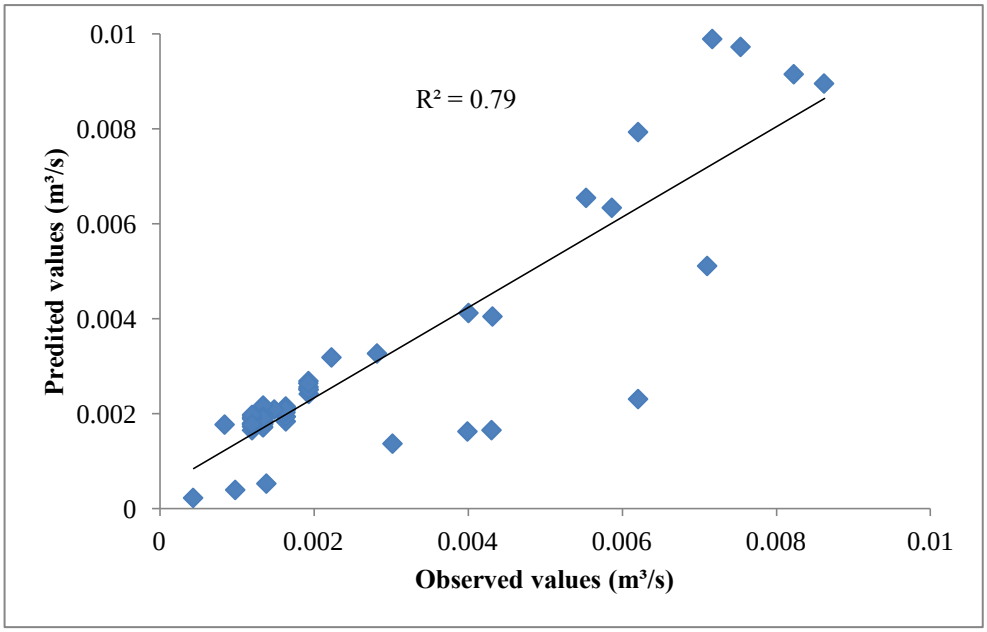

Figure 9.10. Scatter plot of observed and predicted breach discharge values by Equation 9.4 for the second scenario

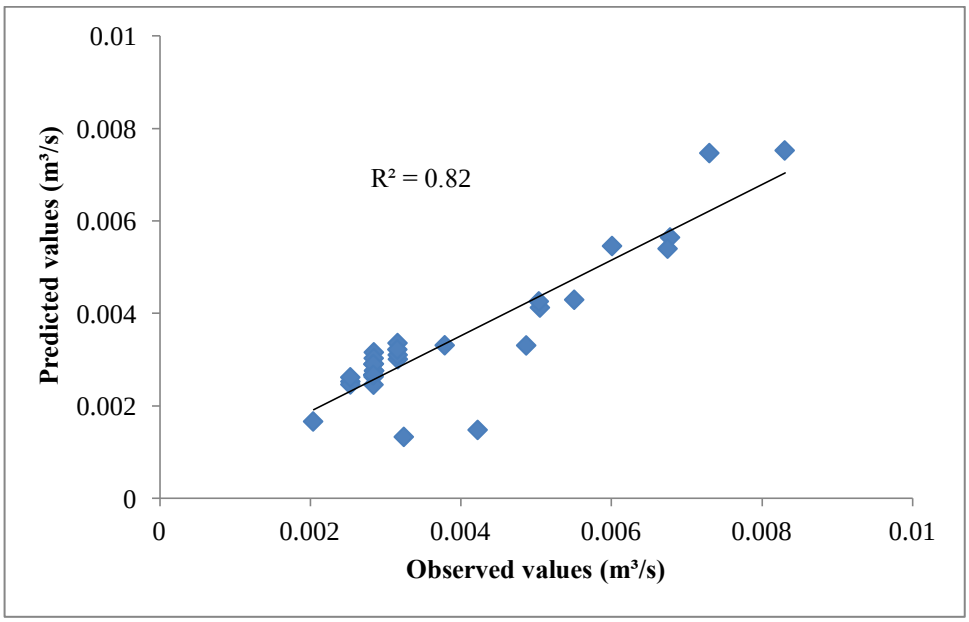

Figure 9.11. Scatter plot of observed and predicted breach discharge values by Equation 9.4 for the third scenario

CHAPTER 10

CONCLUSION AND RECOMMENDATIONS

- The place of the initial hole affects the discharge of water through the breach, surface breach areas, wetted areas, and accordingly velocities for upstream and downstream.
- The discharge of water through the breach at the dam including the initial hole at the middle was approximately twice of the dam including the initial hole at the glass side.
- The maximum breach surface area at upstream is greater than at downstream.
- While the ratio of the mean depth of erosion to the mean base width of the breaches was found as 1.4 ± 0.1 at different time instants for the first scenario whose initial hole exists at the glass side, for the third scenario whose initial hole exists at the middle of the dam, the ratio was found as 1.02 ± 0.1 at different time instants.
- Painting the surface of the dam with green color makes the image processing easier.
- The comparison of the areas obtained by Gauss area calculation and image processing shows that image processing is a good alternative method to calculate the area.
- In order to be aware of the exact soil properties and obtain exact experimental findings, the dam should be constructed from the beginning rather than repairing the failed part, because it has been seen that, there were some differences between the experimental findings, especially at the time parameter when the second and third scenarios were compared.
- To test repeatability and symmetry, the repetition should be conducted for each scenario.
- In this study, only by using one soil composition and one compaction rate, the scenarios were carried out. However, scenarios can be handled again by using different soil compositions and compaction rates.

- By changing the level of the initial hole, the experiments should be repeated and experimental findings should be compared.
- Rather than creating the weak region with an initial hole, the weak region can be maintained by changing the soil compaction rate of the weak part or by using a different material which can increase the probability of seepage, and the experiment can be repeated.
- The nonlinear regression analysis should be tried again for a scenario conducted for the dam whose initial hole exists at the glass side to check obtained C and x coefficients for Equation 9.3.
- The nonlinear regression analysis for Equation 9.3 showed that x coefficients were acquired too close to 1.5 for the scenarios conducted where the initial hole was created at the middle, which has a good agreement with the breach discharge equation given for the weirs in numerical solution analyses in which the dam failure is modelled (Equation 9.1).

REFERENCES

Alamdari, N Zaki, M Banihashemi, and A Mirghasemi. 2012. "A Numerical Modeling of Piping Phenomenon in Earth Dams." *Engineering and Technology International Journal of Civil and Environmental Engineering* 6 (10): 772–74.

Andreini, Marco, Paolo Gardoni, Stefano Pagliara, and Mauro Sassu. 2019. "Probabilistic Models for the Erosion Rate in Embankments and Reliability Analysis of Earth Dams." *Reliability Engineering and System Safety* 181 (September 2017): 142–55. https://doi.org/10.1016/j.ress.2018.09.023.

Ashraf, Muhammad, Ahmed Hussein Soliman, Entesar El-Ghorab, and Alaa El Zawahry. 2018. "Assessment of Embankment Dams Breaching Using Large Scale Physical Modeling and Statistical Methods." *Water Science* 32 (2): 362–79. https://doi.org/10.1016/j.wsj.2018.05.002.

Bonelli, S. 2013. *Erosion in Geomechanics Applied to Dams and Levees*. John Wiley & Sons.

Bonelli, Stéphane, and N. Benahmed. 2010. "Piping Flow Erosion in Water Retaining Structures: Inferring Erosion Rates from Hole Erosion Tests and Quantifying the Failure Time." In *IECS 2010, 8th ICOLD European Club Symposium Dam Safety-Sustainability in a Changing Environment*. Innsbruck, Austria. https://hal.archives-ouvertes.fr/hal-00555648.

Brunner, Gary. 2014. "Using HEC-RAS for Dam Break Studies." *U.S. Army Corps of Engineers Institute for Water Resources Hydrologic Engineering Center*. https://www.scopus.com/inward/record.uri?eid=2-s2.0-84876361807&partnerID=40&md5=dfcbf4adad65f78943b9945d7689f84d.

Chen, Sheng shui, Qi ming Zhong, and Guang ze Shen. 2019. "Numerical Modeling of Earthen Dam Breach Due to Piping Failure." *Water Science and Engineering* 12 (3): 169–78. https://doi.org/10.1016/j.wse.2019.08.001.

Costa, J. E. 1985. "Floods from Dam Failures Open-File Report 85-560." Denver.

Dahlke, Karl. 2017. "Shoelace Formula." 2017. http://book.mathreference.com/struct#shoe.

Dai, F C, C F Lee, J H Deng, and L G Tham. 2005. "The 1786 Earthquake-Triggered Landslide Dam and Subsequent Dam-Break Flood on the Dadu River , Southwestern China." *Geomorphology* 65: 205–21.

https://doi.org/10.1016/j.geomorph.2004.08.011.

"Dam Safety Management Center of the Ministry of Water Resources, P. R. China." 2019. In *Dam Breach Register Book of the National Reservoirs*.

Elkholy, Mohamed, Yusuf A. Sharif, M. Hanif Chaudhry, and Jasim Imran. 2015. "Effect of Soil Composition on Piping Erosion of Earthen Levees." *Journal of Hydraulic Research* 53 (4): 478–87. https://doi.org/10.1080/00221686.2015.1026951.

Fell, Robin, Chi Fai Wan, John Cyganiewicz, and Mark Foster. 2003. "Time for Development of Internal Erosion and Piping in Embankment Dams." *Journal of Geotechnical and Geoenvironmental Engineering* 129 (4): 307–14. https://doi.org/10.1061/(asce)1090-0241(2003)129:4(307).

Fleshman, Mandie S., and John D. Rice. 2014. "Laboratory Modeling of the Mechanisms of Piping Erosion Initiation." *Journal of Geotechnical and Geoenvironmental Engineering* 140 (6): 04014017-1–12. https://doi.org/10.1061/(asce)gt.1943-5606.0001106.

Froehlich, David C. 2016. "Predicting Peak Discharge from Gradually Breached Embankment Dam." *Journal of Hydrologic Engineering* 21 (11): 04016041. https://doi.org/10.1061/(asce)he.1943-5584.0001424.

Greco, M., M. Pontillo, M. Iervolino, and A. Leopardi. 2008. "2DH Numerical Simulation of Breach Evolution in an Earth Dam." In *River-Flow2008*, edited by M. S. Altinakar, M. A. Kökpınar, I. Aydın, S. Çokgör, and S. Kırkgöz, 1:661–67. Kubaba, Ankara,TURKEY.

Hanson, Gregory, Ronald - Ron Tejral, Sherry Hunt, and Darrel Temple. 2010. "Internal Erosion and Impact of Erosion Resistance." In *Proceedings of the 30th U.S. Society on Dams Annual Meeting and Conference April 12-16, 2010*, 773–84. Sacramento, California.

ICOLD. 2017. "INTERNAL EROSION OF EXISTING DAMS , Levees and Dikes , and Their Foundations L ' ÉROSION INTERNE DANS LES DIGUES , Barrages Existants et Leurs Fondations."

Kulkarni, Nilima. 2012. "Color Thresholding Method for Image Segmentation of Natural Images." *International Journal of Image, Graphics and Signal Processing* 4 (1): 28–34. https://doi.org/10.5815/ijigsp.2012.01.04.

Lachouette, Damien, Frédéric Golay, and Stéphane Bonelli. 2008. "One-Dimensional Modeling of Piping Flow Erosion." *Comptes Rendus - Mecanique* 336 (9): 731–36.

https://doi.org/10.1016/j.crme.2008.06.007.

Madani, Mehdi, Mahdi Bagheri, Ramin Sahba, and Amin Sahba. 2011. "Real Time Object Detection Using a Novel Adaptive Color Thresholding Method." In *Proceedings of the 2011 International ACM Workshop on Ubiquitous Meta User Interfaces*, 13–16.

Morris, M, M Hassan, A Kortenhaus, P Geisenhainer, P Visser, and Y Zhu. 2008. "Modelling Breach Initiation and Growth." *Flood Risk Management: Research and Practice*, 581–91. https://doi.org/10.1201/9780203883020.ch67.

Morris, Mark William. 2013. "Breaching of Earth Embankments and Dams." The Open University. https://doi.org/10.21954/ou.ro.0000d502.

Mustikasari, Metty, and Sarifuddin Madenda. 2014. "Performance Analysis of Color Based Image Retrieval." *International Journal of Computers & Technology* 12 (4): 3373–81. https://doi.org/10.24297/ijct.v12i4.7058.

MWR. 2015. *Dam Breach Register Book of the National Reservoirs*. Nanjing, China: Dam Safety Management Center of the Ministry of Water Resources.

Saliba, Fadi, Ronald Bou Nassar, Naji Khoury, and Yara Maalouf. 2019. "Internal Erosion and Piping Evolution in Earth Dams Using an Iterative Approach." In *Geo-Congress 2019: Soil Erosion, Underground Engineering, and Risk Assessment*, edited by Christopher L. Meehan, Sanjeev Kumar, Miguel A. Pando, and Joseph T. Coe, 67–75. https://doi.org/10.1061/9780784482155.007.

Sellmeijer, J. B. 1988. "On the Mechanism of Piping under Impervious Structures." Bibliotheek Technische Universiteit. http://repository.tudelft.nl/assets/uuid:7f3c5919-1b37-4de9-a552-1f6e900eeaad/TR diss 1670(1).pdf.

Shapiro, Linda G., and George C. Stockman. 2002. "Computer Vision." In . Vol. 9. Prentice Hall.

Sharif, Yusuf A., Mohamed Elkholy, M. Hanif Chaudhry, and Jasim Imran. 2015. "Experimental Study on the Piping Erosion Process in Earthen Embankments." *Journal of Hydraulic Engineering* 141 (7): 04015012. https://doi.org/10.1061/(asce)hy.1943-7900.0001019.

Temple, D.M., G.J. Hanson, M.L. Neilsen, and K.R Cook. 2005. "Simplified Breach Analysis Model for Homogeneous Embankments: Part I, Background and Model Components." In *Proceedings of the 2005 U.S. Society on Dams Annual Meeting and Conference, Salt Lake City, Utah*, 151–61.

"Understanding Color Spaces and Color Space Conversion." n.d. MathWorks. https://uk.mathworks.com/help/images/understanding-color-spaces-and-color-space-conversion.html.

Wang, Bo, Yunliang Chen, Chao Wu, Yong Peng, Jiajun Song, Wenjun Liu, and Xin Liu. 2018. "Empirical and Semi-Analytical Models for Predicting Peak Outflows Caused by Embankment Dam Failures." *Journal of Hydrology* 562 (May): 692–702. https://doi.org/10.1016/j.jhydrol.2018.05.049.

Yang, Jian, Chengjun Liu, and Lei Zhang. 2010. "Color Space Normalization: Enhancing the Discriminating Power of Color Spaces for Face Recognition." *Pattern Recognition* 43 (4): 1454–66. https://doi.org/10.1016/j.patcog.2009.11.014.

Yang, Kuo Hsin, and Jyun Yen Wang. 2017. "Experiment and Statistical Assessment on Piping Failures in Soils with Different Gradations." *Marine Georesources and Geotechnology* 35 (4): 512–27. https://doi.org/10.1080/1064119X.2016.1213338.

Zhang, Jing, Zhi-xue Guo, Shu-you Cao, and Feng-guang Yang. 2012. "Experimental Study on Scour and Erosion of Blocked Dam" 5 (50979064): 219–29. https://doi.org/10.3882/j.issn.1674-2370.2012.02.010.

Zhenzhen, Liu. 2015. "HYDRO-MECHANICAL ANALYSIS OF BREACH PROCESSES DUE TO LEVEE FAILURE." UNIVERSITÉ D'AIX-MARSEILLE ÉCOLE.

Zhong, Qi-ming, Sheng-shui Chen, and Zhao Deng. 2017. "Numerical Model for Homogeneous Cohesive Dam Breaching Due to Overtopping Failure." *Journal of Mountain Science* 14 (3): 571–80. https://doi.org/10.1007/s11629-016-3907-5.

Zhong, Qiming, Lin Wang, Shengshui Chen, Zuyu Chen, Yibo Shan, Qiang Zhang, Qiang Ren, et al. 2021. "Breaches of Embankment and Landslide Dams - State of the Art Review." *Earth-Science Reviews* 216 (October 2020): 103597. https://doi.org/10.1016/j.earscirev.2021.103597.

Zhu, Yonghui, P. J. Visser, J. K. Vrijling, and GuangQian Wang. 2011. "Experimental Investigation on Breaching of Embankments." *Science China Technological Sciences* 54 (1): 148–55. https://doi.org/10.1007/s11431-010-4208-9.